UNIVERSITÀ
DEGLI STUDI
FIRENZE

DOTTORATO DI RICERCA IN
INTERNATIONAL DOCTORATE IN
ATOMIC AND MOLECULAR PHOTONICS

CICLO XXX

COORDINATORE Prof. Roberto Righini

Multimodal imaging for tissue diagnostics by combined two-photon and Raman microscopy

Settore Scientifico Disciplinare FIS/03

Dottorando
Dott. Baria Enrico

Tutore
Prof. Cicchi Riccardo

Coordinatore
Prof. Righini Roberto

Anni 2014/2017

TABLE OF CONTENTS

Chapter 1: Introduction

Nonlinear optical (NLO) microscopy and Raman spectroscopy had been widely used for non-invasive and label-free imaging and diagnosis of a great variety of cells and biological tissues. In fact, using these optical techniques provides many and important advantages, which can be exploited for surgical, clinical and pathological applications.

Nonlinear excitation provides deep optical sectioning capability in tissues thanks to a great variety of molecules and biological structures useful for imaging large tissue areas in a relatively short amount of time. This approach is particularly suited for studying tissue morphology with high resolution, but without time-consuming and invasive processes that are usually adopted for common histopathological routines.

Raman spectroscopy is based on the inelastic scattering of light, which can be used for investigating the rotational-vibrational spectrum of a molecule. Such spectrum is highly related to molecular structure so that recording the Raman spectrum of biological tissues provides information about their molecular composition in a label-free and non-invasive modality. However, this modality require very long acquisition times.

Therefore, arranging NLO microscopy and Raman spectroscopy in a complementary approach could integrate the speed of the former with the specificity of the latter. Morphological features, highlighted through NLO imaging, can help identify specific regions of interest within the overall sample; then, Raman spectroscopy can be applied for detailed evaluation of their composition without requiring very long acquisitions. This method could provide a powerful tool for biomedical applications, ranging from pathological examination of *ex vivo* biopsies to *in vivo* clinical detection of both tumour and non-tumour diseases.

During my PhD, I designed and developed a custom-made multimodal microscope combining Fluorescence Lifetime Imaging Microscopy (FLIM), Second Harmonic Generation (SHG) microscopy, Two-Photon Excited Fluorescence (TPEF) microscopy and Raman microscopy for studying both thin and thick ("bulk") biological samples. I performed several experimental measurements for characterising spatial and temporal resolution of the microscope, as well as for calibrating its components. Then, I conducted three research studies for demonstrating the capabilities of both NLO and Raman microscopy. Firstly, I

used FLIM, SHG and TPEF microscopy for examining *ex vivo* human carotids affected by atherosclerosis. In this framework, multiphoton imaging allowed identifying specific tissues within the atherosclerotic plaque, whose presence and size are important data for pathological assessment. Secondly, I used Raman spectroscopy for discriminating three *in vitro* melanoma cell lines. The recorded spectra were successfully classified through two robust scoring methods. Finally, I combined TPEF and Raman microscopy for studying two *ex vivo* bulk tissue types: human bladder affected by urothelial carcinoma (UC) and atherosclerotic aorta obtained from an animal model. This complementary approach proved its potential for *in vivo* applications. In fact, TPEF imaging allowed discriminating healthy and diseased tissues based on their morphology, while the recorded Raman spectra reflected their molecular composition.

This thesis is divided in three main parts, as follows:

- a theoretical discussion on the physical principles at the basis of nonlinear microscopy and Raman spectroscopy (chapter 1);
- a description of the materials and methods, including the characterisation of the experimental setups, and the methods used for data analysis (chapter 2);
- the results obtained from the characterisation of human atherosclerotic tissues (chapter 3), from the discrimination of melanoma cell lines (chapter 4), and from the examination of both arterial and urothelial tissues (chapter 5);
- final consideration and conclusions in chapter 6.

1.1 Theory of nonlinear optical (NLO) microscopy

Nonlinear optics describes the behaviour of light in dielectric media wherein the induced electric polarization is nonlinearly dependent on the incident electric field [1]. Observing such phenomenon requires high peak intensity light sources, e.g. an ultrafast-pulsed laser. In fact, at low intensity, the properties of matter are independent from the amplitude of electric fields. In such regime, according to the superposition principle, electromagnetic (EM) waves pass through materials, or are reflected from borders and interfaces, without interacting each other. Instead, pulsed lasers provide sufficiently high peak intensity to change the optical properties of matter: EM waves can now interact, exchanging impulse and energy, therefore the superposition principle is no longer valid. Such interactions may generate electric fields

with different frequencies – e.g. higher harmonic and sum/difference frequencies – with respect to the incident radiation.

NLO microscopy can be divided in two main categories: coherent and incoherent [2]. Incoherent microscopy generates optical signals whose phase is random and whose power is proportional to the concentration of radiating molecules; fluorescence is such an example. Nonlinear fluorescence microscopes are based on the simultaneous absorption of two (Two-Photon Excited Fluorescence, TPEF [3]) or more photons in the same quantum event. Coherent microscopy, instead, produces optical signals whose phase is rigorously prescribed by a variety of factors – including the excitation light phase and the geometric distribution of the radiating molecules – and whose power is proportional to the n^{th} power of the radiative molecules concentration. Coherent nonlinear techniques are based on the generation of a new photon by combining two or more incident ones, as occurring in Second-Harmonic Generation (SHG [4]), Third-Harmonic Generation (THG [5]) and Coherent Anti-Stokes Raman Scattering (CARS [6]).

Nonlinear microscopy is most often implemented in laser-scanning systems: the focused excitation beam is scanned, point-by-point, along all the regions of interest within the sample. Thus, the signal of interest is synchronously recorded point-by-point. Nonlinear excitation is the main reason for such arrangement. Being second- (or higher) order processes, the above-mentioned techniques require high density of light – both in time and space – for the excitation to happen, and such condition can be achieved only in the beam focus. Therefore, there is no need for spatial filtering in order to eliminate undesired signal coming from out-of-focus planes. Nonlinearity has also another consequence: preventing phototoxic and photodamaging effects, which are particularly relevant for biological samples. In confocal microscopy, by contrast, a very large volume is excited for each scanned point, thus requiring a spatial filter in order to detect only signal coming from the laser beam focus. Therefore, many points of the sample are excited multiple times, increasing the photodamaging risk. Nonlinear techniques, instead, excite only the molecules within the focus, leaving unaltered the other parts of the sample – a very important feature when imaging living (*in vitro* or *in vivo* [7]) organisms. Moreover, such techniques allow an increased penetration depth with respect to single-photon imaging. In fact, the scattering of EM radiation within biological tissues is approximately proportional to $1/\lambda^2$ [8, 9], where λ is its wavelength. Such phenomenon results from a combination of both Rayleigh scattering,

which is proportional to $1/\lambda^4$ (see section 1.2.2), and Mie scattering, which is not strongly wavelength dependent. Thus, longer wavelengths are less scattered, allowing deeper penetration within the sample. Finally, scattered photon in nonlinear microscopy are unable to excite out-of-focus molecules; therefore, as depth increases, the number of scattered photons does as well, but without reducing spatial resolution.

In the following paragraphs, we will discuss the physical theories of the nonlinear optical techniques used in my PhD research: Two-Photon Excited Fluorescence, Second-Harmonic Generation, and Fluorescence Lifetime Imaging Microscopy.

1.1.1 Two-Photon Excited Fluorescence (TPEF) microscopy

An electronic transition can occur following the absorption of a single-photon, but also – as theorized by Maria Goeppert-Mayer in 1931 [10] – by simultaneous absorption of two photons in the same quantum event, provided that the sum of their energies is resonant with the transition. Such phenomenon was first experimentally observed 30 years later, when W. Kaiser and C.G.B. Garrett recorded a two-photon transition in a CaF_2:Eu^{2+} crystal by using a ruby laser as excitation source [11]. However, the application of two-photon microscopy to the study of biological samples was further delayed due to the nonlinear properties of such technique, which requires both high spatial and high temporal density of photons. Since the pulse duration of the first laser sources was too long (~1 ms), the laser power required for observing two-photon transitions would have damaged the sample. Only the development of pulsed femtosecond lasers made possible to implement the first laser-scanning two-photon microscope by W. Denk, J.H. Strickler and W.W. Web in 1990, and to use it for imaging living cells [12].

Two-photon absorption

We will use the time-dependent perturbation quantum theory in order to describe two-photon absorption processes. We can consider a fluorescent molecule as unperturbed system, and an oscillating EM field as perturbation. The Schrödinger equation of the overall system is:

$$i\hbar \frac{\partial \psi}{\partial t} = H\psi \tag{1.1.1}$$

where ψ and H are the wave function and the Hamiltonian of the system, respectively. The last one can be described as the sum of two terms:

(1.1.2) $$H = H_0 + \lambda V(t)$$

where H_0 is the Hamiltonian of the unperturbed system, and $\lambda V(t)$ is the perturbation. Therefore, the steady state, perturbation-free Schrödinger equation is:

(1.1.3) $$H_0 U_n = \varepsilon_n U_n$$

where ε_n and U_n are eigenvalues and eigenfunctions of the unperturbed system, respectively. The temporal evolution of the last one is described by the state Φ:

(1.1.4) $$\Phi = U_n e^{-i\omega_n t}$$

where $\omega_n = \varepsilon_n / \hbar$. Thus, we can use Φ for describing a generic state of the perturbed system as linear combination of eigenstates of the unperturbed system:

(1.1.5) $$\psi = \sum_n c_n(t) U_n e^{-i\omega_n t}$$

where $c_n(t)$ coefficients can be expressed as a power series of λ:

(1.1.6) $$c_k(t) = c_k^{(0)}(t) + \lambda c_k^{(1)}(t) + \lambda^2 c_k^{(2)}(t) + \ldots$$

By substituting the equations 1.1.5 and 1.1.6 in the equation 1.1.1, we get the following equations:

(1.1.7) $$\frac{\partial}{\partial t} c_k^{(0)}(t) = 0$$

(1.1.8) $$\frac{\partial}{\partial t} c_k^{(s+1)}(t) = -\frac{i}{\hbar} \sum_n c_n^{(s)}(t) V_{kn}(t) e^{-i(\omega_n - \omega_k)t}$$

where $V_{kn}(t)$ is the matrix element of the perturbation connecting states n and k:

(1.1.9) $$V_{kn}(t) = \int U_k^* V(t) U_n d^3r$$

Let us suppose that, at $t = 0$, the system occupies one eigenstate of H_0. If U_m is the initial state of the system, and if s is set to 0 (first order) in the equation 1.1.8, we obtain the following relations for c_k coefficients:

(1.1.10) $$c_k^{(0)}(0) = \delta_{km}$$

(1.1.11) $$\frac{\partial}{\partial t} c_k^{(1)}(t) = \frac{1}{i\hbar} V_{km}(t) e^{i\omega_{km} t}$$

where $\omega_{km} = \omega_k - \omega_m = (\varepsilon_k - \varepsilon_m) / \hbar$ is the Bohr frequency. By using the coefficients expansion (at the first order) in the equation 1.1.6 and integrating the equation 1.1.11, we get:

(1.1.12) $$c_k(T) = \delta_{km} + \frac{\lambda}{i\hbar} \int_0^T V_{km}(t)\, e^{i\omega_{km}t}\, dt$$

where T is the time duration of the perturbation. In our case, the perturbing field is an oscillating EM field, thus $V(t)$ perturbation can be expressed as:

(1.1.13) $$V(t) = \frac{\mu E_0}{2}\, e^{i\omega t} + \frac{(\mu E_0)^*}{2}\, e^{-i\omega t}$$

where E_0 is the electric field amplitude, ω is its oscillating frequency and μ is the electric dipole moment of the molecule. By substituting the equation 1.1.13 in the equation 1.1.12 and setting $k \neq m$, we get the following expression for $c_k^{(1)}$ coefficients:

(1.1.14) $$c_k^{(1)}(T) = -\frac{1}{2\hbar}\left[(\mu E_0)_{km}\, \frac{e^{i(\omega_{km}+\omega)T}-1}{\omega_{km}+\omega} + (\mu E_0)^*_{km}\, \frac{e^{i(\omega_{km}-\omega)T}-1}{\omega_{km}-\omega} \right]$$

If the electric field oscillating frequency is close to the Bohr frequency between U_k and U_m states (i.e. $\omega \approx \omega_{km}$), then the first term of the equation 1.1.14 is negligible. The square module of the $c_k^{(1)}$ coefficient is the probability of finding the system in the U_k state after a time T and, after some calculation, its expression become:

(1.1.15) $$\left|c_k^{(1)}(T)\right|^2 \approx \frac{E_0^2}{\hbar^2}\, |\mu^*_{km}|^2\, \frac{\sin^2\left(\frac{\omega_{km}-\omega}{2}T\right)}{(\omega_{km}-\omega)^2}$$

Dividing by the time T, we get the transition probability per unit of time between U_m and U_k states, which is the transition probability for single-photon absorption:

(1.1.16) $$\frac{\left|c_k^{(1)}(T)\right|^2}{T} \approx \frac{E_0^2}{\hbar^2}\, |\mu^*_{km}|^2\, \frac{\sin^2\left(\frac{\omega_{km}-\omega}{2}T\right)}{(\omega_{km}-\omega)^2\, T}$$

In particular, the transition probability depends on (1) the square of the electric field amplitude (in our case, of the light intensity) and (2) the square of the matrix element of the electric dipole moment between the two involved states.

The transition from U_m state to U_k state can occur also by simultaneous absorption of two photons. In order to derive the probability of two-photon absorption, we have to consider the second order of the above-described perturbation theory. Let us suppose that an "intermedi-

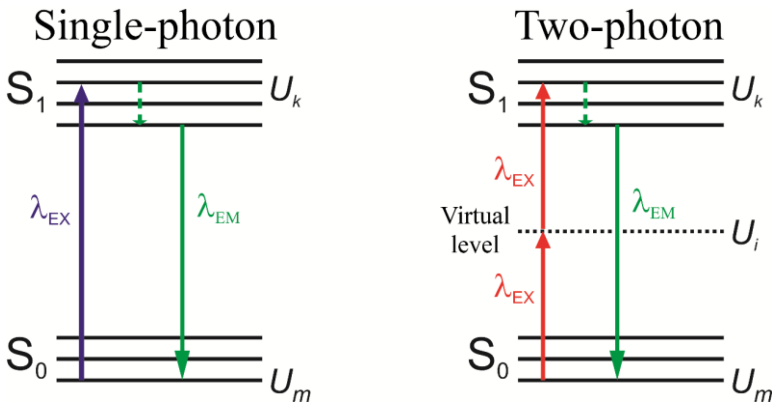

Figure 1.1 Energy level diagrams for single-photon (left) and two-photon (right) absorption. The two-photon transition diagram shows the simultaneous absorption of two photons, i.e. the possibility to observe a transition between the states U_m and U_k through an intermediate virtual state U_i.

ate" virtual state U_i exists, with $i \neq m$ and $i \neq k$, and that V_{im} and V_{ik} values are different from zero. Then, the expression for the first order coefficient for the U_i state is:

(1.1.17) $$c_i^{(1)}(T) = \frac{1}{i\hbar} \int_0^T V_{im}(t)\, e^{i\omega_{im}t}\, dt$$

By substituting $s = 1$ in the equation 1.1.8, we get the following equation for the second order coefficient of the U_k state:

(1.1.18) $$\frac{\partial}{\partial t} c_k^{(2)}(t) = -\frac{i}{\hbar} \sum_i c_i^{(1)}(t)\, V_{ki}(t)\, e^{i\omega_{ki}t}$$

By substituting the equation 1.1.17 in the equation 1.1.18, and then integrating it, we get:

(1.1.19) $$c_k^{(2)}(T) = \frac{1}{(i\hbar)^2} \sum_i \int_0^T V_{ki}(t) e^{i\omega_{ki}t}\, dt \int_0^t V_{im}(t')\, e^{i\omega_{im}t'}\, dt'$$

By substituting the equation 1.1.13 in the equation 1.1.19, we get:

(1.1.20) $$c_k^{(2)}(T) = -\frac{E_0^2}{4(i\hbar)^2} \sum_i \int_0^T \left(\mu_{ki}\, e^{i\omega t} + \mu_{ki}^*\, e^{-i\omega t}\right) e^{i\omega_{ki}t}\, dt \int_0^t \left(\mu_{im}\, e^{i\omega t} + \mu_{im}^*\, e^{-i\omega t}\right) e^{i\omega_{im}t'}\, dt'$$

Finally, the square module of the equation 1.1.20 is:

(1.1.21) $$\left|c_k^{(2)}(T)\right|^2 = \frac{E_0^4}{16\,\hbar^4} \left|\sum_i \int_0^T \left(\mu_{ki}\, e^{i\omega t} + \mu_{ki}^*\, e^{-i\omega t}\right) e^{i\omega_{ki}t}\, dt \int_0^t \left(\mu_{im}\, e^{i\omega t} + \mu_{im}^*\, e^{-i\omega t}\right) e^{i\omega_{im}t'}\, dt'\right|^2$$

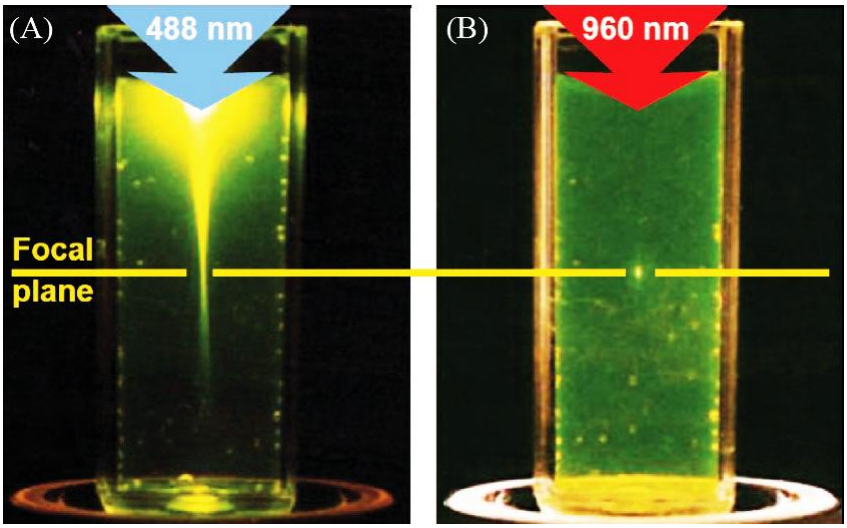

Figure 1.2 Comparison between two excitation volumes. A): single-photon excitation in a fluorescein cuvette by focused (NA = 0.16) 488 nm light. B): two-photon excitation in the same cuvette using focused (NA = 0.16) femtosecond pulses of 960 nm light [13].

Therefore, two-photon transition probability is proportional to the fourth power of the electric field amplitude. At the second order of the perturbation theory, two-photon transition probability is proportional to the square of light intensity; single-photon transition probability, instead, is linearly proportional to light intensity.

(1.1.22) $$\left|c_k^{(2)}(T)\right|^2 \propto I_0^2$$

Such difference between single- and two-photon transitions is particularly relevant in optical sectioning of biological samples – as we will discuss in the following paragraphs.

Image formation

When excited by a two-photon transition, a molecule emits fluorescence light, whose intensity is proportional to the transition probability. The latter is, in turn, proportional to the square of the excitation light intensity (as discussed in the previous section). Therefore, one advantage of two-photon excitation – with respect to single-photon absorption – is to reduce photobleaching, i.e. the photochemical alteration of fluorescent molecules. In fact, the probability of second order processes being very low, excitation requires high density of light both in time and in space. Such density is achieved only in a small volume (typically of the order of 1 femtolitre) around the focus – as demonstrated in the following section – thus only molecules enclosed in that region can be excited. Laser scanning on the focal plane

does not affect out-of-focus molecules (see figure 1.2), avoiding photodamaging and other phototoxic effects. For the same reason, optical sectioning does not require a spatial filter (pinhole) for removing out-of-focus fluorescence – as opposed to confocal microscopy.

Moreover, as mentioned before, the main advantage of two-photon microscopy consists in deeper penetration in turbid samples (as the biological ones) by using longer wavelengths. In fact, penetration depth in biological samples is strongly limited due to elastic scattering of light, which is proportional to the factor $1/\lambda^4$. With respect to single-photon excitation, two-photon microscopy uses twice the wavelength, thus reducing scattering and increasing penetration. Another limiting factor for penetration depth is absorption, which – for biological samples – is typically strong in the visible spectrum and for ultraviolet light. However, the same transition that requires single-photon absorption of visible light can be excited by two-photon absorption of infrared light, effectively reducing the excitation beam absorption. In fact, when scattered by molecules inside the sample, exciting photons do not reach the focal volume, thus preventing any out-of-focus excitation. Spatial resolution is, therefore, unaffected by increasing depth of the focal plane within a turbid sample.

For all these reasons, in the last 27 years two-photon microscopy became one of the most used tools for studying cells and biological tissues. Let us now calculate the 3D spatial extent of a Gaussian beam focus, when it is focused by a high numerical aperture (NA) objective.

Spatial resolution

In laser microscopy, the excitation volume dimensions determine spatial resolution. In fact, the excitation volume determines the Point Spread Function (PSF) of the optical system, i.e. the system optical response to a point light source. The smaller is the PSF Full Width at Half Maximum (FWHM), the better is the spatial resolution.

As shown in the equation 1.1.16, single-photon transition probability is proportional to light intensity, meaning that the single-photon excitation volume is determined by the light intensity distribution around the focal point. For a confocal microscope, the pinhole – used for rejecting out-of-focus fluorescence photons – generates a new PSF in the optical system, which is multiplied by the excitation volume PSF. The product between the two PSFs is in turn a PSF, whose FWHM is smaller with respect to the initial one.

As shown in the equation 1.1.22, two-photon transition probability is proportional to the square of light intensity, meaning that the two-photon excitation volume is determined by the square of the light intensity distribution around the focal point. Therefore, as discussed in the previous section, there is no need for using a pinhole; two-photon spatial resolution is already comparable to that one of a confocal microscope.

We want now to calculate the intensity distribution *I(x,y,z)* near to the focus of a TEM_{00} laser beam, focused by a circular aperture objective lens. Given a cylindrical coordinate system (ρ, z, θ) with the origin in the focus, we can neglect the angular coordinate θ because of rotational invariance. Thus, we are interested only in the radial and axial dependence of light intensity near the focus. Let us change the dimensional coordinates ρ, z to the dimensionless coordinates v, u defined as:

(1.1.23) $$v = \frac{2\pi\rho\ NA}{\lambda}$$

(1.1.24) $$u = \frac{2\pi z\ (NA)^2}{n\lambda}$$

where *NA* is the objective lens numerical aperture, λ is the laser wavelength, and n is the surrounding medium refractive index. Complex amplitude of the electric field near the focus of an aberration-free, circular aperture lens can be expressed [14, 15] as a function of v, u coordinates, as in the following integral:

(1.1.25) $$E(v,u) = 2\int_0^1 J_0(v\rho)\, e^{-\frac{iu\rho^2}{2}}\, \rho\, d\rho$$

where $J_0(v\rho)$ is the zero order Bessel function of the first kind. Therefore, we can write the intensity distribution near the focal point as follows:

(1.1.26) $$I(\rho,z) = I(v,u) = I_0\, |E(v,u)|^2$$

where I_0 is the electric field intensity near the focal point, i.e. measured at the coordinates $\rho = z = 0$ or $v = u = 0$. In order to separately calculate intensity radial and axial distributions, we can solve the integral in the equation 1.1.25 by alternatively substituting $u = 0$ or $v = 0$. Thus, the intensity radial distribution is equal to:

(1.1.27) $$|E(v,0)|^2 = \left|2\int_0^1 J_0(v\rho)\, \rho\, d\rho\right|^2$$

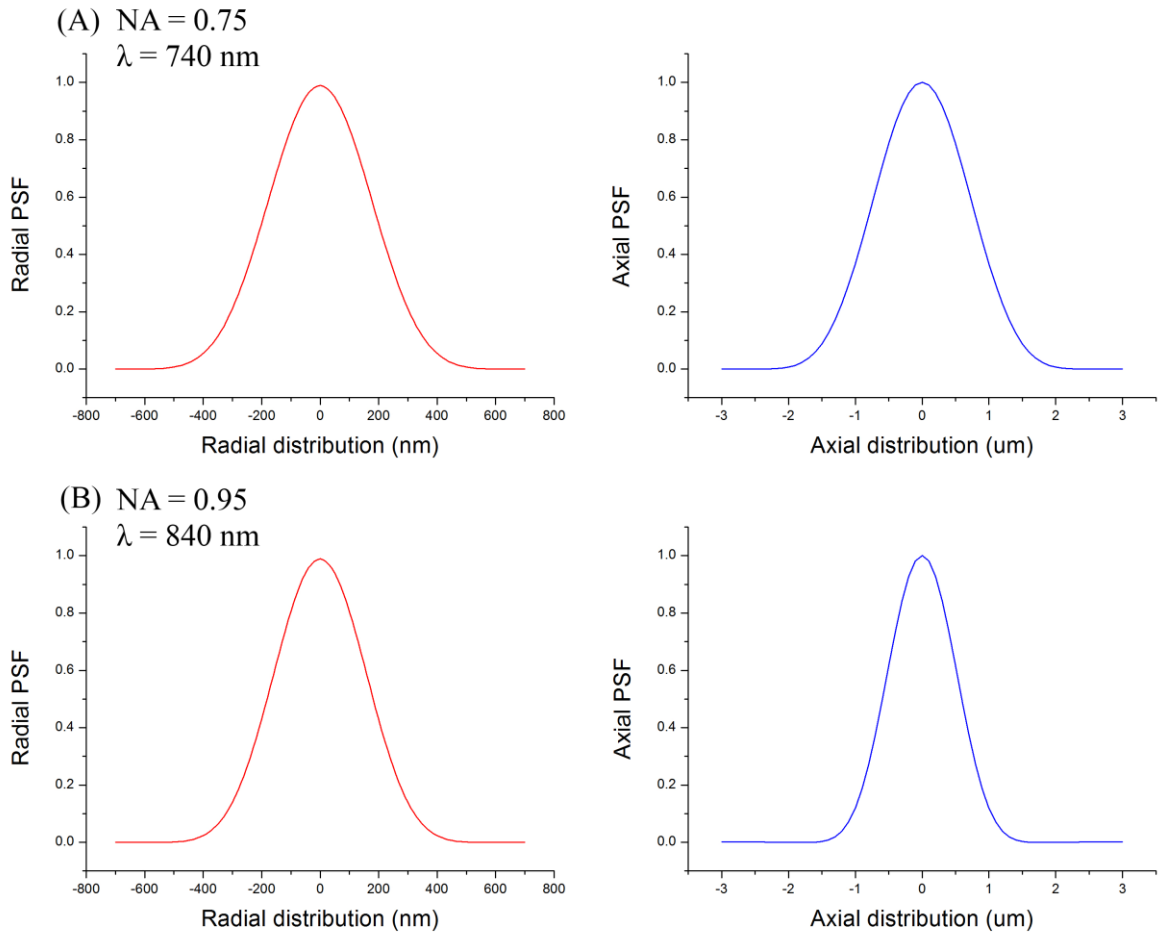

Figure 1.3 A): radial (top-left, red) and axial (top-right, blue) theoretical PSFs for two-photon fluorescence, calculated for an objective with NA = 0.75, focusing a laser beam with λ = 740 nm into air (n = 1.0003). B): radial (bottom-left, red) and axial (bottom-right, blue) theoretical PSFs for two-photon fluorescence, calculated for an objective with NA = 0.95, focusing a laser beam with λ = 840 nm into air.

and the intensity axial distribution equals:

(1.1.28) $$|E(0,u)|^2 = \left|2\int_0^1 e^{-\frac{iu\rho^2}{2}}\,\rho\,d\rho\right|^2$$

By solving the two integrals, we get the following expressions:

(1.1.29) $$|E(v,0)|^2 = \left|\frac{2J_1(v)}{v}\right|^2$$

(1.1.30) $$|E(0,u)|^2 = \left|\frac{sen(u/4)}{u/4}\right|^2$$

Then we can calculate the radial and axial PSFs for a two-photon transition by squaring the last two expressions:

(1.1.31) $$PSF_{rad} = \left|\frac{2\,J_1(v)}{v}\right|^4$$

(1.1.32) $$PSF_{ax} = \left|\frac{sen(u/4)}{u/4}\right|^4$$

These two equations describe radial and axial PSFs (PSF_{rad} and PSF_{ax}, respectively) for two-photon excitation. For example, let us consider an objective with NA = 0.75, focusing a laser beam with λ = 740 nm into air (n = 1.0003), and another one with NA = 0.95, focusing a laser beam with λ = 840 nm into air. Figure 1.3 shows the radial and axial PSFs of the two objectives. FWHM of the axial and radial PSFs represent axial and radial spatial resolutions of the microscope, respectively. In our case, axial and radial resolution are, respectively, 1.7 μm and 400 nm for the NA = 0.75 objective; 1.2 μm and 360 nm for the NA = 0.95 objective.

1.1.2 Second-Harmonic Generation (SHG) microscopy

Two-photon absorption is not the only NLO process for imaging biological samples. In fact, some biological molecules can be properly excited for generating higher-order harmonics.

Second-harmonic generation (SHG) consists in a material generating EM radiation with twice the frequency of the incident EM field. Such phenomenon was firstly used in spectroscopy and later (during the '70s) applied for microscopic imaging [16-18]. Recently, SHG microscopy has become a powerful tool for imaging cells [19], cell membranes [20], tissues [21] and in particular collagen in connective tissues [22].

SHG is a second-order NLO process occurring in non-centrosymmetric materials with large hyperpolarizability. In NLO, a molecule interacts with a driving electric field through both its intrinsic electric dipole moment and the induced electric dipole moment. In general, the electric dipole moment can be expressed as a power series of the electric field:

(1.1.33) $$\mu = \mu_0 + \alpha E + \frac{1}{2}\beta E^2 + \frac{1}{6}\gamma E^3 + \cdots$$

where μ_0 is the permanent electric dipole moment; α is the polarizability related to a linear process (as single-photon absorption and reflection); β is the first hyperpolarizability, which is related to second-order processes (as second-harmonic, sum and difference frequency gen-

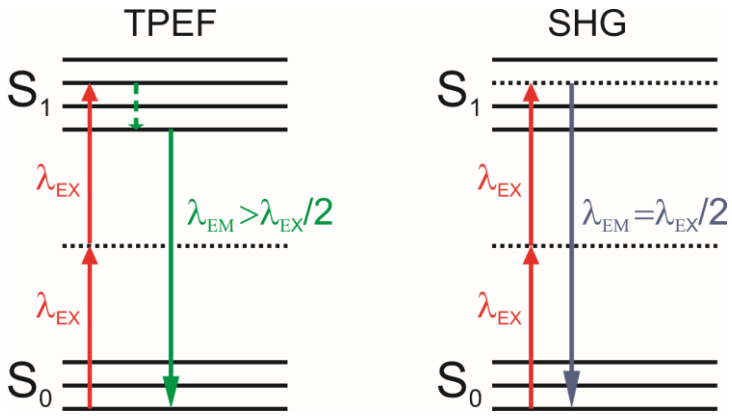

Figure 1.4 Comparison between the energy level diagrams of two-photon fluorescence (on the left) and second-harmonic generation (on the right).

eration); γ is the second hyperpolarizability, which is related to third-order phenomena (as light scattering, third-harmonic generation and two- or three-photon absorption).

Harmonic generation is an optical phenomenon involving coherent radiative scattering, whereas fluorescence generation involves incoherent radiative absorption and re-emission (figure 1.4). Therefore, fluorescence imaging is based on a completely different mechanism from harmonic generation. Moreover, due to its coherent properties, harmonic radiation is highly directional and depends critically on the spatial distribution of the emitters within the focal volume, thus SHG is a more complex phenomenon to be described than fluorescence. In the following paragraphs, we will describe the case of SHG from a particular distribution of second-harmonic emitters, excited by a highly focused laser beam (as in high-resolution microscopy).

Single molecule SHG cross section

In this section, we will determine the SHG cross section of a single molecular scatterer. We can approximate a molecule as an elemental dipole radiator, driven by the excitation light proportionally to its first hyperpolarizability. Also, for simplicity, let us assume the excitation electric field to be linearly polarized along the z axis and let us consider only the component β_{zzz} of the hyperpolarizability tensor β. If ω is the excitation light frequency, then the induced electric dipole moment at frequency 2ω is equal to:

(1.1.34) $$\vec{\mu}_{2\omega} = \frac{1}{2}\,\beta_{zzz}\,E_{\omega}^{2}\,\hat{z}$$

where E_ω is the excitation field amplitude. In far-field approximation, the radiated second-harmonic field at an angle ψ from the z axis is:

(1.1.35) $$\vec{E}_{2\omega}(\psi) = -\frac{\omega^2 \mu_{2\omega}}{\pi \varepsilon_0 c^2 r} \sin(\psi)\ e^{-i2\omega t}\ \hat{\psi}$$

where ε_0 is the vacuum permittivity, c is the speed of light, r is the observation distance from the dipole, t is the corresponding delay time. The resulting power per differential solid angle at the inclination ψ can be expressed (in photons/second units) as:

(1.1.36) $$P_{2\omega}(\psi) = \frac{3}{16\,\pi}\ \sigma_{SHG}\ sin^2(\psi)\ I_\omega^2$$

where I_ω is the excitation intensity (expressed in photons/second per unit area) and σ_{SHG} is the SHG cross sections defined as:

(1.1.37) $$\sigma_{SHG} = \frac{4 n_{2\omega}\ \hbar \omega^5}{3\pi n_\omega^2\ \varepsilon_0^3 c^5}\ |\beta_{zzz}|^2$$

where n_ω and $n_{2\omega}$ are the medium refractive indexes at frequency ω and 2ω, respectively. By integrating the equation 1.1.36 over all solid angles, we obtain a simple expression for the emitted power in terms of the SHG cross section:

(1.1.38) $$P_{SHG} = \frac{1}{2}\ \sigma_{SHG}\ I_\omega^2$$

Similarly, we can express the fluorescence power emitted by an electric dipole undergoing two-photon excitation as:

(1.1.39) $$P_{TPE} = \frac{1}{2}\ \sigma_{TPE}\ I_\omega^2$$

where σ_{TPE} is the product between the two-photon fluorescence cross section and the fluorescence quantum yield [23]. Then, we can express σ_{TPE} and σ_{SHG} in the same units for a direct comparison.

Therefore, the SHG power - as the two-photon one - is proportional to the square of the excitation intensity. As discussed in section 1.1.1, there are three resulting advantages: better spatial resolution, deeper penetration in biological samples, and lower probability of photobleaching and photodamaging. In fact, since SHG is based on a scattering process, the energy transferred to the sample by the incident photons is negligible.

Generalized SHG theory

Let us now consider the SHG emission from a generic spatial distribution of radiating dipoles, driven by a focused Gaussian beam.

The electric field of a highly focused excitation beam with frequency ω, propagating along the optical axis z and polarized in a generic direction $\hat{e}$, can be expressed as:

$$\vec{E}(\vec{x}) = -iE_{\omega} \exp\left(-\frac{x^2+y^2}{w_{\rho}^2} - \frac{z^2}{w_z^2} + i\xi z k_{\omega}\right) \hat{e} \tag{1.1.40}$$

where w_ρ and w_z are the radial and axial beam waists, respectively; $\hat{e}$ is a unit vector in the xy plane; $k_\omega = n\omega/c$, where n is the medium refractive index; ξ is the effective reduction in the axial propagation vector caused by phase anomaly, or Gouy shift [24]. The resulting local second-harmonic dipole moment per unit concentration of emitters is given by:

$$\vec{\mu}_{2\omega,i}(\vec{x}) = \frac{1}{2} E_{\omega}^2(\vec{x}) \sum_{j,k} \langle \beta_{ijk} \rangle \hat{e}_j \hat{e}_k \tag{1.1.41}$$

where $\langle \beta_{ijk} \rangle$ is the local ensemble-averaged hyperpolarizability unit density.

Since SHG is a coherent process, the total power and the angular distribution of the emitted radiation depend on how the emitters are spatially distributed within the focal volume. As shown in figure 1.5, we can define three unit vectors $\hat{r}$, $\hat{\theta}$, $\hat{\varphi}$ corresponding to the propagation direction, the p polarization direction and the s polarization direction, respectively. These three unit vectors are defined by the following expressions:

$$\hat{r} = \sin(\theta)\cos(\varphi)\ \hat{x} + \sin(\theta)\sin(\varphi)\ \hat{y} + \cos(\theta)\ \hat{z} \tag{1.1.42}$$

$$\hat{\theta} = \cos(\theta)\cos(\varphi)\ \hat{x} + \cos(\theta)\sin(\varphi)\ \hat{y} - \sin(\theta)\ \hat{z} \tag{1.1.43}$$

$$\hat{\varphi} = -\sin(\varphi)\ \hat{x} + \cos(\varphi)\ \hat{y} \tag{1.1.44}$$

Let us consider first the second-harmonic electric far-field radiated in the direction $\{\theta,\varphi\}$, hereafter indicated by Θ, from a single isolated emitter located exactly in the focus. It can be decomposed in its p and s polarization components:

$$\vec{E}_{2\omega}^{(0)}(\Theta) = \begin{pmatrix} \vec{E}_{2\omega}^{(0)p}(\Theta) \\ \vec{E}_{2\omega}^{(0)s}(\Theta) \end{pmatrix} = \frac{\eta}{r} M \cdot \vec{\mu}_{2\omega}(0) \tag{1.1.45}$$

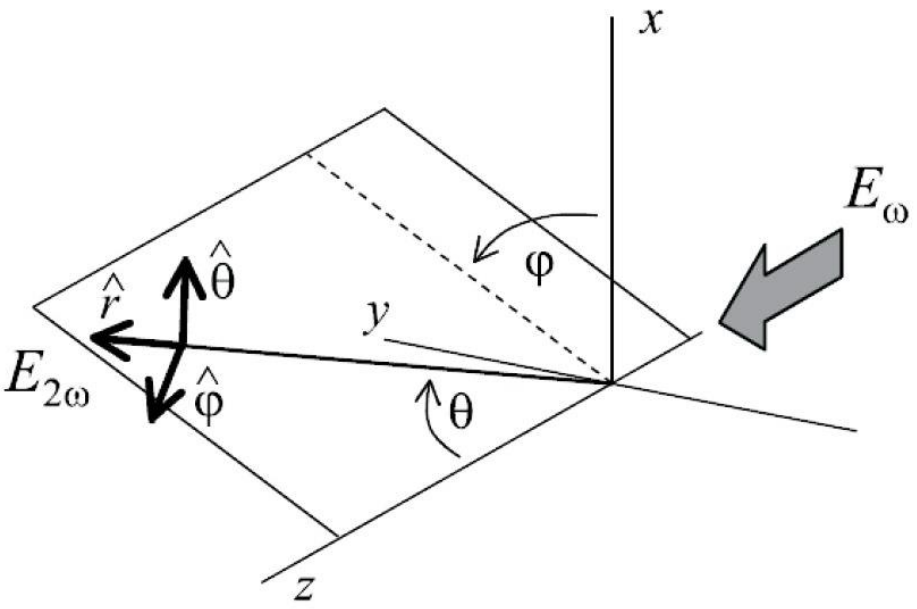

Figure 1.5 Coordinate system. The excitation beam propagates along the *z* axis. The SHG signal propagates along the $\hat{\boldsymbol{r}}$ direction, defined by $\{\theta,\varphi\}$. θ and φ correspond to the *p* and *s* polarization directions, respectively.

where $\eta = \omega^2/\pi\varepsilon_0 c^2$; r is the far-field propagation distance ($rk_\omega \gg 1$) with respect to the observer; M is the projection matrix, defined as:

(1.1.46) $$M\begin{pmatrix}\hat{\theta}\\ \hat{\varphi}\end{pmatrix} = \begin{pmatrix}\cos(\theta)\cos(\varphi) & \cos(\theta)\sin(\varphi) & -\sin(\theta)\\ -\sin(\varphi) & \cos(\varphi) & 0\end{pmatrix}$$

For simplicity, we assumed $n_\omega \approx n_{2\omega}$. The equation 1.1.45 can now be generalized for describing the far-field radiation generated by a collection of emitters with an arbitrary concentration distribution, defined by $N(\vec{x})$.

(1.1.47) $$\vec{E}_{2\omega}(\Theta) = \frac{\eta}{r}\int N(\vec{x})\, M \cdot \vec{\mu}_{2\omega}(\vec{x})\, e^{-ik_{2\omega}\,\vec{x}\cdot\hat{r}}\, d\vec{x}$$

where we assumed $\langle\beta\rangle$ to be position-independent. We can now expand $N(\vec{x})$ in its Fourier components, defined as:

(1.1.48) $$N(\vec{q}) = \left(\frac{k_{2\omega}}{2\pi}\right)^d \int N(\vec{x})\, e^{-ik_{2\omega}\,\vec{q}\cdot\vec{x}}\, d\vec{x}$$

where $\vec{q}$ represents a spatial wave vector normalized to $k_{2\omega}$, and d is the dimensionality of the emitters distribution. Thus, the total radiated field is given by the coherent summation of contributions of the local induced polarization at all points in the space:

(1.1.49) $$\vec{E}_{2\omega}(\Theta) = V_{(d)}\, \vec{E}_{2\omega}^{(0)}(\Theta) \int N(\vec{x})\, A_{(d)}(\Omega, \vec{q})\; d\vec{q}$$

where $V_{(d)}$ is the active SHG "volume" (corresponding to a length, an area or a volume for d = 1, 2 or 3, respectively) and $A_{(d)}$ is the "antenna" factor arising from the phased summation of the radiated fields from the distributed sources, also dependent on the dimensionality. If we define three components of this "antenna" factor as follows

(1.1.50) $$A_x = \exp\left(\frac{-k_{2\omega}^2\, w_\rho^2\, [\sin(\theta)\cos(\varphi) - q_x]^2}{8}\right)$$

(1.1.51) $$A_y = \exp\left(\frac{-k_{2\omega}^2\, w_\rho^2\, [\sin(\theta)\sin(\varphi) - q_y]^2}{8}\right)$$

(1.1.52) $$A_z = \exp\left(\frac{-k_{2\omega}^2\, w_z^2\, [\cos(\theta) - \xi - q_z]^2}{8}\right)$$

we can then consider three different cases, corresponding to three different geometries of the problem. If the sources are uniformly distributed along a one-dimensional line in the z direction (x, y = 0), then:

(1.1.53) $$V_{(1)} = \left(\frac{\pi}{2}\right)^{1/2} w_z$$

(1.1.54) $$A_{(1)} = A_z$$

If the sources are distributed on a two-dimensional surface in the yz plane (x = 0), then:

(1.1.55) $$V_{(2)} = \left(\frac{\pi}{2}\right) w_\rho\, w_z$$

(1.1.56) $$A_{(2)} = A_y\, A_z$$

If they are distributed in a three-dimensional volume, then:

(1.1.57) $$V_{(3)} = \left(\frac{\pi}{2}\right)^{3/2} w_\rho^2\, w_z$$

(1.1.58) $$A_{(3)} = A_x\, A_y\, A_z$$

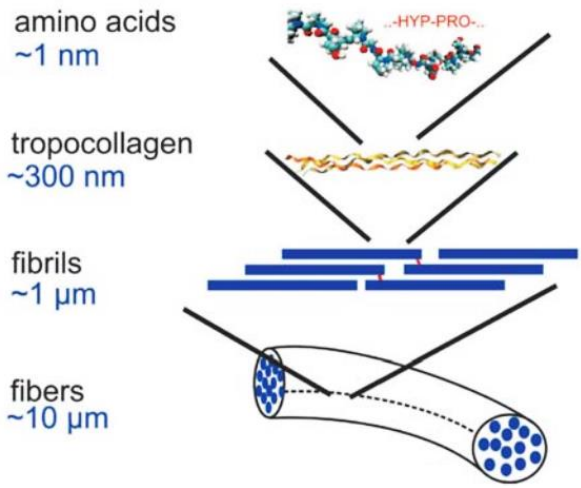

Figure 1.6 Collagen hierarchical organization. Picture taken from [25].

Finally, the resulting SHG power emitted in the unit of solid angle in the direction Ω is given by:

(1.1.59) $$P_{2\omega}(\Omega) = \frac{1}{2}\, n\varepsilon_0 c r^2 \left|\vec{E}_{2\omega}(\Theta)\right|^2$$

We will apply such result in the next paragraph, while discussing the SHG emission from collagen. Such topic is particularly important for SHG imaging of a great variety of biological tissues.

SHG from collagen

Collagen is the main structural protein in the extracellular space of connective tissues in animal bodies (figure 1.6). Its basic unit is the tropocollagen, a 300 nm long molecule with a diameter of 1.5 nm. Tropocollagen has three subunits (or chains), each one containing 1050 amino acids, wrapped to form a right-handed triple helix. Tropocollagen molecules arrange themselves into collagen fibrils, each one with a diameter ranging from 50 to 200 nm. Fibrils, aligned side-by-side, form fibre bundles. SHG emitters are localized in peptide bonds of the amino acid chain. Thus, the triple helix molecular structure of collagen causes the SHG emitters to be well organized into a helicoidal distribution, resulting in a high degree of anisotropy. The latter, together with the high hyperpolarizability within peptide bonds, allows imaging collagen fibres through SHG microscopy [26, 27].

Let us consider now two particular geometries of SHG emitters, corresponding to a collagen fibre either aligned to the optical axis or lying on the focal plane. For simplicity, in the following model we will assume the emitter dipoles to be orthogonal to the fibre axis – instead of their more complex helicoidal geometry distribution.

Let us first consider the case of a collagen fibre aligned to the optical axis. In our model, the excitation laser is polarized along the *y* axis, and the hyperpolarizability of each emitter is uni-axial and also directed along the *y* axis.

We assume the emitters to be uniformly distributed along the *z* axis, with constant density N_1 per unit length. Therefore, by using the formulas derived in the previous paragraph, we obtain a distribution in the Fourier space of $N(\vec{q}) = \delta(0)$. Consequently:

(1.1.60) $$\vec{E}_{2\omega}(\Theta) = \left(\frac{\pi}{2}\right)^{1/2} w_z \, \vec{E}_{2\omega}^{(0)}(\Theta) \, N \exp\left(\frac{-k_{2\omega}^2 \, w_z^2 \, [\cos(\theta) - \xi]^2}{8}\right)$$

Then, the SHG power per unit of solid angle is given by:

(1.1.61) $$P_{2\omega}(\Omega) = \frac{\pi n \varepsilon_0 c r^2 w_z^2}{4} \, N^2 \left|\vec{E}_{2\omega}^{(0)}(\Theta)\right|^2 \exp\left(\frac{-k_{2\omega}^2 \, w_z^2 \, [\cos(\theta) - \xi]^2}{4}\right)$$

The resultant SHG radiation power is confined to a forward directed off-axis cone, as depicted in figure 1.7. The angular deviation from the optical axis is given by:

(1.1.62) $$\theta_{peak} \approx cos^{-1}(\xi)$$

which also corresponds to the angle with maximum emitted power. In this case, the SHG power is proportional to the square of the emitter dipoles (N^2) – while TPEF power is proportional to *N*. Such difference arises from the coherent nature of the SHG process.

Let us consider now the case of the collagen fibre emitter dipoles aligned to the *y* axis, instead of the optical axis. Again, the excitation laser is polarized along the *y* axis, and the hyperpolarizability of each emitter is uni-axial and also directed along the *y* axis. For simplicity, we assume the emitters to be uniformly distributed along the *y* axis, with constant density *N* per unit of length (as in figure 1.8). In this case, too, the emitters distribution in the Fourier space is a one-dimensional δ-function in the q_y space. Therefore, the total SHG

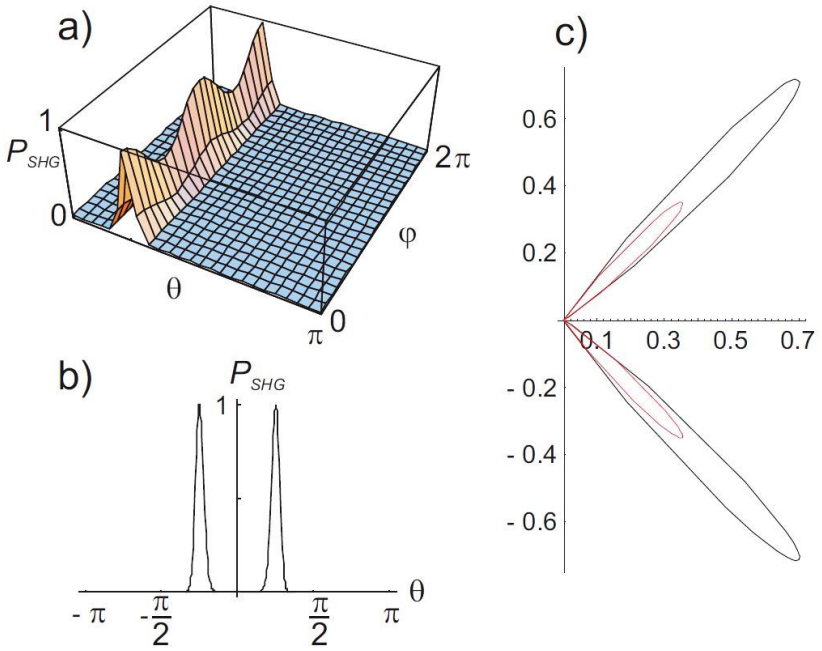

Figure 1.7 Angular distribution of SHG emitted by a uniform distribution of *z*-aligned, *y*-polarized dipoles, excited by a *z*-propagating, *y*-polarized propagating beam. In a) we plotted its dependence from angles θ e φ. In b) we plotted the $\varphi = 0$ case. The two peaks showed in b) correspond to the $cos^{-1}(\xi)$ values. In c) we represented the polar diagram of the SHG emission for the *xz* plane (black line) and for the *yz* plane (red line); the *z* direction is reported in abscissa. The calculation was done using the following parameters: λ = 840 nm (excitation wavelength), ξ = 0.7 (phase anomaly), w_z = 1600 nm (axial beam *waist*). Picture taken from [28].

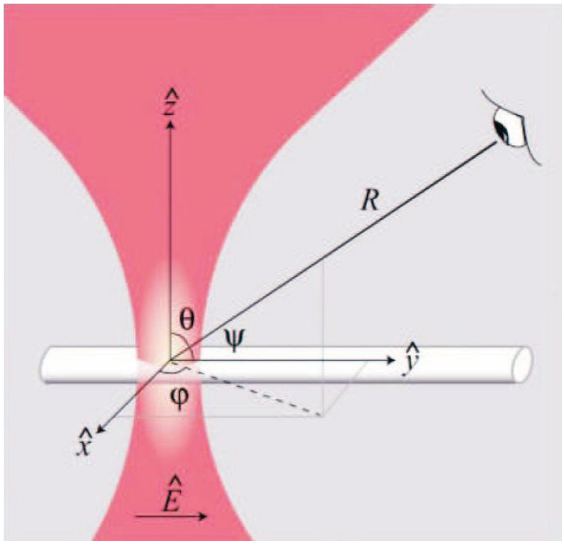

Figure 1.8 Diagram of coordinate system for calculating the total emitted SHG field from a uniform distribution of nonlinear emitters along a *y*-aligned fibre. The excitation light is directed along the *z* axis and polarized along the *y* axis. Nonlinear induced emitting dipoles are assumed to be *y*-polarized.

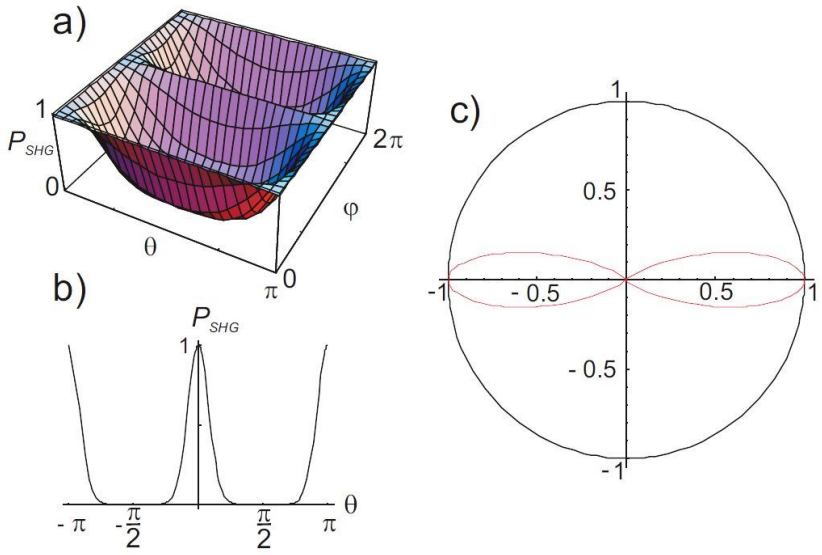

Figure 1.9 Angular distribution of SHG emitted by a uniform distribution of *y*-aligned, *y*-polarized dipoles, excited by a *z*-propagating, *y*-polarized propagating beam. In a) we plotted its dependence from angles θ e φ. In b) we plotted the $\varphi = \pi/2$ case. SHG emission is equally distributed both in forward and backward directions. In c) we represented the polar diagram of the SHG emission for the *xz* plane (black line) and for the *yz* plane (red line); the *z* direction is reported in abscissa. The calculation was done using the following parameters: λ = 840 nm (excitation wavelength), ξ = 0.7 (phase anomaly), w_z = 350 nm (axial beam *waist*). Picture taken from [28].

far-field per unit of solid angle is given by:

$$\vec{E}_{2\omega}(\Theta) = \left(\frac{\pi}{2}\right)^{1/2} w_\rho \, \vec{E}_{2\omega}^{(0)}(\Theta) \, N \exp\left(\frac{-k_{2\omega}^2 \, w_\rho^2 \, sin^2(\theta) \, sin^2(\varphi)}{8}\right) \tag{1.1.63}$$

and the total emitted SHG power per unit of solid angle is equal to:

$$P_{2\omega}(\Omega) = \frac{\pi n \varepsilon_0 c r^2 w_\rho^2}{4} \, N^2 \left|\vec{E}_{2\omega}^{(0)}(\Theta)\right|^2 \exp\left(\frac{-k_{2\omega}^2 \, w_\rho^2 \, sin^2(\theta) \, sin^2(\varphi)}{4}\right) \tag{1.1.64}$$

The main difference with respect to the previous case consists in the different "antenna" factor *A*, resulting in a different angular distribution (see figure 1.9).

In general, SHG radiation can be emitted both forward and backward with respect to the excitation light direction. The emitted SHG angular distribution depends on the angle between the excitation field direction and the hyperpolarizability direction (e.g. the direction of the fibrils in the case of collagen). The ratio between the forward-directed and the backward-directed SHG signals varies with the same angle, as depicted in figure 1.10. The main SHG contribution is usually directed as the excitation light. In the case of the collagen

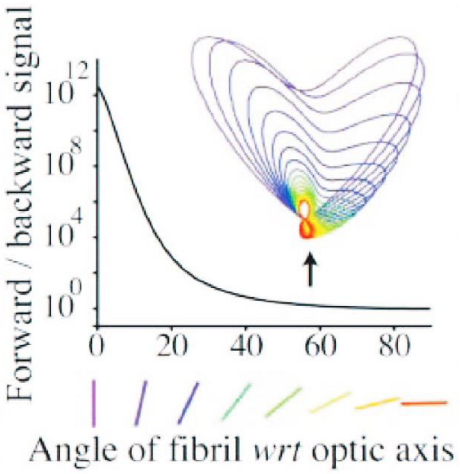

Figure 1.10 SHG forward/backward ratio versus the angle between collagen fibrils and the optical axis. Above the graph, the expected angular distribution of SHG emission is reported for different angles between the fibrils and the optical axis (the latter is indicated by the black arrow). Picture taken from [29].

SHG emission from tissues, SHG light can be detected in both forward and backward directions.

Thin tissue samples – less than 1 mm thickness – can be studied through both forward and backward detection (even if backward signal is usually small). Instead, for samples more than 1 mm thick, only backward detection is allowed, since their thickness prevents detecting the forward emission. In the latter case, however, forward-emitted SHG signal can be backward scattered by the sample molecules, thus enhancing the backward-emitted signal; such effect occurs only in highly scattering media, as biological tissues.

1.1.3 Fluorescence Lifetime Imaging Microscopy (FLIM)

Since the end of the ‘80s, time-resolved fluorescence spectroscopy has been widely used for studying the emission dynamics of fluorescent molecules – as, for example, the time distribution of a molecule radiative decay after its excitation to an upper electronic energy level [30, 31]. The time extension of such distribution is referred to as the fluorescence lifetime of the molecule. Lifetime measurements can yield information on the molecular microenvironment of a fluorescent molecule. In general, everything influencing the non-radiative decay channel width (see figure 1.11) of the molecule – e.g. ionic bonds, oxygen

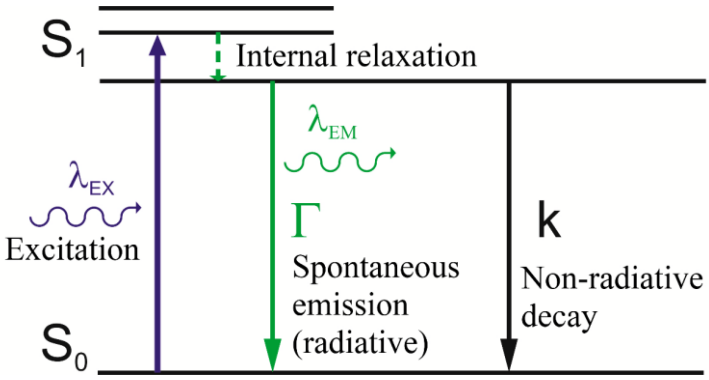

Figure 1.11 Energy diagram for the absorption-emission process. In evidence the two decay rate constants *Γ* and *k* for radiative and non-radiative decay processes, respectively.

concentration, collisions and energy exchanges with other molecules – can affect its fluorescence lifetime.

At the beginning of the 90's, this field has been revolutionized by the development of fluorescence lifetime imaging microscopy (FLIM [32, 33]). Such technique generates an image of the sample based on the mean lifetime measured at each pixel. Fluorescence lifetime imaging has been implemented in wide-field [32], confocal [34] and multiphoton microscopes [35]. FLIM couples the advantages of fluorescence microscopy and time-resolved spectroscopy by revealing the spatial distribution of fluorescent molecules together with information about their microenvironment.

Fluorescence mean lifetime

The fluorescence lifetime of a molecule usually represents its average permanence time in the excited state, before decaying to the ground state. If we consider an ensemble of molecules, excited by an infinitely short pulse of light, resulting in an initial population N_0 in the excited state, then the decay rate of the latter is:

(1.1.65) $$\frac{d}{dt}N(t) = -(\Gamma + k)\,N(t)$$

where $N(t)$ is the number of molecules in the excited state at time t, Γ and k are the radiative and non-radiative decay rate constants, respectively (see figure 1.11). By integrating the equation 1.1.65 with the initial conditions $N(t=0) = N_0$, we obtain:

(1.1.66) $$N(t) = N_0\, e^{-t/\tau}$$

where τ is the excited state lifetime, defined as:

(1.1.67) $$\tau = \frac{1}{\Gamma + k}$$

Therefore, we expect the fluorescence intensity *I(t)*, which is proportional to the excited state population, to decay exponentially. In general, the excited state lifetime of a population of molecules can be calculated as the ensemble-averaged permanence time of the population in the excited state:

(1.1.68) $$\langle t \rangle = \frac{\int_0^\infty t\, N(t)\, dt}{\int_0^\infty N(t)\, dt}$$

If *N(t)* has an exponential decay trend, then:

(1.1.69) $$\langle t \rangle = \frac{\int_0^\infty t\, N_0\, e^{-t/\tau}\, dt}{\int_0^\infty N_0\, e^{-t/\tau}\, dt}$$

and hence:

(1.1.70) $$\langle t \rangle = \tau$$

Thus, for an exponential decay, the average permanence time of a molecule in its excited state is equal to its fluorescence lifetime.

Time-Correlated Single Photon Counting (TCSPC)

There are essentially two methods for calculating the fluorescence lifetime: time domain and frequency domain measurements. The first approach is based on exciting the sample with a pulse of light and measuring the time dependence of the emitted fluorescence; the second one is based on measuring the fluorescence phase shift with respect to a modulated excitation.

Time-correlated single photon counting (TCSPC) is the most common technique used in time domain measurements. In fact, as discusses in the previous paragraph, the fluorescence emission from an ensemble of molecules excited by a laser pulse has an exponential distribution in time. TCSPC can record this distribution by measuring the time delays of individual fluorescence photons with respect to the excitation pulse.

Let us divide the time period between two excitation pulses in a certain number *N* of time channels, each one with amplitude *Δt*. The time-channel *i* corresponds to a mean time delay *t* (measured with respect to the first excitation pulse arrival) and to a certain interval *Δt*. If the average number of photons detected in the i^{th} time channel is $\bar{n}_i$, which in turn corresponds to an average number of detected photoelectrons $\bar{x}_i$, then:

(1.1.71) $$\bar{x}_i = \bar{n}_i \, q$$

where *q* is the detector quantum efficiency. If there is a large number of excitation pulses for every count registered in the i^{th} channel, then the probability $P_x(i)$ of generating $\bar{x}_i$ photoelectrons in the same time channel is given by the following Poisson distribution:

(1.1.72) $$P_x(i) = \frac{(\bar{x}_i)^x \, e^{-\bar{x}_i}}{x!}$$

with:

(1.1.73) $$\sum_{x=0}^{\infty} P_x(i) = 1$$

Therefore, the probability of detecting at least one photoelectron per excitation pulse is given by:

(1.1.74) $$P_{x\geq 1}(i) = 1 - P_0(i) = 1 - e^{-\bar{x}_i} = 1 - \left(1 - \bar{x}_i + \frac{\bar{x}_i^2}{2} + \ldots\right)$$

At very low light levels $\bar{x}_i \gg \bar{x}_i^2/2$ and, hence, the equation 1.1.74 becomes:

(1.1.75) $$P_{x\geq 1}(i) \approx \bar{x}_i = \bar{n}_i \, q$$

Thus, under such conditions, the probability of detecting one or more photon per excitation pulse in the i^{th} time channel is proportional to the fluorescence intensity at a delay time *t*. This is the general required condition for accurate TCSPC measurements.

Assuming that the repetition rate of the source is R_s, and the total rate of detected fluorescence photons over all delay times is R_d, if the condition:

(1.1.76) $$\frac{R_d}{R_s} \equiv \alpha \ll 1$$

is respected, then the probability of detecting two fluorescence photons per excitation pulse is negligible. A value $\alpha \leq 0.01$ is typically required for TCSPC. Let us now consider a *δ*-

function excitation, as we can approximate the pulse of a femtosecond laser. After measuring for a time *T*, the number of counts (i.e. the number of detected fluorescence photons) Y_i acquired in the i^{th} time channel is given, for a single exponential decay of the fluorescence intensity with lifetime τ, by:

(1.1.77) $$Y_i = \alpha R_s T \frac{\Delta t}{\tau} e^{-i\,\Delta t/\tau}$$

The equation 1.1.77 demonstrates another advantage of the TCSPC technique: the measurement accuracy can be improved by simply increasing the acquisition time *T*.

Time resolution

We assumed the excitation light pulse to be a δ-function in time in order to obtain the equation 1.1.77. Such condition is usually accomplished by using mode-locked lasers with pulses whose FWHM Δt_e is much less than the measured fluorescence lifetime τ. However, the time resolution is determined by the overall impulse response of the detection system (mainly the single photon detector, the timing electronics and the optical components).

If the impulse response of the i^{th} system component has a FWHM Δt_i, then the measured FWHM Δt_m is given by:

(1.1.78) $$\Delta t_m \approx [(\Delta t_e)^2 + \sum_i (\Delta t_i)^2]^{1/2}$$

We can now express the measured fluorescence signal *F(t)* as the convolution product of the measured instrumental response function (IRF) *R(t)* and the theoretical fluorescence response function *I(t)* – i.e. the one we would observe for δ-function excitation.

(1.1.79) $$F(t) = \int_0^t R(t')\, I(t - t')\, dt'$$

The IRF $R(t')$ is, in turn, the convolution product between the impulse response functions of all the system components:

(1.1.80) $$R(t') = S(t') \otimes D(t') \otimes O(t') \otimes E(t')$$

where *S(t)* is the excitation pulse temporal profile; *D*, *O* and *E* are the impulse responses of the detector, the optical and the electronic components, respectively. Thus, we can derive the theoretical fluorescence response *I(t)* by experimentally measuring the functions *R(t)*, *F(t)* and then by deconvolving.

1.2 Theory of Raman spectroscopy

The rotational-vibrational spectrum of a molecule is highly related to its geometry, especially in the so-called fingerprint region (500-1500 cm^{-1} or 6-20 μm). Therefore, knowing the spectrum (in such region) of a substance allows its identification. In order to do that, there are two complementary optical techniques: infrared (IR) absorption spectroscopy, and Raman spectroscopy. The latter measures the molecular rotational-vibrational transitions using visible (380-700 nm) or near-infrared (700-2500 nm) light. The main advantages of this technique are:

- lasers can be used as light sources – whereas IR spectroscopy requires traditional incandescent sources or modern (but more costly/complex) nonlinear ones;
- instrumentation materials are not required to be transparent to IR radiation;
- silicon detectors are suitable;
- the Raman spectrum of water shows no major peaks between 500 and 2500 cm^{-1}, while there is a strong absorption in the IR region. Thus, Raman spectroscopy can analyse samples with high water content (i.e. biological samples).

Depending on the desired application, Raman spectroscopy can be implemented in laser-scanning microscopes (which allow imaging based on spectrum analysis [36]) as well as in fibre optic sensors.

In the following paragraph, we will make a brief digression on the molecular rotational-vibrational levels. Then we will discuss the Raman effect, the theory behind it and its application to the study of biological tissues (as done in my PhD research).

1.2.1 Roto-vibrational energy structure of diatomic molecules

A molecule is a system of two or more atoms held together by chemical bonds. If we neglect the hyperfine and spin-orbit interactions, the Hamiltonian of such system consists in the kinetic energy of nuclei, the kinetic energy of electrons, the attractive potential between nuclei and electrons, the repulsive potential between nuclei and the repulsive potential between electrons [37]:

(1.2.1) $$H = -\sum_{\alpha} \frac{\hbar^2}{2M_\alpha} \nabla^2_{R_\alpha} - \sum_i \frac{\hbar^2}{2m_i} \nabla^2_{r_i} - \sum_{i,\alpha} \frac{Z_\alpha e^2}{4\pi\epsilon_0} \frac{1}{|R_\alpha - r_i|} +$$

$$+ \frac{1}{2} \sum_{\alpha \neq \beta} \frac{Z_\alpha Z_\beta e^2}{4\pi\epsilon_0} \frac{1}{|R_\alpha - R_\beta|} + \frac{1}{2} \sum_{i \neq j} \frac{e^2}{4\pi\epsilon_0} \frac{1}{|r_i - r_j|}$$

where R_α , Z_α and M_α are the position, the atomic number and the mass, respectively, of the α^{th} nucleus, and r_i is the the i^{th} electron position. In order to solve the Schrödinger equation of this Hamiltonian, we can introduce the Born-Oppenheimer approximation [38]: a general approximation based on the mass (hence, speed) difference between nuclei and electrons. In fact, during the time required for nuclei to change their relative position due to vibrations and rotations, each electron (being much less massive and much faster than its bounded nucleus) can occupy multiple times the positions within the so-called molecular orbital. Therefore, while describing the electronic energy structure, we can consider the nuclei to be at rest; on the other hand, we can approximate the nuclear rotational and vibrational motions as independent of the electrons motion, since it occurs on a much faster time scale.

In accordance with the hypothesis of electrons instantaneously adapting to nuclear motion, let us consider the Hamiltonian as the sum of a nuclear part and an electronic one; for the latter, however, nuclear coordinates are parameters (instead of variables). The molecular total wave function is thus given by:

(1.2.2) $$\psi(\boldsymbol{r}, \boldsymbol{R}) = \varphi_n(\boldsymbol{R})\, \psi_e(\boldsymbol{r}, \boldsymbol{R})$$

where φ_n depends only on the nuclear coordinates $\boldsymbol{R}$, while ψ_e describes the electronic states as a function of electronic coordinates $\boldsymbol{r}$ given for a certain fixed nuclear configuration. For a diatomic molecule, the Schrödinger equation of the nuclear wave function is:

(1.2.3) $$\left[-\frac{\hbar^2}{2\mu} \nabla^2_R + \frac{L^2}{2\mu R^2} + V_{Morse}(R) \right] \varphi_n(R) = E_{v,l}\, \varphi_n(R)$$

where R is the distance between the two nuclei; L is the orbital angular momentum; μ is the reduced mass of the two-body system; $E_{v,l}$ is the energy eigenvalue depending on quantum numbers v and l, which describe the vibrational and rotational states of the molecule, respectively. The Morse potential V_{Morse} is an approximation for the molecular potential, defined as:

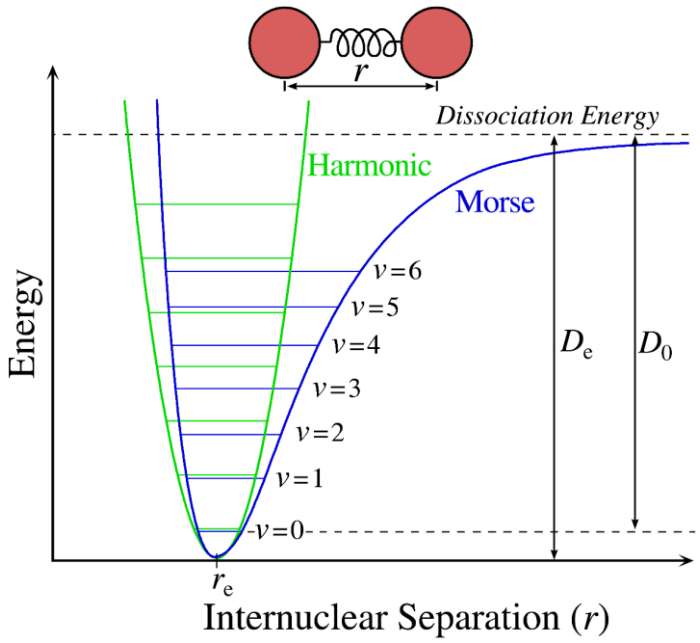

Figure 1.12 Molecular potential of a diatomic molecule: harmonic approximation (green), Morse approximation (blue). Picture taken from [39].

(1.2.4) $$V_{Morse}(R) = D_e \left(1 + e^{-a(R-R_e)}\right)^2$$

where D_e is the depth of the potential well (see figure 1.12), R_e is the equilibrium internuclear distance, and a is a parameter setting the potential curvature. Then, by representing the Morse potential via a Taylor series centred at R_e and stopping at the second order (harmonic approximation), the total energy eigenvalue is equal to:

(1.2.5) $$E_{v,l} = \hbar\omega_0 \left(v + \frac{1}{2}\right) + Bl(l+1)$$

(1.2.6) $$\omega_0 = \sqrt{\frac{k}{\mu}} \; ; \; B = \frac{\hbar^2}{2\mu R_e^2} \; ; \; k = \left(\frac{\partial^2 V_{Morse}}{\partial R^2}\right)_{R=R_e}$$

The selection rules of the obtained roto-vibronic spectrum are: $\Delta v = \pm 1$, $\Delta l = \pm 1$. As shown in the above formulas, the molecular energy levels and the corresponding spacing depend on both the reduce mass and the equilibrium internuclear distance – that is, they are specific for each molecular type. Moreover, since the constant B is inversely proportional to the molecular moment of inertia, the rotational energy contribution is usually very small with respect to the vibrational one. Finally, spectra derived from transitions between these energy levels are in the IR region (i.e. 400-4000 cm^{-1}).

1.2.2 Raman effect

Let us consider a transparent medium, irradiated by monochromatic light whose frequency (v_0) does not match any EM transition of the sample. The incident light mainly passes through the sample, unchanged; nonetheless, a very small part is scattered in different directions by the molecules. By studying the scattered light, we can find that the major part has the same frequency v_0 of the incident field. Such phenomenon is known as Rayleigh (or elastic) scattering, whose intensity is proportional to the fourth power of v_0. However, the scattered light spectrum shows also other frequencies. If v_r is one frequency of the scattered light, then the frequency shift $v_r - v_0 = \Delta v$ can be positive (anti–Stokes Raman shift) or negative (Stokes Raman shift). Δv is also called Raman frequency, or Raman shift. Being independent from the incident frequency v_0, the Raman frequencies reflect the specific molecular energy structure of the scatterer that generated them. Raman lines have higher intensity for negative Δv; moreover, the intensity associated with positive Δv strongly decreases with increasing $|\Delta v|$.

In order to understand this effect, let us consider light as made by photons [40], each one with energy hv_0 (where h is the Planck constant). The collision with a molecule can elastically scatter the photon, leaving its energy unchanged (Rayleigh scattering). Nevertheless, collisions can also be inelastic, causing the molecule to undergo a transition to a higher energy state; as a result, the photon loses energy and is scattered with a lower frequency (negative Δv). On the other hand, if the molecule is already in one excited state, the collision can cause a transition to a lower energy state, and the photon is scattered with higher frequency with respect to v_0 (positive Δv). Therefore, Raman shifts are related to the photon-molecule energy exchanges, which in turn reflect the specific energy transitions undergone by the scattering molecules. Moreover, in thermal equilibrium, the population of energy levels exponentially decreases with increasing energy. Thus, positive Raman shifts are less frequent than negative ones, and their line intensity rapidly decreases with increasing $|\Delta v|$ (figure 1.13).

Raman shifts correspond to the vibrational or rotational transitions of the scattering molecules. While these transitions can be excited through the absorption of IR light, in Raman spectroscopy we can observe them – by means of the corresponding frequency shifts – in the visible spectrum, which is more convenient. Visible light sources and detectors are

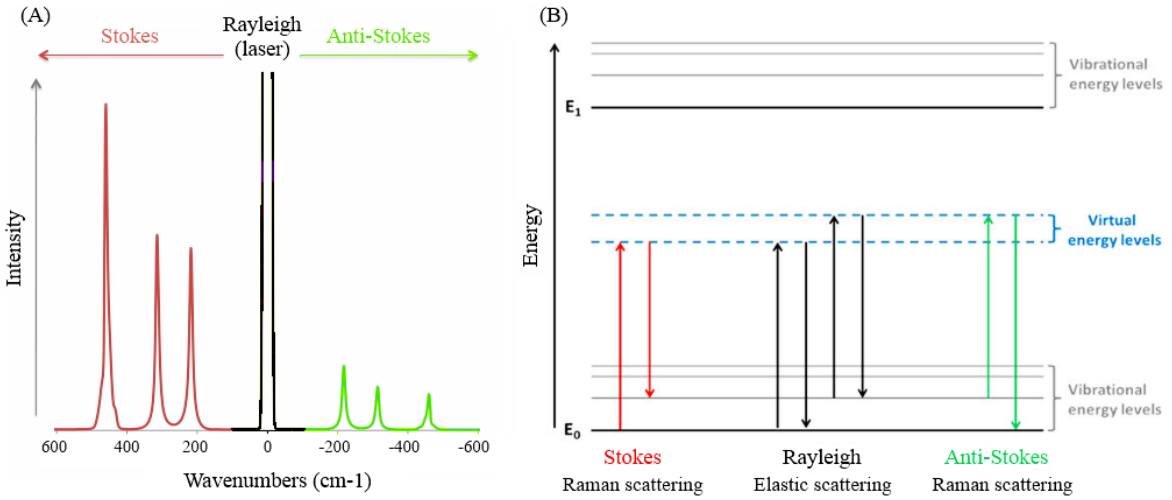

Figure 1.13 A typical spectrum of scattered light (A) and the Jablonski diagram of different scattering processes (B). A): the Rayleigh line (black) is at the centre, while Stokes (red) and anti-Stokes (green) bands are on the left and right sides, respectively [41]. B): Rayleigh scattering transitions (black) are at the centre, while Stokes (red) and anti-Stokes (green) Raman scattering transitions are on the left and right sides, respectively [42].

generally cheaper and/or simpler than the corresponding IR instrumentation; moreover, water absorption is lower in the visible region.

Quantum mechanical theory of light scattering

Georg Placzek developed a theory [43] for explaining the Rayleigh scattering and the Raman effect by studying how the incident light perturbs the wave function of the scattering molecule. In fact, we can define the matrix element of the induced electric dipole moment P_{nm}, corresponding to a transition from the n state to the m state, as follows:

(1.2.7) $$P_{nm} = \int \psi_m^* \, P \, \psi_n \, d\tau$$

where P is the electric dipole moment operator; ψ_m and ψ_n are the wave functions of the n and m states, respectively; the integral is extended over the whole space. The quantum-mechanical result of the integral is:

(1.2.8) $$P_{nm} = \frac{1}{h} \sum_r \left(\frac{M_{nr} \, M_{rm}}{\nu_{rn} - \nu_0} + \frac{M_{nr} \, M_{rm}}{\nu_{rm} + \nu_0} \right) E$$

where r indicates every energy level of the unperturbed molecule; ν_{rn} and ν_{rm} are the frequencies corresponding to the energy gaps between the states indicated by their subscripts; M_{rn} and M_{rm} are the corresponding transition dipole moments; E is the electric

field of the incident light, whose frequency is v_0. The square module of P_{nm} determines the scattering intensity associated with the $n \rightarrow m$ transition:

(1.2.9) $$I_{nm} \propto (\nu_0 + \nu_{nm})^4 |P_{nm}|^2 \propto (\nu_0 + \nu_{nm})^4 I$$

where I is the incident light intensity, which is proportional to E^2. Then, for a system of N_n molecules in the initial state n, we can calculate the total intensity by simply multiplying by the factor N_n. The frequency of the scattered radiation is $v_0 + v_{nm}$. The case $n = m$ (thus $v_{nm} = 0$) corresponds to the Rayleigh scattering. The case $n \neq m$ describes the Raman effect.

Moreover, the expression of P_{nm} contains the transition dipole moments from the initial n state to all the r states of the unperturbed molecule, and those from all the r states to the final m state. However, such transitions do not actually occur during the scattering process. In fact, the r states are also called "intermediate levels" of the scattering process; similarly to the intermediate levels involved in two-photon absorption, their role is purely virtual. The only necessary condition for Raman scattering is that the energy hv_0 of the incident photon has to be greater than the energy gap $E_m - E_n$ between the initial and the final states of the real transition. In fact, since there is no real transition to the r states, v_0 is not required to match any absorption frequency of the scattering molecule. We can also note that the expression of P_{nm} involves the products between the transition dipole moments with the r subscript, and not the single transition dipole moments. Since the latter can be positive as well as negative, terms belonging to different r states may cancel each other and set P_{nm} to zero; in such case, the Raman line is forbidden.

The intensity of a Raman line depends on the frequency v_0 due to both the factor $(v_0 + v_{nm})^4$ and the denominators of the summation shown in the equation 1.2.8. However, for a transparent sample, v_{rn} and v_{rm} are ultraviolet (UV) frequencies; by choosing v_0 in the visible spectral range ($v_0 \ll v_{rn}$, $v_0 \ll v_{rm}$), its contribution to those denominators becomes negligible. Thus, in such conditions, the Raman intensity I_{nm} becomes linearly proportional to the fourth power of the Raman line frequency.

General theory of Raman scattering polarizability

The electric polarization P induced in the scattering molecule by the incident light electric field E can be described as follows:

(1.2.10) $$\vec{P} = \alpha \vec{E}$$

where α is the molecular polarizability. Since P and E are vectors, α is usually a tensor: it is a scalar only when the P and E directions are equal, e.g. for an isotropic molecule. Therefore, the tensor is generally defined by nine components: α_{xx} , α_{xy} etc. Since α is a symmetric matrix, the off-diagonal elements are bound by the following relations:

(1.2.11) $$\alpha_{xy} = \alpha_{yx} \; ; \; \alpha_{yz} = \alpha_{zy} \; ; \; \alpha_{zx} = \alpha_{xz}$$

We can use the six remaining components to form the equation of the ellipsoid associated to α. In fact:

(1.2.12) $$\alpha_{xx}\, x^2 + \alpha_{yy}\, y^2 + \alpha_{zz}\, z^2 + 2\alpha_{xy}\, xy + 2\alpha_{yz}\, yz + 2\alpha_{zx}\, zx = 1$$

Since a symmetric matrix is diagonalizable, the off-diagonal terms can be set to zero by choosing an appropriate coordinate system. Then, the equation 1.2.12 takes the form of an ellipsoid ($A\,x^2 + B\,y^2 + C\,z^2 = 1$).

Moreover, we have to consider the conditions under which the Placzek theory can be applied:

1. The electronic state of the scattering molecule (in practice, its ground state) has to be non-degenerate – which is true in almost all the cases.
2. Raman scattering is mainly due to electrons, which explains why the energy transfer between the incident photon and the molecule depends on its vibrational and rotational motions. In fact, such motions influence the electron cloud polarizability, which interacts with the incident photon. Moreover, if the incident light frequency ν_0 is greater than the nuclear frequencies, electrons can "follow" it, while nuclei cannot (Born-Oppenheimer approximation). Consequently, the polarizability measured for each instantaneous nuclei distribution is almost identical to the case of stationary nuclei in the same positions. Since rotational-vibrational transition frequencies are in the IR spectrum, such condition is satisfied when ν_0 belongs to the visible spectrum.
3. The frequency difference between an electronic absorption band and the incident light has to be big with respect to rotational-vibrational frequencies. In practice, it is easy to satisfy this condition too.

Within such limits, the polarizability α is a function of the nuclear coordinates only. Therefore, if the nuclei follow a classical periodic motion of frequency ν_{mol}, the polarizability

has the same temporal periodicity. When the electric vector of the incident light oscillates with frequency v_0 and polarizes a molecule, the induced electric dipole moment P shows beat frequencies $v_0 \pm v_{mol}$. Thus, the positive sign accounts for anti-Stokes Raman shifts, while the negative sign for Stokes Raman shifts. However, such classical approach cannot explain the intensity difference between Stokes and anti-Stokes shifts. Hence, we need to consider a quantum-mechanical point of view. The matrix element P_{nm} for the $n \rightarrow m$ transition is given by:

(1.2.13) $$P_{nm} = (\int \psi_m^* \, \alpha \, \psi_n \, d\tau) E = \alpha_{nm} \cdot E$$

In the following paragraphs, we will discuss separately vibrational and pure rotational Raman transitions focusing on their intensity and quantum-mechanical selection rules.

Pure rotational Raman effect

For an isotropic molecule, no pure Raman effect is allowed. Classically, if the polarizability ellipsoid is a sphere (as in the case of an isotropic molecule), the incident light "sees" the same polarizability for every angle of rotation of the molecule. Since there is no rotation-induced modulation of α, there are no resulting beat frequencies. Instead, for a linear molecular geometry, the selection rule is $\Delta J = \pm 2$, where J is the total angular momentum. We can explain this result also from a classical point of view. For symmetry reasons, one main axis of the polarizability ellipsoid lies on the inter-nuclear line. If the molecule rotates around an axis perpendicular to such line, the ellipsoid will be in an identical position after half a revolution, and then again after a whole revolution. Therefore, the frequency of its aspect changing is double the rotation frequency, which corresponds to the quantum-mechanical selection rule $\Delta J = \pm 2$.

It is important to stress that pure rotational Raman effect can be observed from molecules without a permanent electric dipole moment, which in fact show no rotational absorption in the IR and the microwave parts of the EM spectrum. Thus, Raman spectroscopy can be used for determining molecular moments of inertia even when absorption techniques are not applicable.

In general, pure rotational Raman frequencies are small: typically between 3 GHz and 3 THz (while vibrational Raman frequencies are in the range of 10-100 THz). In order to measure

them, a high-dispersion, high-resolution spectrograph is needed. Optical frequencies, instead, are in the range of 400-750 THz.

Vibrational Raman effect

Vibrational transitions are generally together with rotational ones, thus the resulting Raman effect shows a roto-vibronic band. Spectroscopic measurements are usually performed on liquid samples, whose rotational energy structure cannot be resolved. However, both classical and quantum-mechanics considerations bring to the conclusion that the total intensity of an unresolved roto-vibronic spectrum is identical to the intensity calculated for averaged (on all the molecular orientations) pure vibrational transitions. Therefore, let us consider only vibrational transition dipole moments as follows:

(1.2.14) $$P_{nm} = \left(\int \psi_m^* \, \alpha \, \psi_n \, dQ \right) E$$

where ψ_m and ψ_n are vibrational wave functions, and α is a function of only the nuclear coordinates Q. When the nuclear configuration of a molecule is slightly distorted in an arbitrary direction, restoring forces come into play; therefore, when released, the molecule performs small-amplitude vibrations. In general, nuclei motion seems random and aperiodic; nonetheless, classical mechanics demonstrates such complex motion to be composed by a finite number of normal modes. For each normal mode, all the nuclei move in phase with the same normal frequency of vibration. We can easily calculate the number of such modes: if there are N nuclei, there are $3N$ degrees of freedom. Molecular translations account for three of them, and rotations for other three. Thus, there are $3N - 6$ degrees of freedom left for the relative positions of the nuclei (e.g. for internal molecular motions). This is the number of normal modes.

In general, at equilibrium, the nuclear configuration of a molecule has some symmetry elements (e.g. planes of reflection, rotational axes, etc). These elements characterise also the symmetry of the electron cloud, which – due to the Coulomb interaction – takes part in the restoring forces after a small change in the nuclei position (i.e. a small molecular deformation). Consequently, the molecular symmetry properties influences the normal modes of vibration. Each mode is described by the corresponding normal coordinates Q, which account for the displacements of all the nuclei.

In the following paragraph, we will use the Placzek simplified theory of polarizability for deriving the intensity and the selection rules of vibrational Raman transitions.

Placzek simplified theory of polarizability

In the general theory about polarizability, we considered the tensor α as a function of the nuclear coordinates. Therefore, for a particular vibration mode, α is a function of the normal coordinates Q. Since the amplitude of these coordinates is small [43], we can represent α via a Taylor series. By stopping at the linear term in Q and neglecting the higher powers, we find:

(1.2.15) $$\alpha = \alpha_0 + \left(\frac{\partial \alpha}{\partial Q}\right)_0 Q$$

where $(\partial\alpha/\partial Q)_0$ represents how much, at equilibrium (subscript zero), α changes with respect to variations in Q. The corresponding matrix element for the $n \rightarrow m$ transition becomes:

(1.2.16) $$\alpha_{nm} = \int \psi_m^* \, \alpha_0 \, \psi_n \, dQ + \left(\frac{\partial \alpha}{\partial Q}\right)_0 \int \psi_m^* \, Q \, \psi_n \, dQ$$

Due to the orthogonality of ψ_m and ψ_n, the first term on the right of the equation is zero, unless $n = m$ (which corresponds to the Rayleigh scattering). If we consider the vibration to be a harmonic oscillation, the second term is zero, unless $m = n \pm 1$ (which corresponds to the ground state Raman band of the vibrational mode). According to this simplified theory, combination bands (i.e. the excitation of more than one normal modes) and overtone bands (i.e. a transition between non-adjacent energy levels) are forbidden: this is the consequence of neglecting the higher terms in the Taylor series. In fact, combination and overtone bands weakly contribute to the total Raman effect; thus, our approximation is well satisfied.

Let us consider the Stokes line of a particular mode, e.g. the $n \rightarrow n + 1$ transition for a non-rotating molecule. By knowing [44] the result of the equation 1.2.16, $\alpha_{n,n+1}$ becomes:

(1.2.17) $$\alpha_{n,n+1} = \left(\frac{\partial \alpha}{\partial Q}\right)_0 \sqrt{\frac{(n+1)h}{8\pi^2 M \nu}}$$

where M and ν are the reduced mass and the ground state frequency of the normal mode. The induced transition moment and the line intensity are given by:

(1.2.18) $$P_{n,n+1} = \alpha_{n,n+1} \cdot E$$

(1.2.19) $$I_{n,n+1} \propto (\nu_0 - \nu)^4 |P_{n,n+1}|^2$$

Thus, the Raman line intensity depends on the derivative tensor $\alpha' = (\partial\alpha / \partial Q)_0$. Two invariant quantities (whose values are not affected by changes in the coordinate system orientation of the molecule) are related to the derivative tensor:

(1.2.20) $$\bar{\alpha}' = \frac{1}{3}(\alpha'_{xx} + \alpha'_{yy} + \alpha'_{zz})$$

(1.2.21) $$\gamma'^2 = \frac{1}{2}[(\alpha'_{xx} - \alpha'_{yy})^2 + (\alpha'_{yy} - \alpha'_{zz})^2 + (\alpha'_{zz} - \alpha'_{xx})^2 + 6(\alpha'^2_{xy} + \alpha'^2_{yz} + \alpha'^2_{zx})]$$

Thus, the intensity of the light scattered by an irradiated molecule is a function of such quantities:

(1.2.22) $$I_{n,n+1} \propto (\nu_0 - \nu)^4 \frac{(n+1)h}{8\pi^2 M\nu} \frac{E^2}{45} [45\bar{\alpha}'^2 + 13\gamma'^2]$$

At room temperature, the majority of scattering molecules is in the lowest vibrational state ($n = 0$). However, some molecules are in the higher states, for which there is a greater intensity (proportional to $n + 1$) of the scattered light. Therefore, considering Boltzmann statistics (regarding the particle distribution on energy levels), the intensity of the Raman line is given by:

(1.2.23) $$(I_{n,n+1})_{oss} = K I_0 \frac{(\nu_0 - \nu)^4}{M\nu(1 - e^{-h\nu/k_B T})} [45\bar{\alpha}'^2 + 13\gamma'^2]$$

where K is a constant and I_0 (which is proportional to E^2) is the incident light intensity. In the following paragraph, we will discuss the applications of the Raman effect to the study of biological samples.

Application of Raman scattering to the study of cells and biological tissues

Being a non-invasive technique, in recent years Raman spectroscopy has been extensively used for analysing biological tissues (e.g. skin, lung, stomach, colon, bladder and arteries [45-49]) as well as for discriminating different cell types and studying cellular biology [50-53]. One of its main advantages consist in detecting small molecular or biochemical changes within cells/tissues in few seconds, thus proving to be a powerful tool for clinical applications [54]. In fact, Raman spectra represent the "fingerprints" of the molecules within the examined sample: detected peaks and their intensities indicate the presence and the

relative abundancy of specific molecules. This technique, for example, can be used to discriminate healthy biological materials from diseased ones.

However, the probability of Raman scattering is extremely low. In particular, for biological tissues, it is several orders of magnitude smaller than the excited fluorescence emission. Therefore, it is necessary

- to minimize the fluorescence contribution with respect to the Raman signal;
- to separate the former from the latter by means of computational techniques [55].

For tissues, fluorescence excited by IR radiation is much lower than fluorescence excited by visible light. Moreover, longer wavelengths allow deeper penetration in the sample. However, Raman intensity is proportional to the fourth power of the excitation frequency, thus visible laser sources provide higher signals than IR laser sources. In general, there is a trade-off between these three factors. Nonetheless, for wavelengths longer than 1000 nm, there is greater absorption by water, which reduces the signal-to-noise ratio (SNR) and the penetration depth. In addition, the detection efficiency of charge-couple devices (CCD) significantly declines above 900-950 nm [56]. Based on such considerations, proper laser sources for Raman spectroscopy of biological tissues emit in the NIR; excitation wavelengths are typically chosen between 780 nm and 830 nm.

For studying a thin layer of living cells, on the contrary, there is no need for reaching high penetration depths. Moreover, cell culture glass-bottom dishes show strong photoluminescence when excited at 785 nm, which completely obscures the fingerprint region of the Raman spectrum [57]. Thus, by taking into account the above-mentioned frequency dependence, a better Raman-to-fluorescence signal can be achieved by using a visible laser source. In addition, when the incident laser frequency is close in energy (resonance) to an electronic transition of the molecule under examination, the vibrational modes associated with the excited electronic state are enhanced [58]. As a result, Raman scattering intensities increase by a factor 10^2-10^6; such effect is known as Resonance Raman (RR [59]). In order to exploit RR, the excitation wavelength has to be in the visible range [60]. Therefore, for all these reasons, a typical wavelength choice for studying cell biology is 532 nm [61-63].

1.3 Conclusions

In this chapter, we discussed the theory of two-photon absorption, second-harmonic emission and Raman spectroscopy, and the basic principles underlying fluorescence lifetime measurements.

Regarding TPEF, we found that, at the second order of the quantum perturbation theory, the two-photon transition probability is proportional to the square of the excitation light intensity. Moreover, the spatial resolution of a two-photon transition is comparable to that one of a confocal microscope, but without the need of a spatial filter. Finally, we described a theoretical approach for calculating radial and axial PSFs for two-photon fluorescence.

Then, we described a generalized theory for SHG emission from a population of emitting molecules. We found that, due to the coherence of the SHG process, the emitted SHG power scales with the square of the molecule number. The angular distribution of the emitted SHG light strongly depends on the spatial distribution of the emitting molecules within the focal volume; in the particular case of one-dimensional distributed molecules, it depends on the angle between the emitting dipoles and the optical axis. SHG typically shows a larger signal contribution in forward direction, thus it is usually forward detected; however, in highly scattering media (as tissues), it can be backward detected by taking advantage of the backscattered forward-emitted SHG photons.

Regarding FLIM measurements in the time domain, we demonstrated that TCSPC is a powerful method for measuring fluorescence decay functions at low fluorescence light level. The accuracy of such technique can be enhanced by increasing the acquisition time, and its time resolution depends only on the response of optical and electronics components.

Finally, we described the rotational-vibrational energy levels of a molecule and discussed the theory of the Raman effect, which is related to the transitions between them. Being an optical, non-invasive technique, Raman scattering has a great potential for studying biological samples and providing tools for clinical applications. In this regard, we also discussed the proper choice of the excitation source for two kinds of samples: tissues and cells. In general, a NIR wavelength is more convenient for studying tissues, while a visible wavelength is better for studying cells.

All these concepts will be recalled and applied in chapter 2, while describing the procedures adopted for characterising and calibrating the experimental setups.

Chapter 2: Materials and methods

2.1 Experimental setups

During my PhD, I designed and developed a custom-made multimodal microscope combining two-photon microscopy and Raman spectroscopy; then I used it in two separate studies (see chapters 3 and 5). A further study (see chapter 4) was conducted by using a commercial Raman microscope (XploRA INV, Horiba, Kyoto, Japan). In this section, I will describe both the experimental setups and report the adopted procedures for their calibration and characterisation.

2.1.1 Custom-made multimodal microscope

I contributed to the realization and the development of an optical, laser-scanning microscope for TPEF, FLIM, SHG and Raman microscopy. Such system allows spectroscopy and 3D imaging of both thin and "bulk" biological samples. It consists in four major parts – laser source, optical scanning system, mechanical components and detection system – placed on an optical table and on a vertical breadboard. A detailed description of the developed experimental setup, together with drawings and pictures, is provided below.

Laser source, optical scanning and detection systems

The excitation source is a Ti:Sapphire laser (Mira900F, Coherent, Santa Clara, CA, USA) either emitting 140 fs pulses at a 76 MHz repetition rate or a continuous wave beam. Its wavelength is tuneable – by means of a micrometre that controls the rotation of a birefringent wave plate – between 700 nm and 980 nm. Its pump is a frequency-doubled Nd:YAG laser (Verdi V10, Coherent, Santa Clara, CA, USA) emitting at 532 nm. As shown in figure 2.1A, the output beam passes through a collimating telescope (lenses L1 and L2, f = 50 mm, placed in a 4f configuration). An electronic shutter S (SH05, Thorlabs, Newton, NJ, USA) regulates the laser illumination time of the sample. The beam power is adjusted by a polarization-based system, consisting of a half-wave plate $\lambda/2$ and a polarizing beam splitter (PBS). A motorized device (NSR1, Newport, Irvine, CA, USA) rotates the plate, which in turn rotates the polarization of the electric field, causing only a part of it to be transmitted by the PBS. Then, a quarter-wave plate $\lambda/4$ changes the excitation field polarization from linear to circular (at the sample) and compensates for the polarization ellipticity introduced by other

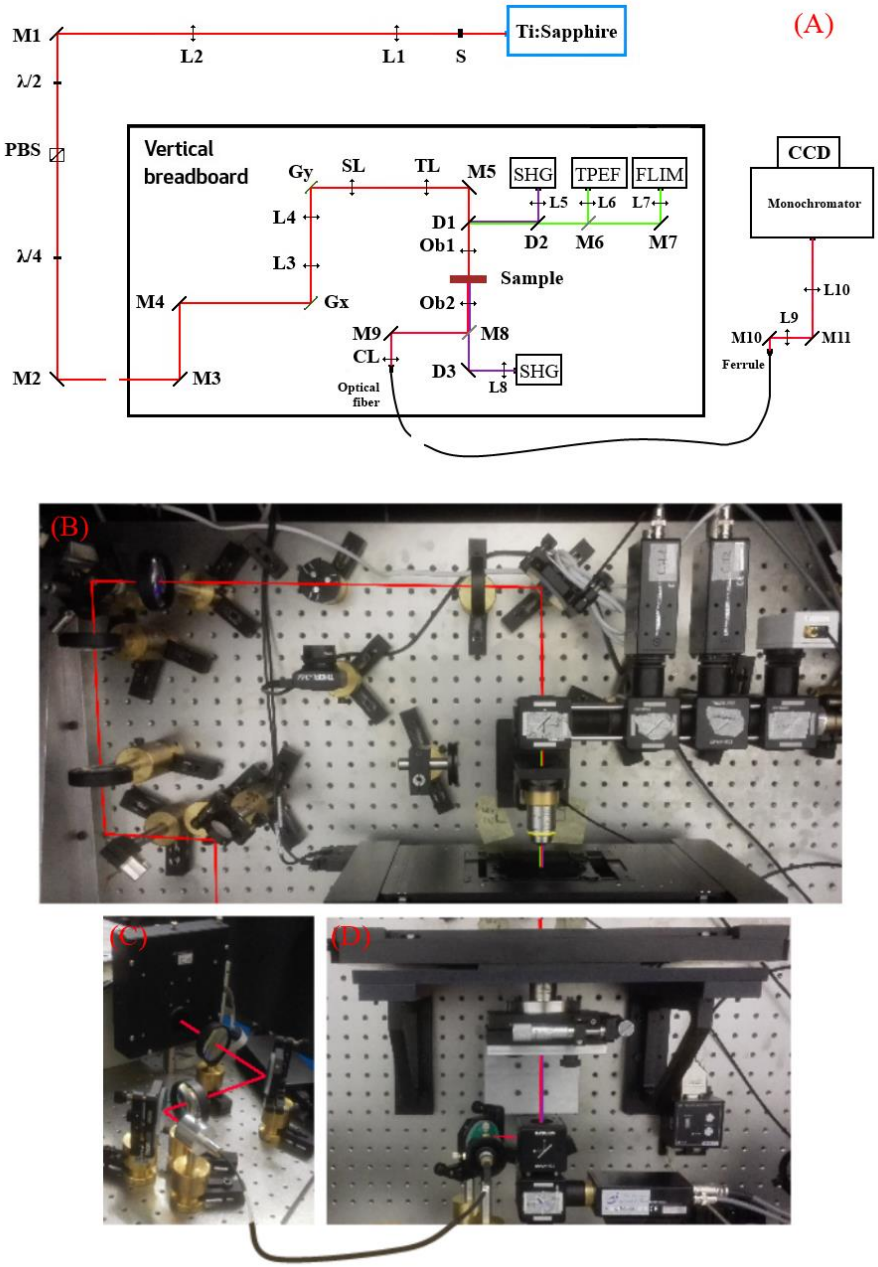

Figure 2.1 Experimental setup of the custom-made multimodal microscope. A): optical scheme. B) and D): pictures of the upper and lower parts of the vertical breadboard, respectively. C): picture of the custom-made F# matcher placed in front of the monochromator.

optical elements. The transmitted beam goes to a scanning system mounted on a vertical breadboard, based on two galvanometric mirrors – Gx and Gy (VM500, GSI Lumonics, Karlsruhe, Germany) – and an optical relaying telescope between them (L3 and L4 lenses, f = 60 mm, 4f configuration). In particular, the choice L3 and L4 lenses was done by considering that longer focal lengths make the beam alignment easier, but also require bigger

lens diameter and longer optical path (i.e. more space on the vertical breadboard). On the other hand, shorter focal lengths make the alignment more difficult, while requiring smaller lenses and allowing a more compact optical scheme. In this case, an adequate solution consisted in two lenses with 50.8 mm diameter and 60 mm focal length. Other two lenses (the scanning lens SL, with 50 mm focal length, and the tube lens TL, with 200 mm focal length) expand the beam to about 1.5 cm diameter in order to overfill the back-aperture of the objective, and reduce the scanning angle by a factor of 4. Then, the laser beam travels through a dichroic mirror D1 (FF685-Di02, Semrock, Rochester, NY, USA) before being focused on the sample by the objective Ob1. Two piezoelectric motors – P725.4CL and M-687 (Physik Instrumente, Karlsruhe, Germany) – ensure high-precision controlled movement of the objective along the optical axis (Z) and of the sample across a radial plane (XY), respectively. There is also a manual linear stage (M-126.M0, Physik Instrumente, Karlsruhe, Germany) for a grossly axial (Z) positioning of the objective.

The light emitted from the sample is detected either forward and/or backward. Fluorescence and second-harmonic light are backward-collected by the same objective used for excitation and reflected by the D1 dichroic mirror, which has a 665 nm cut-off wavelength. The epi-detection system consists of three photomultiplier (PMT) tubes: two detectors H7422 (Hamamatsu, Hamamatsu City, Japan) and one high-speed PMT for photon counting PMH-100 (Becker-Hickl, Berlin, Germany). As shown in figure 1A, each detector is fixed to 30 mm "cage" cube (DFM1/M, Thorlabs, Newton, NJ, USA) that allows quick mounting/replacing of optical filters and dichroic mirrors in prealigned configurations. In order to focus the optical signal at the entrance of each PMT, a lens with a very short focal length (30 mm) is placed inside each connecting tube between the detector and the corresponding cube. In fact, considering that the detection is performed in non-descanning mode (the "confocal" point is scanned in the image plane), this lens allows maintaining the "confocal" point always within the sensible area of the detector. For example, combining this lens with a 20× objective having 200 mm reference focal length produces a 3× magnification: thus, laser scanning a 500 μm size area on the sample results in a 1.5 mm size scanned area on the image plan. Of course, a shorter focal length would further reduce the size of the scanned area on the detector aperture, but such advantage typically comes together with a smaller lens diameter – which in turn reduces the light collected by the lens itself. Since the sensible area of each detector has ~1 cm diameter, there is no need for smaller

magnification; moreover, the diameter of L5, L6 and L7 lenses perfectly fits the connecting tube size, maximising light collection. Finally, the three cubes are fixed together through a set of steel rods. All these arrangements were chosen for providing a very compact mechanical structure for SHG, TPEF and FLIM detection. In fact, second-harmonic light is reflected by the dichroic mirror D2 (FF452-Di01, Semrock, Rochester, NY, USA), passes through a narrow band-pass filter and is detected by the first H7422 detector. Fluorescence passes through both the 452 nm dichroic and a large band-pass filter; then is reflected by a removable mirror M6 (DFM1/M-E02, Thorlabs, Newton, NJ, USA) and detected by the second H7422 photomultiplier. Alternatively, fluorescence signal can be detected using the PMH-100, and then processed by a single photon counting FLIM board SPC-730 (Becker-Hickl, Berlin, Germany) for time-resolved analysis.

Forward-emitted SHG is collected by the objective Ob2, whose position is adjusted by two manual translation stages: M-126.M0 and AKT-120 (Physik Instrumente, Karlsruhe, Germany) for Z and XY positioning, respectively. SHG is reflected by the dichroic mirror D3 (FF685-Di02, Semrock, Rochester, NY, USA), filtered by another narrow band-pass filter and focused by another lens L8 (with 30 mm focal length) into the sensible area of a third H7422. Instead, forward-emitted Raman signal is reflected by a removable mirror (DFM/M-P01, Thorlabs, Newton, NJ, USA) placed after the objective Ob2, and then focused by the collector lens CL into the tip of an optical fibre bundle. At the distal end of the fibre bundle, light comes out from 24 fibres arranged in two lines within an MTP connector. The latter is connected to a ferrule, which in turn arranges the fibres in one vertical line at the entrance of a custom-made F# matcher. The latter consists of two mirrors (M10-11) and two lenses (L9-10, with 75 mm and 150 mm focal lengths, respectively) placed in 4f configuration with respect to the ferrule output. I designed these scheme for increasing the beam F# from the optical fibre bundle by a factor of 2; thus, the typical F# of silica fibres (~2) is matched with the input of the subsequent monochromator (F# ~4). As result, the F# matcher projects the image of the 24 fibres onto the monochromator slit while reducing both stray light and losses in collection efficiency. Finally, Raman signal enters the monochromator (Oriel Cornerstone 260, Newport, Irvine, CA, USA), where it is diffracted by a 1200 lines/mm grating and detected by a CCD camera (Andor DU401A, Andor Technology, Belfast, Northern Ireland, UK). In order to reduce thermal noise, the CCD is cooled to -80 °C by an external liquid cooler and a Peltier cell. Since Raman measurements

are performed with 785 nm wavelength excitation, there are three additional optical filters in the setup. First, a narrow band-pass filter (FF01-780/12, Semrock, Rochester, NY, USA), placed before the dichroic D1, for "cleaning" the excitation wavelength from any spurious contribution; second, a long-pass filter (LPD01-785 RU, Semrock, Rochester, NY, USA), placed after the objective Ob2, for preventing the excitation beam from entering the optical fibre bundle; finally, a notch filter (NF03-785E, Semrock, Rochester, NY, USA), placed in the optical fibre bundle tip.

Mechanical components

The experimental setup is placed onto two metallic breadboards – a horizontal one (1800 mm × 1200 mm) and a vertical one (1200 mm × 750 mm) – with M6 threaded grids, whose spacing is 25 mm. Two set-square-shaped supports fix the vertical breadboard to the horizontal one, which in turn stands on a granite optical table, sustained by four reinforced concrete legs. A neoprene substrate – 1 cm thickness – placed between the horizontal breadboard and the table dampens mechanical vibrations.

As already mentioned, the P725.4CL and M-687 piezoelectric motors move (respectively) the objective and the sample with submicron accuracy. The objective is grossly positioned by the M-126.M0 manual stage. In order to place these components according to the vertical architecture of the microscope, I designed some proper mechanical components: a shelf for the M-687 motor, and a holder for the P725.4CL and M-126.M0 stages (figure 2.2A and B, respectively). In order to do so, I used a Computer-Aided Design (CAD) software, 3D Autodesk Inventor [64]. Thereafter, all the components were made of aluminium alloy by the mechanical workshop of the Italian National Institute of Optics (INO).

The shelf consists of a rectangular ring (length: 360 mm; width: 237 mm; height: 15 mm), two "big" set-square-shaped supports (length: 258 mm; width: 50 mm; height: 170 mm; thickness: 15 mm) and two "small" ones (length. 185 mm; width: 15 mm; height: 135 mm; thickness: 15 mm). Four screws fix the M-687 motor to its shelf. For holding the objective, two mechanical pieces are needed: a plate (width: 50 mm; height: 70 mm; thickness: 10 mm) for fixing the M-126.M0 stage to the vertical breadboard, and a T-shaped mount (length: 130

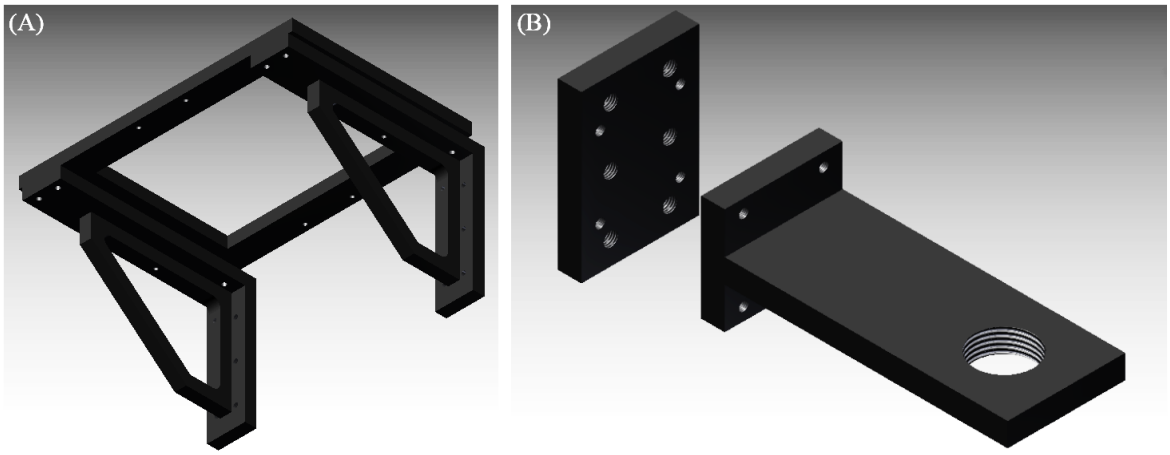

Figure 2.2 3D drawings of the shelf (A) and the holder (B), which support the XY and Z motorized and manual stages, respectively.

mm; width: 50 mm; height: 45 mm; thickness: 10 mm) – fixed to the manual stage itself – which holds the P725.4CL motor and the objective.

Calibration and characterisation

Several experimental measurements and protocols were implemented for characterising spatial and temporal resolution of the microscope, as well as for calibrating some of its components. I will report them in the following paragraphs.

Calibration of the scanning system

As already mentioned, the scanning system is based on two galvanometric mirrors: one moves the excitation beam along the X-axis, the other along the Y-axis. The inputs received by the mirrors are voltage signals: a greater amplitude produces a larger angle of rotation (with respect to the equilibrium position of the mirror). Thus, images are acquired by point-by-point (i.e. pixel-by-pixel) detection of the signal collected during the scanning, and their field of view (FOV) depends on the maximum voltage applied to each galvanometric mirror. In order to determine the FOV dimensions – i.e. to calibrate the mirrors response in function of the applied voltage – I moved a fluorescent object (by using the XY motorized stage) while imaging it. A calibration factor was calculated by measuring how much the image of the object was displaced as a function of its physical changes of position (as reported from the position sensor of the XY stage).

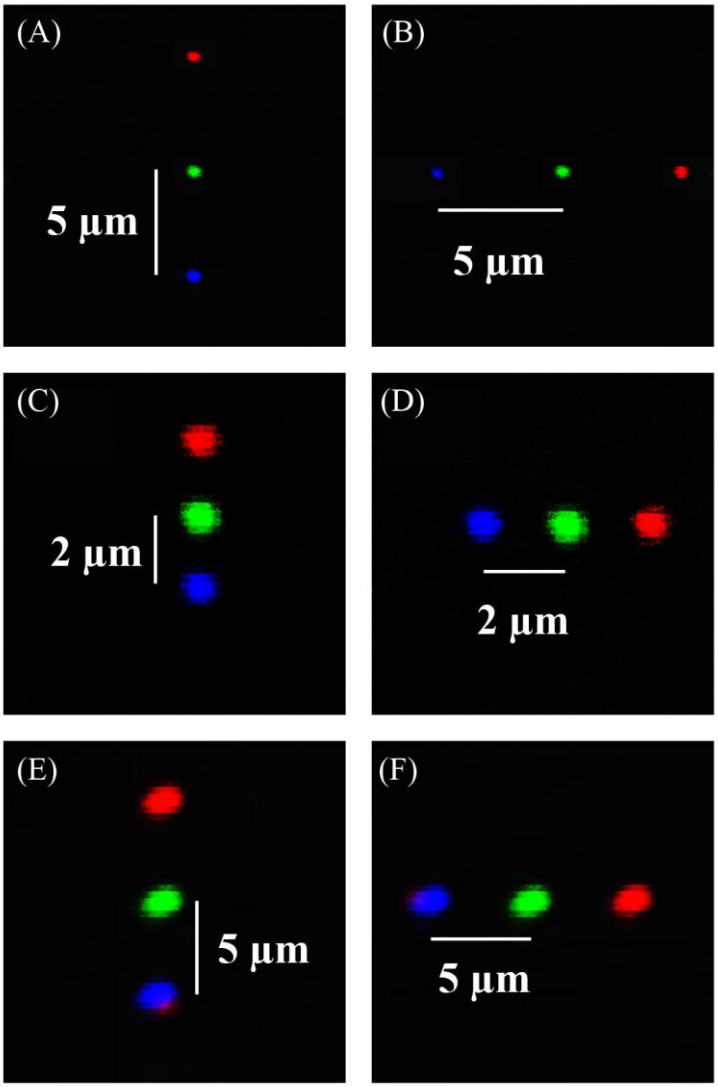

Figure 2.3 QDs TPEF images acquired at three equally spaced positions (marked progressively in red, green and blue) of the XY motorized stage. A) and B): three images of a QD, acquired with a 40× objective at 5 µm steps. C) and D): three images of a QD, acquired with a 20× objective at 2 µm steps. E) and F): three images of a QD, acquired with a 10× objective at 5 µm steps.

For this procedure, I chose to image a quantum dot (QD) with 50 nm diameter. Therefore, I placed a water (n = 1.33) solution containing QDs on a microscope slide. The QDs sticked to the glass surface, and a proper concentration was set in order to have few of them per FOV. Then I moved the slide via the XY stage at small (2-5 µm) steps, while looking at the corresponding QD displacements (measured in terms of pixels) within the observed FOV, as shown in figure 2.3. By calculating the calibration factor between image displacements and physical ones, FOV dimensions were simply derived. Consequently, I obtained a voltage-to-FOV calibration.

Since the FOV depends on the magnification of the excitation objective, I did such procedure for three objectives: Plan-Apochromat 10× (Carl Zeiss, Oberkochen, Germany; NA = 0.45, WD = 2 mm), Plan-Apochromat 20× (Nikon, Shinjuku, Tokyio, Japan; NA = 0.75, WD = 1 mm) and Plan-Apochromat 40× (Carl Zeiss; NA = 0.95, WD = 0.25 mm).

Spatial resolution

In two-photon microscopy, the size of the excitation beam focus determine the spatial resolution (as discussed in section 1.1.1). Since the QDs used in the previous section are much smaller than the spatial resolution of the microscope, they can be used also for measuring the PSF. Thus, I did the 3D TPEF imaging of a QD for two wavelength/objective sets: 740 nm excitation and 20× objective (NA = 0.75); 840 nm excitation and 40× objective (NA = 0.95). After setting the FOV dimensions (9 μm for the first set, 15 μm for the second one) and choosing the number of pixels (512 × 512 for each image), a Z-scan of the QD was done by moving the objective at 0.2 μm steps. I used the software ImageJ [65] for measuring both the radial intensity profile of the QD fluorescence emission and, for each step of the Z-scan, the total number of emitted photons. Finally, by plotting the latter as a function of the Z-position, I obtained the axial intensity profile of the QD fluorescence emission.

The results are shown in figure 2.4. The radial and axial intensity profiles represent, respectively, the radial and axial point spread functions (PSFs) of the two-photon microscope. The data points of each profile are fitted to a Gaussian function, whose FWHM represents the spatial resolution. At 740 nm, with NA = 0.75, the obtained FWHM of the radial and axial PSFs are (630 ± 20) nm and (4.3 ± 0.2) μm, respectively. At 840 nm, with NA = 0.95, the obtained FWHM of the radial and axial PSFs are (410 ± 30) nm and (3.3 ± 0.2) μm, respectively. The uncertainty of each result is given by the nominal spatial resolution: for radial results, by the size of each image pixel; for axial results, by the size of each Z-scan step.

By doing the calculation described in section 1.1.1, we can compare these finding with those derived from the theory of two-photon microscopy. At 740 nm, with NA = 0.75 and n = 1.33, the FWHM of the theoretical radial and axial PSFs are 400 nm and 2.2 μm, respectively. At 840 nm, with NA = 0.95 and n = 1.33, the FWHM of the theoretical radial and axial PSFs are 360 nm and 1.6 μm, respectively. Thus, the presented results are in line with those predicted by the theory: when comparing the two wavelength/objective sets, the

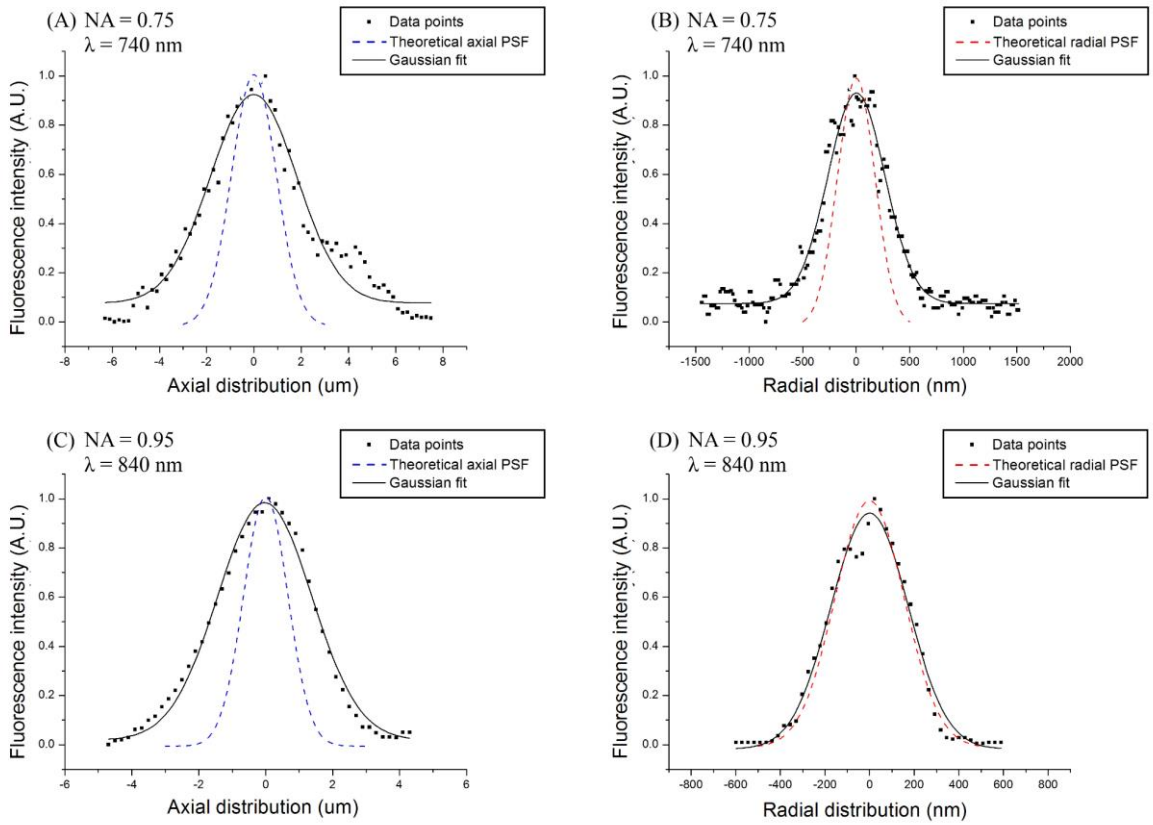

Figure 2.4 Axial (left) and radial (right) PSFs measured from TPEF emission from a water solution containing QDs (50 nm diameter). A) and B) graphs show the results obtained with 740 nm excitation and NA = 0.75. C) and D) graphs show the results obtained with 840 nm excitation and NA = 0.95. Each graph shows the collected data points (black squares), the corresponding Gaussian fit (black solid line) and the theoretical PSF (dashed line; blue for axial PSFs, red for radial ones).

objective with higher NA results in better spatial resolution – despite being used with a longer excitation wavelength.

Temporal resolution

The temporal resolution of a time-correlated single photon counting (TCSPC) system is given by the instrumental response function (IRF). The latter – as discussed in section 1.1.3 – is the convolution product between the impulse response functions of all the system components. In order to measure the IRF of FLIM detection, we can approximate it as the system temporal response to a very short (in time) signal: for example, SHG emission. In fact – as discussed in section 1.1.2 – harmonic generation involves coherent radiative scattering, which is an instantaneous process. Moreover, since the expected temporal resolution (hundreds of picoseconds) is about 1000 times bigger than the temporal FWHM

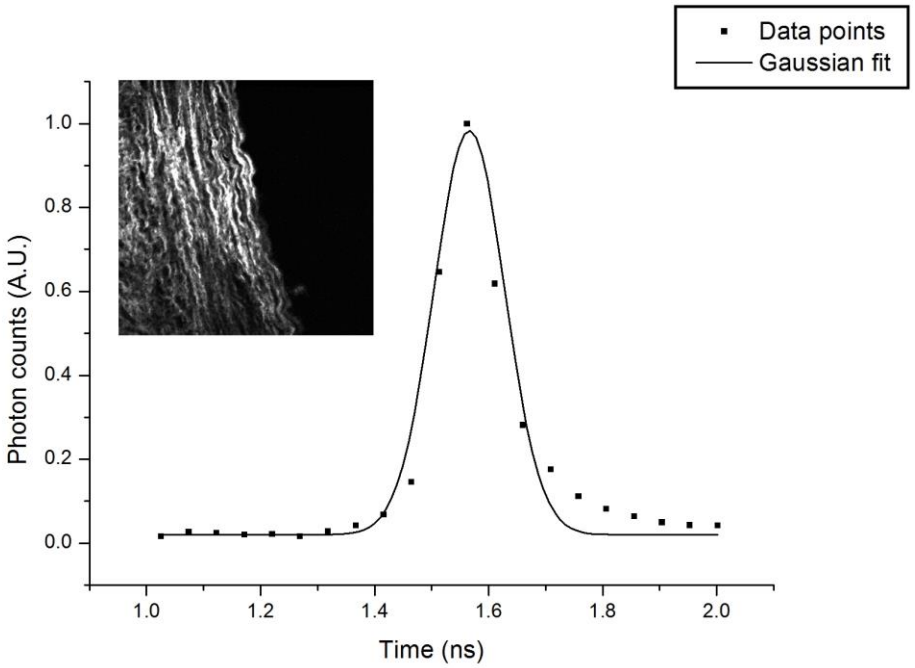

Figure 2.5 IRF of the FLIM detection system. The data points (black squares) represent the time-resolved SHG signal intensity emitted by collagen. A Gaussian function (black line) fits the data. The top-left picture shows a bundle of collagen fibres imaged through SHG microscopy.

of a laser pulse (140 fs), the latter can be considered a δ-function in time. Thus, by exciting second-harmonic emitters with a laser pulse, the temporal FWHM of the resulting SHG signal can be approximated as the effective IRS of the detection system.

For this measurement, I set the laser wavelength to 840 nm and then used the FLIM detection system for imaging a sample of collagen (which emit a strong SHG signal). In order to detect only the second-harmonic emission, I placed a narrow band-pass filter (FF01-420/10, Semrock, Rochester, NY, USA) before the PMH-100 detector. Finally, the time-resolved signal emitted from collagen was plotted (see figure 2.5) and fitted to a Gaussian function. Its FWHM is (150 ± 50) ps – where the uncertainty is given by the nominal temporal resolution of the measurement (12500 ps / 256 time channels). Such result is consistent with the IRF of the FLIM detector, whose data sheet certifies it is 150 ps.

Half-wave plate calibration

As already mentioned, the laser power can be adjusted by rotating a half-wave plate (λ/2) placed before a PBS. In order to calibrate this polarization-based system, I measured – with

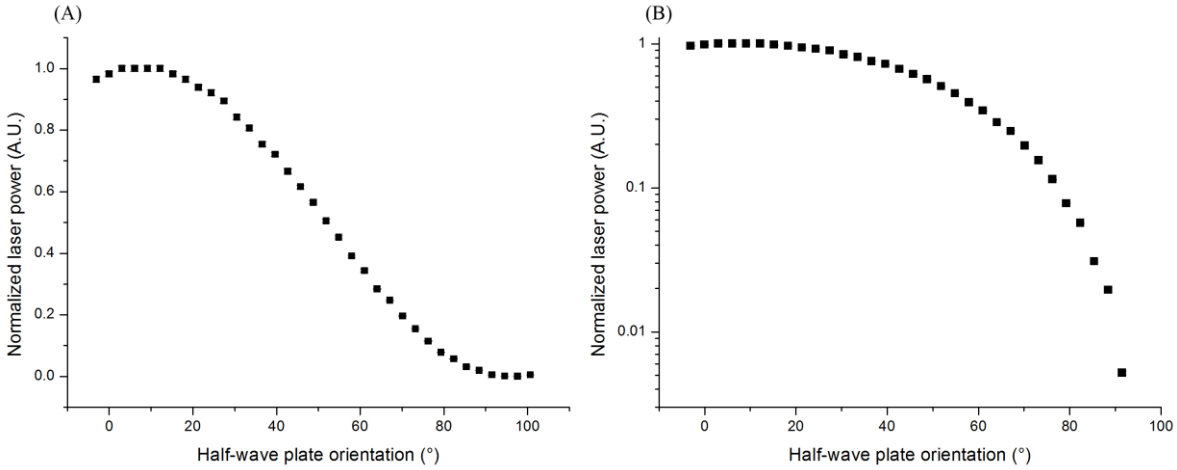

Figure 2.6 Calibration curve of the laser power as a function of the half-wave plate rotation, plotted both on linear (A) and logarithmic (B) scales. The laser power, reported on the vertical axis, is normalized to the maximum measured value; error bars are smaller than the plotted data points (black dots). The plate orientation, reported on the horizontal axis, is expressed in degree.

an optical power meter (S120C, Thorlabs, Newton, NJ, USA) – the laser power passing through the PBS for different orientations of the half-wave plate.

The results are shown in figure 2.6. The laser power has a sinusoidal behaviour (2.6A) in function of the plate orientation, as expected from rotating the polarization of the incident electric field. Moreover, this system allows a decrease in beam intensity of three orders of magnitude (2.6B).

Measurement of TPEF intensity dependence from laser power

As discussed in section 1.1.1, the two-photon transition probability is proportional to the square of the excitation intensity. In order to verify that I am measuring optical signals excited by a two-photon process, I measured the TPEF emission of an autofluorescent plastic slide (92001, Chroma Technology, Bellows Falls, VT, USA) for different values of the laser power – i.e. for different orientations of the half-wave plate, as explained in the previous paragraph. The fluorescence emission intensity was detected though a PMT (as described at the beginning of this section).

Figure 2.7 shows the fluorescence intensity collected at different laser powers. The quadratic trend expected from the theory is a very good approximation of the experimental data: the latter are fitted to a power function, whose exponent is found to be (1.99 ± 0.07).

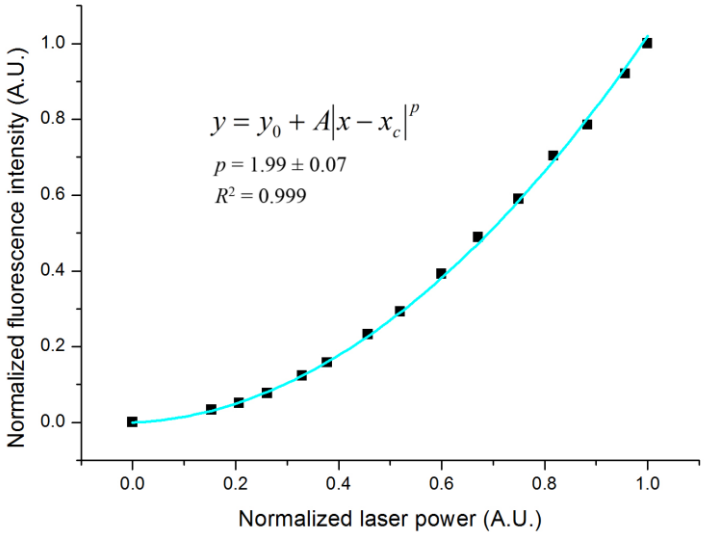

Figure 2.7 TPEF intensity as a function of the laser power. The acquired data (black squares) are fitted with a power function (cyan line). The exponent resulting from the fit is equal to (1.99 ± 0.07); such value is consistent with the quadratic trend expected from the theory (section 1.1.1).

Measurement of flat-field deviation

Ideally, each point of the observed FOV should receive the same amount of laser power; thus, laser-scanning a uniform sample should produce an equally uniform output image (i.e. a flat-field image). However, imaging larger FOVs requires greater scanning angles, which in turn may cause losses of laser power due to the limited size of the objective aperture. In fact, before being focused onto the sample, the excitation beam is partially cut by the edges of the objective. As result, image edges are darker than its centre and the maximum FOV size is limited by this effect. Thus, in order to estimate the deviation of the microscope scanning system from perfect flat-field illumination, I recorded the TPEF emission of an autofluorescent plastic slide (the same one used in the previous paragraph) while imaging a 500 × 500 μm^2 FOV with a 10× objective.

Figure 2.8 shows the average fluorescence intensity profile of the recorded image. The recorded intensity is approximately constant (within 10% from the maximum value) in a 330-μm-size area, and decreases ~20% at the edges of the image with respect to the centre. Moreover, the intensity losses at the edges are approximately linear: 1% loss every 8 μm. Based on these results, flat-field correction was not considered necessary for applying the

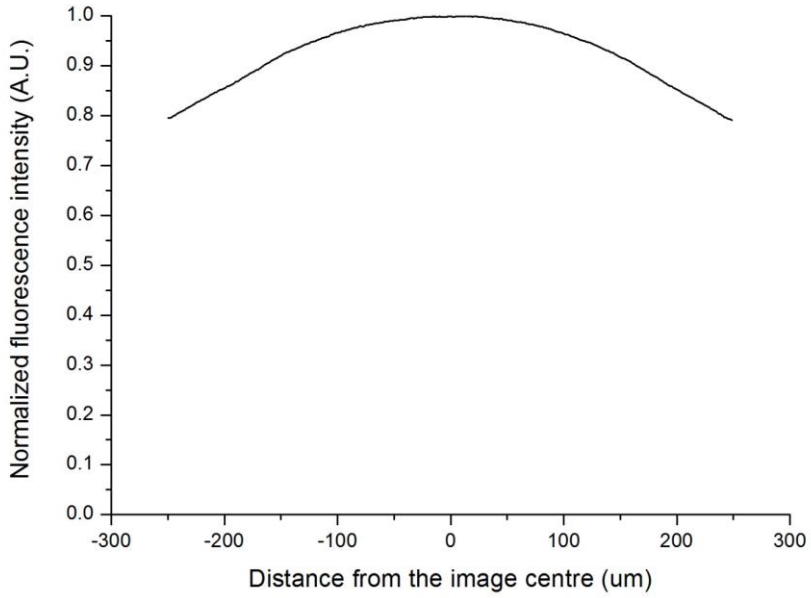

Figure 2.8 Fluorescence intensity profile of a TPEF image (500 × 500 μm^2 FOV) acquired with a 10× objective from a uniform autofluorescent plastic slide. The intensity profiles recorded on the major axes of the image were averaged and normalized to the maximum intensity value.

image analysis techniques described in the following section 2.2.1. In particular, the study reported in chapter 3 is based on the analysis of images recorded from the uniform-illumination-area of the same objective used for this measurement.

Single photon counting regime

TCSPC consists in measuring the arrival time of single photons of a weak light signal with respect to a pulsed excitation with high-repetition frequency. In proper conditions, the probability to detect one photon during one period of the signal is very low. Moreover, as discussed in section 1.1.3, the probability of detecting two or more photons per excitation pulse is negligible. Consequently, the fluorescence decay curve can be reconstructed by detecting single photons, measuring their temporal delay with respect to the excitation pulse, and making a statistics on the arrival time of individual photons.

Therefore, this technique can be successfully adopted when the signal intensity lays within a proper range. On one hand, above a certain intensity level, the probability of detecting two photons per single excitation pulse increases and cannot be neglected anymore. Since the

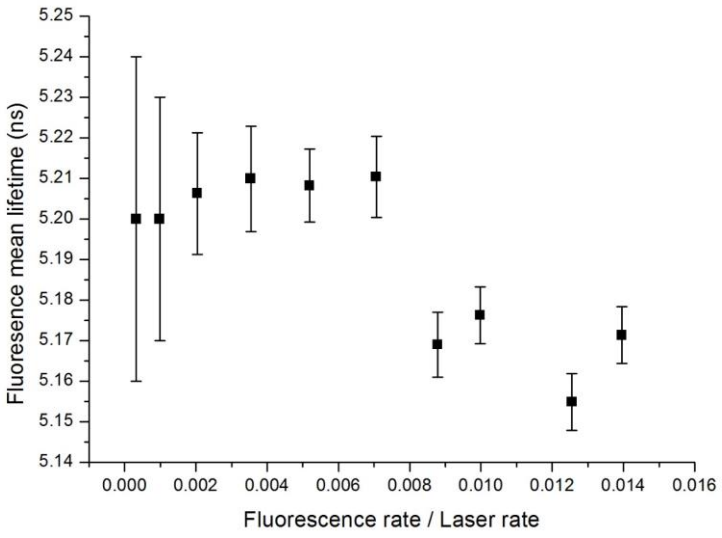

Figure 2.9 Fluorescence lifetime calibration. The horizontal axis reports the ratio between the number of detected fluorescence photons per second (fluorescence rate) and the number of laser pulses per second (laser rate). The vertical axis reports the corresponding values of the measured mean fluorescence lifetime.

TCSPC electronics can detect only one photon per pulse because of dead time, the second photon is missed, causing the measured fluorescence lifetime to be underestimated (i.e. lower than the actual one). On the other hand, when fluorescence intensity decreases, the SNR decreases too. Under a certain intensity level, noise affects so much the fluorescence decay curve that the measurement is no more reliable.

In order to estimate the proper signal range for the collected intensity, I measured the lifetime of an autofluorescent plastic slide (the same one used in the two previous paragraphs), excited using different values of the laser power – and, therefore, of the fluorescence intensity. The slide contains a chromophore (fluorescein isothiocyanate, FITC) whose fluorescence decay can be approximated with a single exponential function. In this regard, an alternative calibration sample could have been a water solution of FITC, but its preparation requires high precision pH control and reproducibility. Thus, the plastic slide was preferred for providing reproducible measurements, and for being ready-to-use and compatible with the mechanical mounting on the XY stage.

The collected intensity can be expressed in terms of the ratio between the fluorescence rate and the laser rate (as done in figure 2.9). The former is the number of detected fluorescence

photons per second, while the latter is the number of laser pulses per second; the TCSPC electronics measures both of them. Thus, I measured the fluorescence mean lifetime (τ_m) at different fluorescence-rate-to-laser-rate ratios. The procedure adopted for FLIM analysis will be described in details in section 2.2.1.

The results are shown in figure 2.9. Fluorescence lifetime of FITC is known in literature, but only for water solutions; thus, we cannot compare the measured value and the tabulated one. We know from the theory of TCSPC that the fluorescence-rate-to-laser-rate ratio has to be much lower than 1. In practice, TCSPC typically works when such ratio is below 0.01. In fact, I verify that the measured fluorescence lifetime is underestimated when the ratio is greater than 0.008. On the other hand, when the ratio is smaller than 0.002, noise decreases the measurement precision, resulting in larger uncertainty (error bars). In the range between these two values, I found the fluorescence lifetime of the slide to be constant and equal to (5.209 ± 0.015) ns. Therefore, I always verified the fluorescence-rate-to-laser-rate ratio to be within such range of values when taking FLIM measurements on biological samples.

Spectrograph calibration

Raman signal is forward collected and sent to a monochromator, where it is diffracted by a 1200 lines/mm grating and detected by a CCD camera. The diffracted light is detected by the pixels of the camera according to the Bragg's law:

$$n\,\lambda = d\,[\sin\theta_0 + \sin\theta] \tag{2.1.1}$$

where n is a positive integer (the diffraction order); λ is the diffracted wavelength; d is the spacing between the lines on the grating; θ_0 is the angle of the incident light with respect to the normal of the grating; θ is the angle of the diffracted light with respect to the normal. The grating can be rotated in order to change the angle θ_0 and select the desired spectral range. In general, for small values of θ, the relation between wavelengths and angles can be approximated as linear ($sin(\theta) \approx \theta$) over the observed spectral range.

The CCD consists in a rectangular array of 1024 × 256 pixels; in particular, the diffraction angles are distributed across the longer side of the detector. Hence, I did a spectral calibration for assigning the corresponding wavelength to each one of the 1024 pixels. In order to do that, I recorded the emission spectrum of a Neon-Argon glow lamp (figure 2.10A). Its emis-

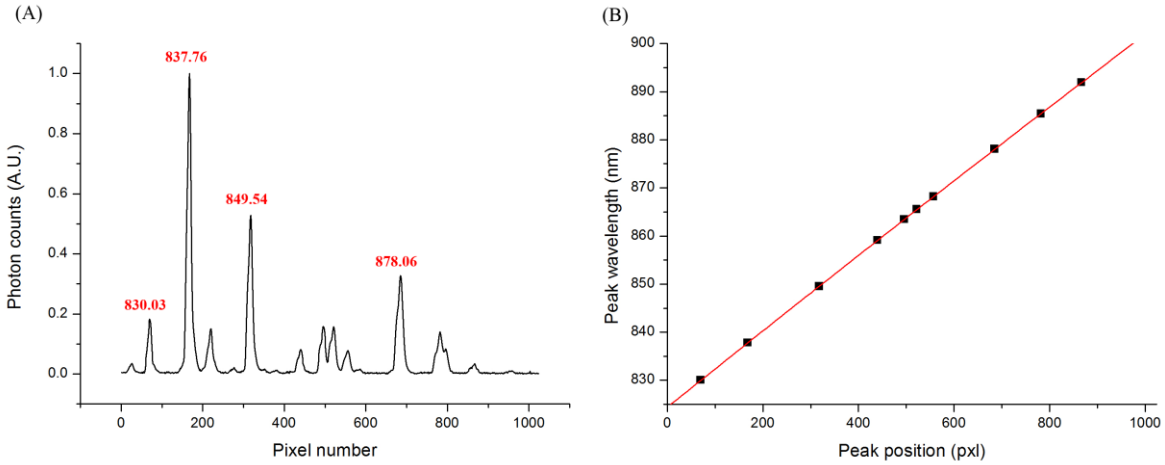

Figure 2.10 A): emission spectrum of a Neon-Argon glow lamp, acquired with the Raman detection setup of the custom-made microscope. The horizontal axis reports the CCD pixels, while the vertical axis reports the corresponding number of collected photons. The wavelength of each emission peak is annotated in red and expressed in nm. B): the graph reports the wavelength of each emission peak as a function of its corresponding position (pixel) on the camera. The data (black squares) are fitted with a sinusoidal function (red line), which is approximately linear – as expected by the Bragg's law for small angles.

sion lines are narrow and well-known in literature [66], thus I was able to assign the corresponding wavelength to each recorded peak. Then, I plotted the emission wavelengths as a function of the corresponding pixels and – according to the Bragg's law – I used a sinusoidal fitting (figure 2.10B). As expected, the fitting function is approximately linear in the small angle range. Such procedure allowed calibrating the wavelength of the recorded signals for each camera pixel.

Excitation laser wavelength calibration

As discussed in section 1.2.2, Raman shifts (i.e. the frequency difference between excitation frequency and scattered ones) correspond to vibrational or rotational transitions of a scattering molecule. Hence, they are independent from the excitation wavelength/frequency. Therefore, in order to compare Raman spectra acquired with different excitation wavelengths, Raman shifts are usually reported in wavenumbers (measured in cm^{-1}) instead of wavelengths (measured in nm). In fact, the relation between a Raman shift (*RS*) and its corresponding wavelength is:

(2.1.2) $$RS(cm^{-1}) = \left(\frac{1}{\lambda_{ex}(nm)} - \frac{1}{\lambda(nm)}\right) 10^7$$

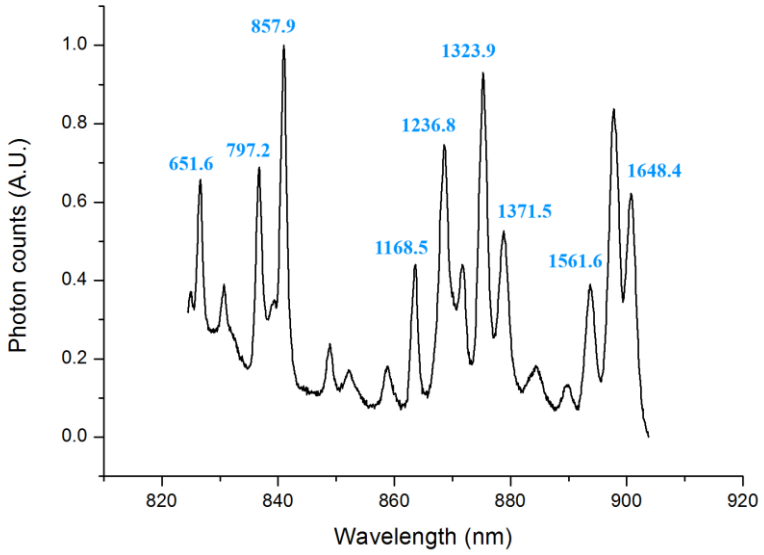

Figure 2.11 Raman spectrum of paracetamol. The horizontal axis reports the detected wavelengths, while the vertical axis reports the corresponding (normalized) number of collected photons. The Raman shift of each peak is annotated in blue and expressed in cm^{-1}.

where λ_{ex} is the excitation wavelength, and λ is the scattered wavelength, both expressed in nm units. Different excitation wavelengths produces different scattered wavelengths, but same wavenumbers.

In order to calculate the Raman shift corresponding to a scattered wavelength, it is necessary to know the excitation source wavelength. The latter is typically calibrated using well-known Raman shifts of a calibration substance, e.g. paracetamol. In fact, equation 2.1.2 can be rewritten as:

(2.1.3) $$\tilde{\nu}_{ex} = \tilde{\nu} + RS$$

where $\tilde{\nu}_{ex} = 10^7/\lambda_{ex}(nm)$ is the absolute wavenumber (in cm^{-1} units) corresponding to the excitation wavelength, and $\tilde{\nu} = 10^7/\lambda(nm)$ is the absolute wavenumber corresponding to the scattered wavelength. Therefore, peak positions in the measured spectrum are converted from wavelength to absolute wavenumbers, and the reference values for the corresponding Raman shift are added. This yields the absolute wavenumber of the excitation laser, which in turn can be reconverted to wavelength. Thus, such procedure provides an estimate of the excitation wavelength.

Peak wavelength (nm)	Absolute wavenumber (cm^{-1})	Raman shift (cm^{-1})	Excitation absolute wavenumber (cm^{-1})	Excitation wavelength (nm)
826.62	12097	652	12749	784.38
830.68	12038	711	12749	784.38
836.71	11952	797	12749	784.38
840.98	11891	858	12749	784.38
848.92	11780	969	12748	784.44
858.93	11642	1106	12748	784.44
863.67	11579	1169	12747	784.50
868.55	11513	1237	12750	784.31
871.71	11472	1279	12750	784.31
875.25	11425	1324	12749	784.38
879.09	11375	1372	12747	784.50
893.73	11189	1562	12751	784.25
900.75	11102	1648	12750	784.31

Table 2.1 Columns from left to right: wavelengths of the detected Raman peaks, their absolute wavenumbers, the corresponding Raman shifts (known from literature), the absolute wavenumber of the excitation source (obtained by summing the latter two columns), and its wavelength.

Therefore, I set the laser wavelength to 785 nm through its micrometre, and then I acquired the Raman spectrum of paracetamol powder (figure 2.11) placed on a quartz slide. Raman shifts of paracetamol are well-known in literature [67], thus I was able to assign them to the corresponding recorded peaks. Table 2.1 reports the calculations for calibrating the excitation wavelength, and the latter was found to be (784.38 ± 0.13) nm. Such value is consistent with the accuracy (~1 nm) of the micrometre that allows setting the laser wavelength.

2.1.2 Commercial Raman microscope

The commercial microscope used for Raman measurements is an XploRA INV (Horiba, Kyoto, Japan) is an inverted, confocal Raman microscope. This commercial setup consists of three lasers with different wavelengths (532, 638 and 785 nm) and powers (20-25 mW for the firsts two, 180-200 mW for the third one), an optical system for delivering the excitation

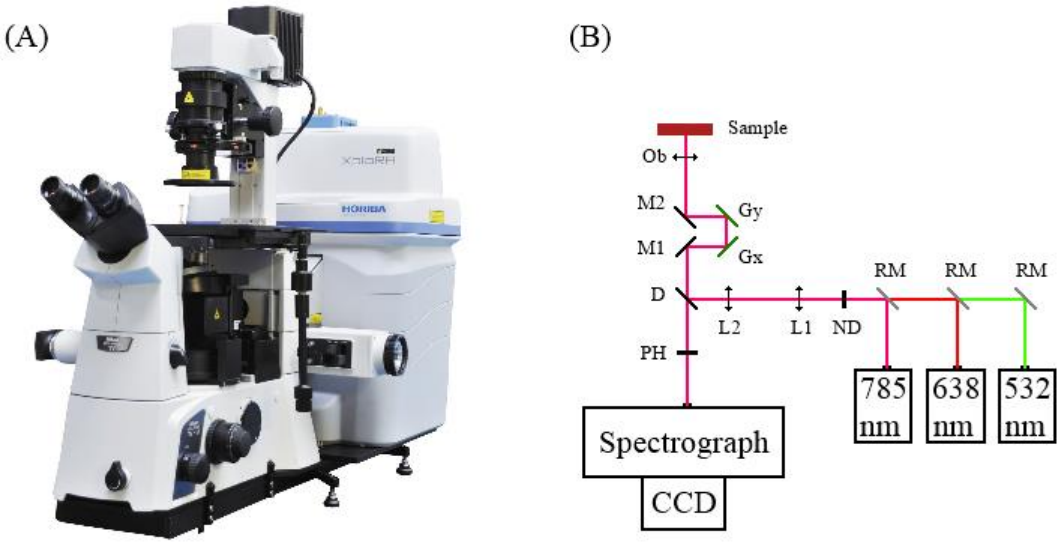

Figure 2.12 Picture of the XploRA INV microscope (A) and its representative optical scheme (B).

light on the sample (figure 2.12) and a spectrograph. The microscope is remotely controlled via PC software (LabSpec6, Horiba, Kyoto, Japan).

Raman measurements are performed in epi-detection configuration. The inverted configuration of the system is particularly suited for studying cell cultures. In addition, two white-light sources allow for wide field epi- and trans- illumination imaging, respectively.

Description of the Raman system

A removable mirror (RM) selects the excitation source. The laser power can be adjusted by rotating a variable neutral-density filter (ND) between six discrete positions, corresponding to 0.1%, 1%, 10%, 25%, 50% and 100% of the maximum power. A dichroic mirror (D) reflects the laser toward the excitation objective (Ob). Before the latter, there is a scanning system based on two galvanometric mirrors (Gx and Gy), allowing for Raman signal acquisition by either a single point or from an arbitrary scanned area within the sample. The acquired signal is backward-collected, passes through the dichroic and a pinhole (PH), and finally enters the spectrograph. The pinhole diameter can be adjusted between three sizes (100, 300 and 500 µm) for alternatively increasing the spatial resolution or the collected signal. Moreover, there is a slit at the entrance of the spectrograph: its width can be adjusted among three sizes (100, 200 and 300 µm) for increasing/decreasing the spectral resolution.

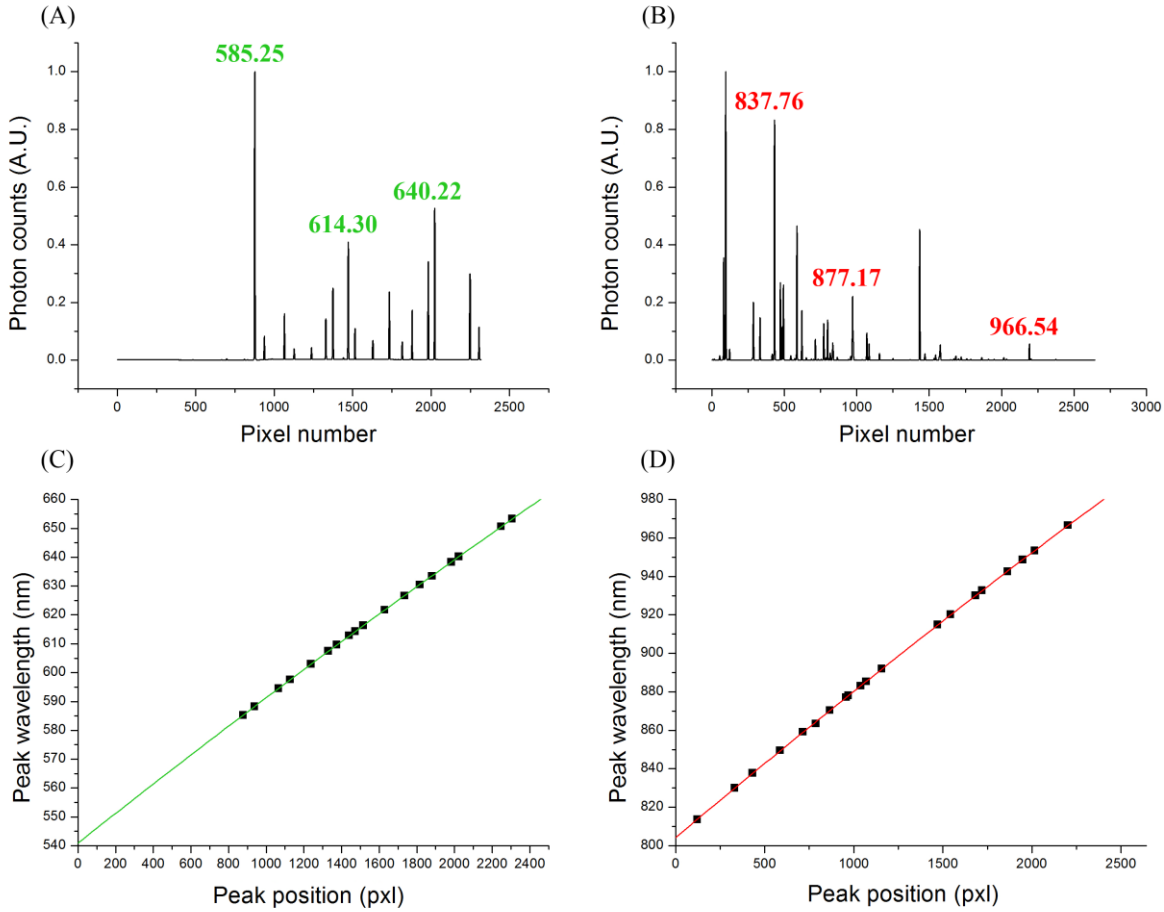

Figure 2.13 A) and B): emission spectra of a Neon-Argon glow lamp, acquired in two distinct spectral ranges (541-654 and 804-996 nm, respectively) with the Xplora INV microscope. The horizontal axis reports the CCD pixels, while the vertical axis reports the corresponding normalized number of collected photons. The wavelength of each emission peak is annotated in green (A) or red (B) and expressed in nm. C) and D): each graph reports the wavelength of the emission peaks as a function of their corresponding positions (pixels) on the camera. The data (black squares) are fitted with a sinusoidal function (green or red, respectively) which is approximately linear – as expected by the Bragg's law for small diffraction angles.

Inside the spectrograph, light is diffracted by a grating and detected by a CCD camera. The spectrograph has four gratings with different spacing (600, 1200, 1800 and 2400 lines/mm).

Calibration

In order to calibrate this experimental setup, I did the same procedures previously described for calibrating the Raman detection system of the custom-made microscope. I will report them in the following paragraphs.

Spectrograph calibration

I recorded the emission spectrum of a Neon-Argon glow lamp in two spectral ranges: 541-654 nm (corresponding to 313-3506 cm^{-1} for 532 nm excitation) and 804-996 nm (corresponding to 301-2699 cm^{-1} for 785 nm excitation). I assigned the corresponding wavelengths to the recorded peaks, I plotted them as a function of the corresponding pixels and I used a sinusoidal fitting. Figure 2.13 shows the results.

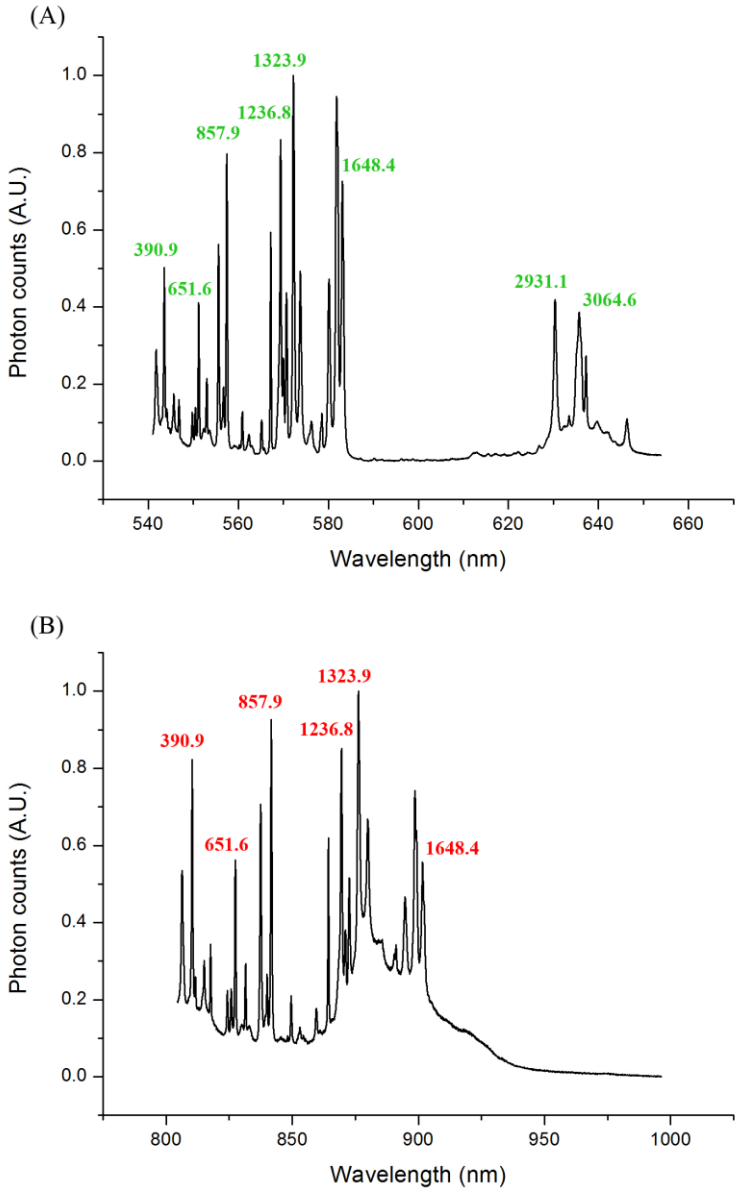

Figure 2.14 A) and B): Raman spectra of paracetamol acquired with 532 and 785 nm excitation, respectively. The horizontal axis reports the detected wavelengths, while the vertical axis reports the corresponding normalized number of collected photons. The Raman shift of each peak is annotated in green (for 532 nm excitation) or red (for 785 nm excitation) and expressed in cm^{-1}.

Excitation laser wavelength calibration

I acquired the Raman spectrum of paracetamol powder, placed on a glass coverslip, with two laser wavelengths: 532 and 785 nm (figure 2.14A and B). I assigned to the main emission peaks their corresponding Raman shifts (known from literature). Then, for both measurements, I used the same procedure previously described for determining the excitation wavelength. The results are: (532.0 ± 0.2) nm, (785.1 ± 0.3) nm. Thus, such findings are consistent with the specifications provided by the XploRA producer.

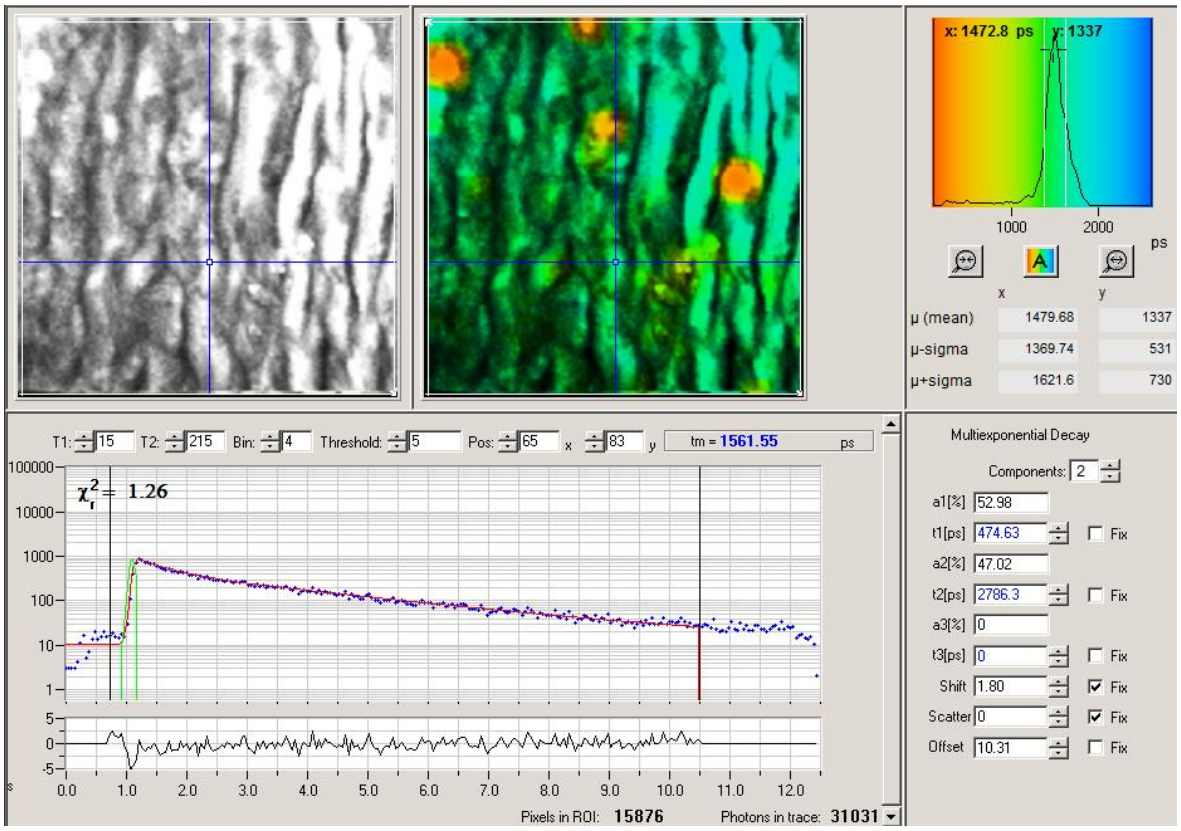

Figure 2.15 Graphical user interface of the FLIM data analysis software (SPCImage). Top-left: greyscale TPEF intensity image. Top-centre: false colour image showing the fluorescence mean lifetime τ_m (red colour corresponds to 100 ps, blue colour to 2600 ps). Top-right: τ_m histogram. Bottom-centre: time-resolved fluorescence signal (blue dots) recorded on the pixel indicated by the cross-shaped cursor. The software calculates the instrumental response function (green line), performs a deconvolution between the latter and the acquired signal, and finally performs a biexponential fitting (red line) of the data points. These data were obtain through FLIM acquisition on a human carotid cross-section.

2.2 Methods for data analysis

In this section, I will describe different data analysis methods applied to multiphoton images and to Raman spectra. Then, after reporting the samples used during my PhD and their preparation (section 2.3), I will explain how such methods were applied to analyse the acquired data (section 2.4).

2.2.1 Analysis of multiphoton images

Extraction of fluorescence mean lifetime

For analysing the mean fluorescence lifetime, I used the software SPCImage 4.9.7 (Becker-Hickl, Berlin, Germany). As shown in figure 2.15, this software shows the time-resolved fluorescence signal collected for each pixel of the FLIM image. The software automatically evaluates the IRF and performs a deconvolution between the latter and the time-resolved detected signal (see section 1.1.3). Finally, an exponential decay function fits the deconvoluted data points. More in detail, a biexponential fitting allows separating two decay components: a fast one (i.e. with shorter mean lifetime) and a slow one (i.e. with a longer mean lifetime). Thus, for each image pixel, time-resolved fluorescence intensity can be approximated according to the following equation:

(2.2.1) $$\frac{I(t)}{I_0} = a_1\, e^{-t/\tau_1} + a_2\, e^{-t/\tau_2}$$

where I_0 is the fluorescence intensity collected over all the temporal channels, τ_1 is the fast component, τ_2 is the slow component, a_1 and a_2 are their respective coefficients (whose ratio a_1/a_2 reflects the relative abundance of the fast component over the slow one). Therefore, the fluorescence mean lifetime τ_m calculated at a given pixel is given by:

(2.2.2) $$\tau_m = \frac{a_1\,\tau_1 + a_2\,\tau_2}{a_1 + a_2}$$

SPCImage calculates all these parameters (τ_1, τ_2, τ_m, a_1 and a_2) for each image pixel. Moreover, it generates a histogram for each parameter, reporting the distribution of its values within the image: the horizontal axis reports the parameter values (grouped in class intervals, whose width can be freely chosen) and the vertical axis reports the number of pixels where such values were recorded. For example, a peak at 1500 ps (with 10 ps interval width) in the distribution of τ_m indicates that the mean fluorescence lifetime of most molecules in the im-

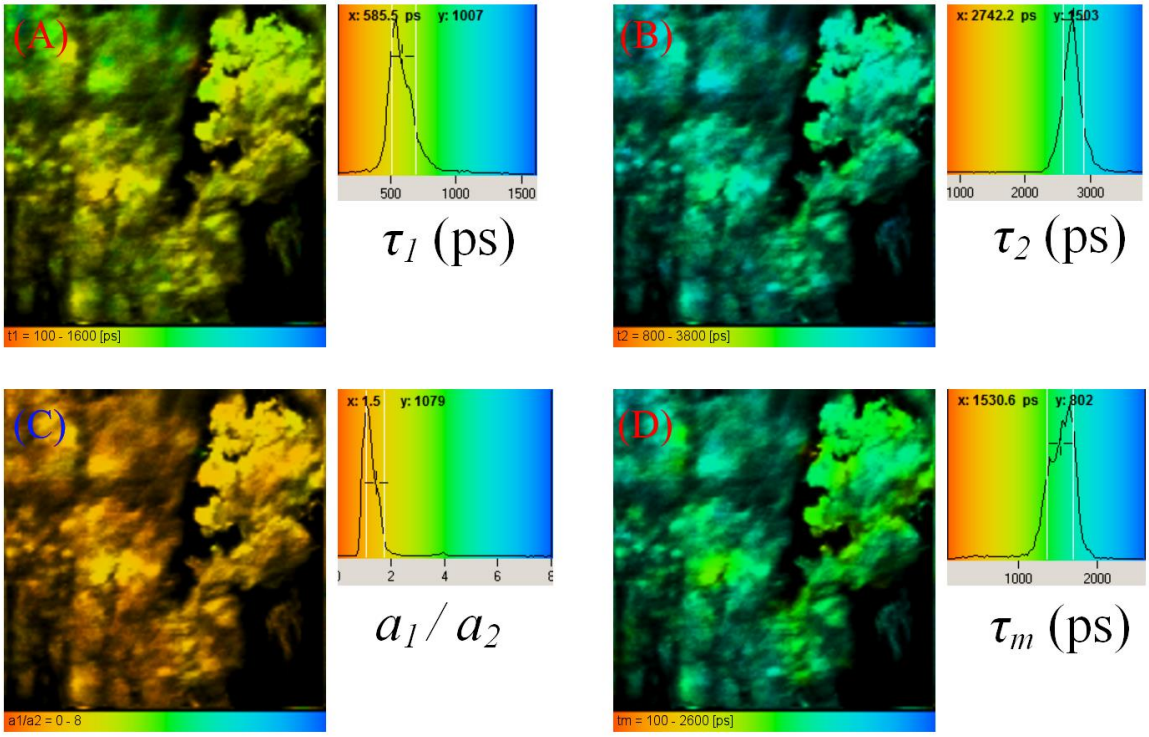

Figure 2.16 False colour FLIM images. A-D): τ_1, τ_2, a_1/a_2, τ_m images and distribution histograms, respectively. The colour range of each parameter is listed as follows: for τ_1, 100-1600 ps; for τ_2, 800-3800 ps; for a_1/a_2, 0-8; for τ_m, 100-2600 ps. Each histogram has 100 class intervals. These data were obtain through FLIM acquisition on a human carotid cross-section.

aged area is comprised between 1495 ps and 1505 ps. The software generates also a false colour image for each parameter, where every colour corresponds to a different value of the parameter itself; moreover, the higher the fluorescence intensity, the brighter the image.

In conclusion, each FLIM image provides four distributions – τ_1, τ_2, τ_m, a_1/a_2 (figure 2.16) – and the corresponding false colour images.

Analysis of SHG images through Fast Fourier Transform (FFT)

The Fast Fourier Transform (FFT [68]) is an algorithm for calculating the Discrete Fourier Transform (DFT) and its inverse function. DFT transforms a function from time (or space) domain to frequency (or spatial frequency) domain, and vice versa.

FFT can be applied to image analysis: in fact, the distribution of image spatial frequencies can be used for characterising the geometry of the observed structures. This technique is particularly useful for monitoring the organization of collagen fibres observed in SHG im-

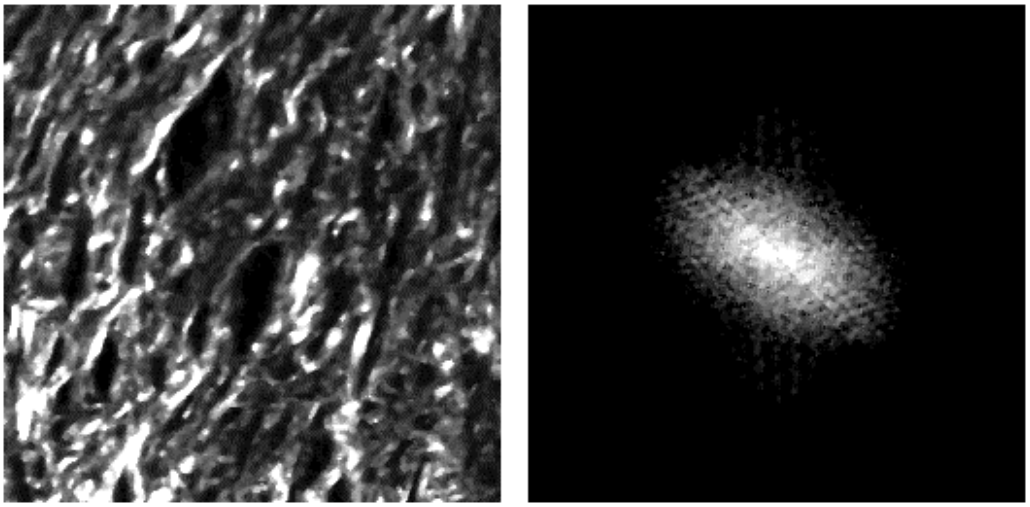

Figure 2.17 SHG image (left) showing collagen fibres, and its FFT profile (right). As expected, the major axis of the FFT ellipsis is orthogonal to the main direction of collagen fibres: the former is bottom-right to top-left oriented, while the latter are bottom-left to top-right aligned.

ages [69]. For example, a bundle of aligned fibres results in a FFT image showing high intensity values along a direction orthogonal to the direction of fibres themselves. In such case, the FFT intensity profile is elliptic (figure 2.17). On the contrary, if collagen fibres are randomly oriented, the FFT image shows a circular intensity profile.

Therefore, acquiring a SHG image and determining the eccentricity of its FFT intensity profile allows characterising the anisotropy of collagen fibres within the examined tissue. The anisotropy level is given by the minor-to-major axis ratio ("aspect ratio") of the elliptic FFT profile. If the sample is perfectly isotropic, the FFT aspect ratio is equal to 1; if the sample is totally anisotropic, the ratio is 0.

Analysis of TPEF images through Grey Level Co-occurrence Matrix (GLCM)

The co-occurrence matrix is a simple and well-known tool for analysing monochromatic images (as the one shown in figure 2.17), providing information on the spatial relations between their pixel intensity values. In fact, the Grey Level Co-occurrence Matrix (GLCM) compares the grey level of a pixel with the one of its neighbours at a certain distance (offset).

In order to describe such procedure, let us consider a practical example, as the one reported in figure 2.18. Panels A) and B) show a greyscale image with four grey levels (0, 1, 2 and 3) and its corresponding numerical matrix, respectively. As shown in panel C), we can generate

(A) 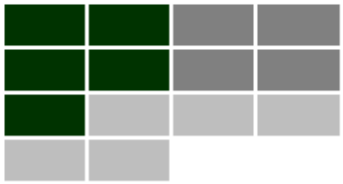

(B)

0	0	1	1
0	0	1	1
0	2	2	2
2	2	3	3

(C)

neig. pxl value --> ref. pxl value:	0	1	2	3
0	0,0	0,1	0,2	0,3
1	1,0	1,1	1,2	1,3
2	2,0	2,1	2,2	2,3
3	3,0	3,1	3,2	3,3

(D)

2	2	1	0
0	2	0	0
0	0	3	1
0	0	0	1

Figure 2.18 The figure [70] shows the procedure for calculating the GLCM elements. A): greyscale image with four grey levels: 0, 1, 2 and 3. B): numerical matrix corresponding to the image. C): structure of GLCM (4 × 4 matrix) calculated for offset = 1 pxl. This example investigates the following relation: "reference pixel on the left, pixel to be compared on the right" (or "right-to-left"). D): GLCM of the top image, for offset = 1 pxl and for "right-to-left" pixel relation.

a new square matrix, whose dimension (4 × 4) is given by the number of grey levels in the original image. Known as GLCM, such matrix investigates the relation between grey levels of different pixels in the original image; each pair of examined pixels is at a fixed offset from one another. In this example, the offset is 1 pxl and the relation is: "reference pixel on the left, pixel to be compared on the right" (or "right-to-left"). Therefore, cell (0,0) reports the number of times a pixel with intensity 0 is immediately on the right of a pixel with intensity 0. Cell (0,1) reports the number of times a pixel with intensity 1 is immediately on the right of a pixel with intensity 0. Etc. Panel D) shows all the GLCM elements obtained from this procedure. Then, in order to consider all the possible directions, a GLCM routine usually calculates other three matrices (left-to-right, bottom-to-top, top-to-bottom) for the same offset. Finally, the four matrices are averaged.

Statistical methods based on GLCM detect the repetition of a certain pattern within the original image. One of them is c*orrelation* (*Cor*), which analyses the correlation between the intensity values of GLCM elements. In fact, let us consider an image with *N* grey levels. We can generate its $N \times N$ GLCM, whose elements are $p_{i,j}$ (where *i* and *j* are the row and column indexes, respectively). After $p_{i,j}$ normalization between 0 and 1, GLCM correlation is calculated as follows:

(2.2.3) $$Cor = \sum_{i,j=0}^{N-1} p_{i,j} \frac{(i-\mu_i)(j-\mu_j)}{\sqrt{(\sigma_i^2)(\sigma_j^2)}}$$

where μ_i, μ_j are defined as:

(2.2.4) $$\mu_i = \sum_{j=0}^{N-1} j\, p_{i,j}$$

(2.2.5) $$\mu_j = \sum_{i=0}^{N-1} i\, p_{i,j}$$

and σ_i, σ_j are defined as:

(2.2.6) $$\sigma_i = \sqrt{\sum_{j=0}^{N-1} p_{i,j}\,(j-\mu_i)^2}$$

(2.2.7) $$\sigma_j = \sqrt{\sum_{i=0}^{N-1} p_{i,j}\,(i-\mu_j)^2}$$

In practice, the GLCM correlation routine valuates the similarity between every pixel of the original image and the neighbour pixels placed at a certain offset. A GLCM is generated for each offset, and then the corresponding GLCM correlation is calculated according to the equation 2.2.7. We finally obtain a correlation function depending on the offset (figure 2.19). In general, high correlation value at a certain offset reflects a periodic structure (whose period is equal to that offset) in the original image.

We can derive a parameter from the correlation function of an image: the *correlation length*. The latter is calculated by fitting the correlation function with an exponential decay. But if the correlation function cannot be fitted properly, we can approximate the correlation length as the offset where the function is equal to 0.5 (as a sort of *correlation half-life*). In conclusion, GLCM correlation provides information about structural regularity within an image.

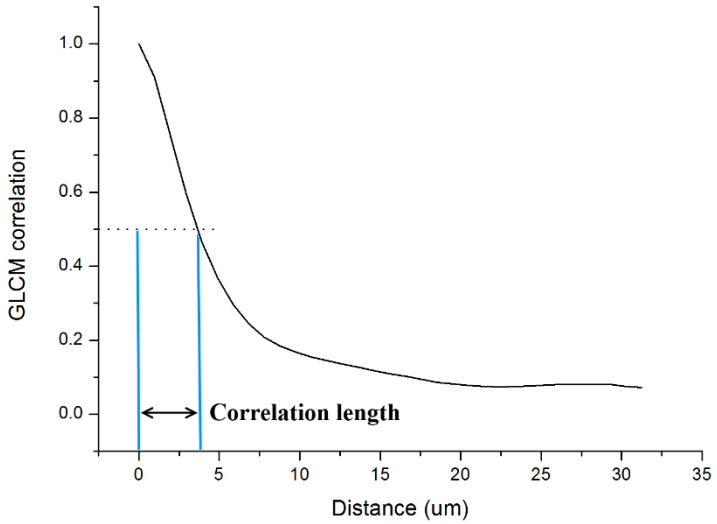

Figure 2.19 GLCM correlation function of the SHG image shown in figure 2.16. One GLCM was calculated for each offset between 0 and 32 pxl, and then averaged for all directions. Finally, GLCM correlation was calculated for each GLCM. The graph shows the obtained values as a function of the corresponding offset, which is expressed as distance between pixels. The dotted line represents a correlation value equal to 0.5 ("half-life" of the correlation function). The corresponding abscissa, determined by the blue line on the right, is the correlation length.

2.2.2 Analysis of Raman spectra

Fluorescence signal subtraction through polynomial fitting

The Raman effect in biological tissues is very weak: approximately, only one Raman photon is generated out of 10^8-10^9 excitation photons [56, 71], while fluorescence signal is some orders of magnitude greater (one out of 10^5-10^6, depending on the sample and the excitation wavelength). Then, considering that the fluorescence emitted by a biological tissue is broad, the Raman spectrum appears as a series of small peaks "on the top" of the fluorescence spectrum. Therefore, an automated method for removing fluorescence signal is necessary.

For biomedical applications, polynomial fitting is the most simple, convenient and (hence) used technique for such purpose. In fact, spectral-resolved fluorescence signal can be mathematically modelled as a polynomial function, whose order is chosen for properly removing the fluorescence baseline from the recorded signal, without subtracting the Raman peaks. Fourth to sixth order polynomials typically provide the best fitting [55]. On one hand, lower orders may not fit properly the baseline, creating artefacts; on the other hand, higher

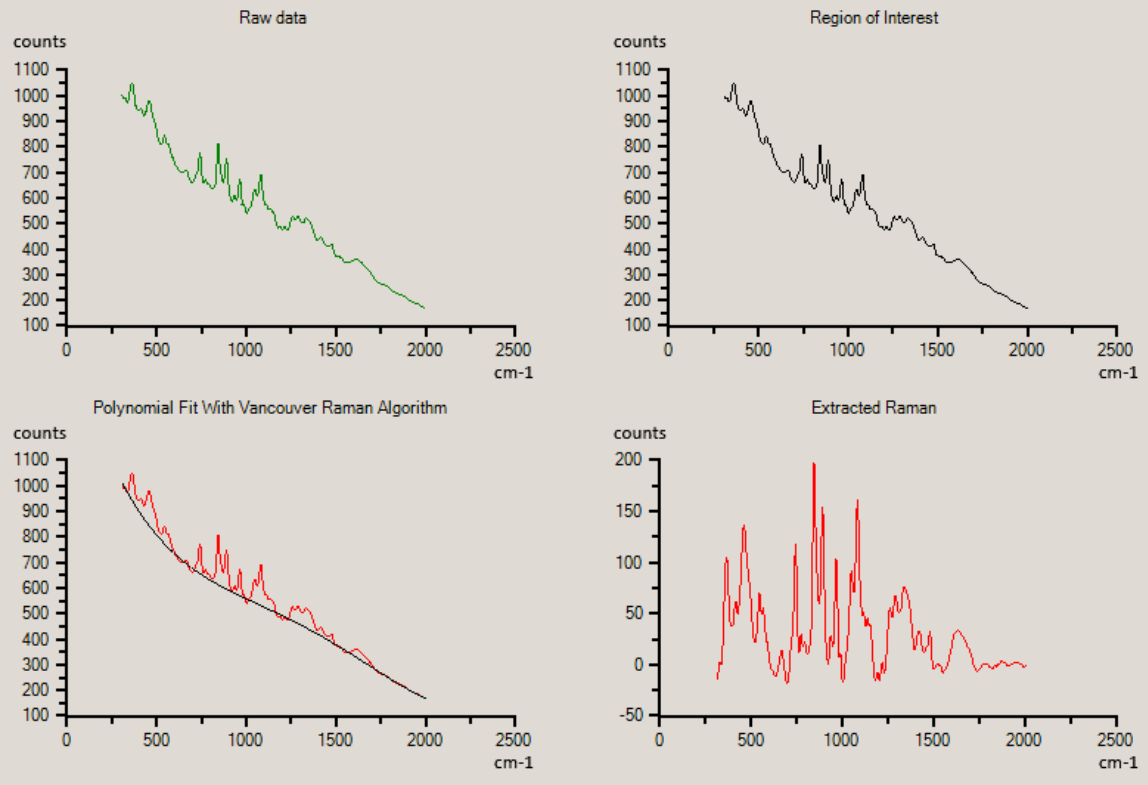

Figure 2.20 Fluorescence signal subtraction through the Vancouver Raman Algorithm routine. Top-left: raw spectrum acquired from an agar sample. Top-right: data selected for the analysis according to the chosen settings. Bottom-left: 4th grade polynomial fitting (black line) of fluorescence signal. Bottom-right: Raman spectrum obtained by subtracting the polynomial function.

orders may remove also Raman peaks. In fact, the n^{th} order polynomial can remove as many relative maxima/minima as the zeros of its derivative function, i.e. up to $(n - 1)$.

The most sophisticated algorithms for fluorescence removal use automated iterative routines in order to consider these problems. Vancouver Raman Algorithm is one of them (figure 2.20). The advantages [55, 72] of this software are:

- reduced computational time with respect to other methods;
- suppression of the artificial peaks on both ends of the analysed spectrum that may be introduced by other methods;
- less dependency on the choice of the polynomial order.

An alternative to polynomial fitting is Shifted Excitation Raman Difference Spectroscopy (SERDS). This technique takes advantage of the different spectral behaviour between fluorescence and Raman scattering: a small shift in the excitation wavelength causes an equal

shift in the Raman peaks, while leaving unchanged the fluorescence spectrum. Thus, the fluorescence signal can be removed by subtracting two spectra acquired with slightly different laser wavelengths. However, the resulting SNR is usually low [73]. In recent years, this technique has been improved by adopting a tuneable laser, allowing a continuous modulation of the excitation wavelength at a certain frequency. Thus, a large number of spectra (typically, one hundred) can be recorded, each one with a different excitation wavelength. Such approach sensibly increases the SNR [74]. Its main disadvantage consists of long acquisition times: a single spectrum is sufficient for polynomial fitting, while SERDS requires one spectrum for each excitation wavelength.

Data analysis through Principal Component Analysis (PCA)

Principal Component Analysis (PCA) is a simple and nonparametric method for extracting the most relevant information from a dataset by reducing its dimensions, which makes easier its analysis [75, 76]. Collected data consist in series of measurements for each dimension of the observed phenomenon; however, they usually contain noise. In fact, some data may be redundant. Therefore, if we represent the dataset as a matrix with respect to the basis of observed dimensions, then PCA transforms such matrix with respect to a new basis that contains only the most relevant information.

If we take N measurements for each one of the M physical dimensions observed, then the dataset is a $M \times N$ matrix ($\boldsymbol{X_0}$). By subtracting the mean of each series ($\bar{x}_i$) from all the acquired data of the corresponding series (x_{ij}, with $j = 1, 2 \ldots N$), we obtain a new $M \times N$ matrix $\boldsymbol{X}$. Then, the covariance matrix $\boldsymbol{C_X}$ of the new dataset is given by:

$$\boldsymbol{C_X} = \frac{1}{N-1}\, \boldsymbol{X}\, \boldsymbol{X}^T \tag{2.2.8}$$

At this point, we can calculate the eigenvalues and eigenvectors of $\boldsymbol{C_X}$ (which has M rows and M columns). The eigenvectors ($E_1, E_2 \ldots E_M$) represent the relations between different series of measurements – i.e. between data observed from different dimensions – while the corresponding eigenvalues express their significance. The higher the eigenvalue, the more significant the relation; for this reason, the eigenvectors corresponding to the highest eigenvalues are called *principal components* of the dataset. The PCA routine puts the eigenvectors in order of significance and discards the ones with lowest eigenvalues. A new matrix $\boldsymbol{P}$ is created from the remaining K eigenvectors:

(2.2.9) $$\boldsymbol{P} = (E_1 \ E_2 \ \dots \ E_K)$$

Thus, $\boldsymbol{P}$ has M rows and K columns. Finally, we can use the principal components for obtaining a new $K \times N$ dataset $\boldsymbol{Y}$:

(2.2.10) $$\boldsymbol{Y} = \boldsymbol{P}^T \boldsymbol{X}$$

$\boldsymbol{Y}$ contains only the most relevant data, since the PCA process re-expresses the original dataset by getting rid of its redundancy.

PCA has been widely applied to the study of Raman spectral dataset [46, 77-80]. In such particular application, we typically have N acquired spectra, each one consisting in M data points (corresponding to as many spectral channels of the detector). Once calculated the principal components (typically the first two or three eigenvectors of the covariance matrix), each acquired spectrum can be expressed as a linear combination of them:

(2.2.11) $$S_0^{(i)} = \sum_{j=1}^{N} c_j^{(i)} E_j$$

(2.2.12) $$S^{(i)} = \sum_{j=1}^{K} c_j^{(i)} E_j$$

where $S_0^{(i)}$ is i^{th} spectrum of the original dataset, $c_j^{(i)}$ is the coefficient (or score) related to the j^{th} principal component (E_j), and $S^{(i)}$ is the i^{th} spectrum of the new dataset. Therefore, each spectrum is specifically identified by its coefficients $c_j^{(i)}$. Moreover, the new spectra – being re-expressed only as a function of the most important components – show a better signal-to-noise ratio (SNR).

Data analysis through Artificial Neural Network (ANN)

An Artificial Neural Network (ANN) is a computing system made up of a number of simple, highly interconnected processing elements (called *nodes* or *neurons*) working in unison to solve specific problems. Basically, it is an information processing algorithm that is broadly inspired by the biological nervous system [81]. In fact, the textbook explanation of ANNs [82] typically use a very simplified description of biological neurons in order to stress the analogy with their artificial counterparts. The former are brain cells that communicate via short-lived electrical signals, and each one is connected to thousands of others. Therefore, a biological neuron is constantly receiving a multitude of incoming signals, which – broadly speaking – are processed by the cell. If the resulting signal exceeds a threshold, then the neu-

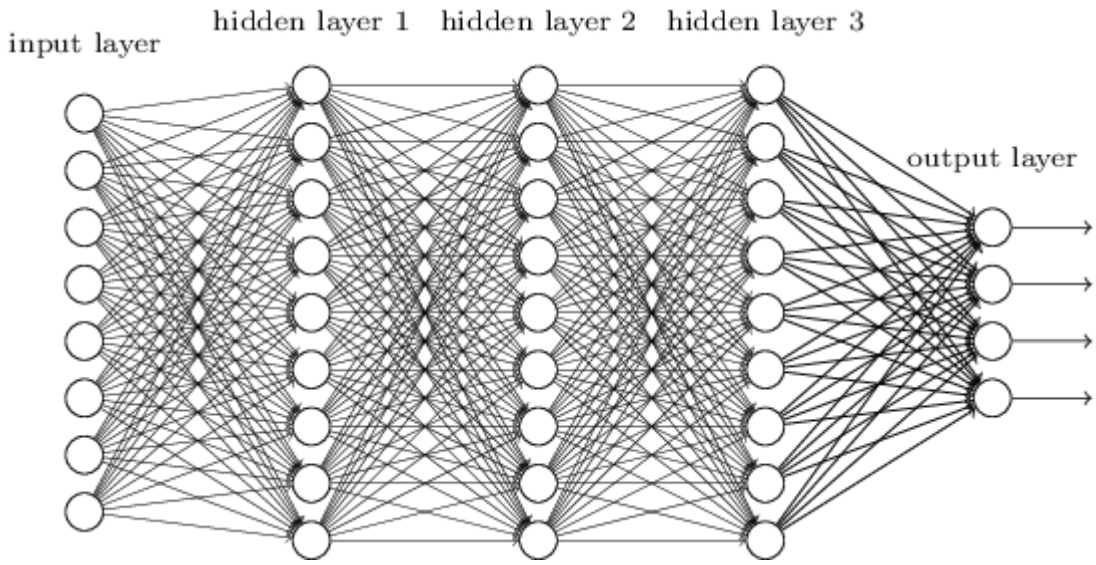

Figure 2.21 General scheme of an ANN. Neurons (portrayed as circles) are arranged in layers: the first layer provides the inputs to be processed by the neurons of the following layers. The final layer produces the network output. Picture taken from [83].

ron generates a voltage impulse in response, which in turn is transmitted to other neurons. In particular, in determining whether an impulse should be produced or not, some incoming signals produce (via neurotransmission) an inhibitory effect, whereas others are excitatory and promote impulse generation. The brain processes information through such architecture.

An ANN is characterised by a similar organisation. As shown in figure 2.21, its neurons are arranged in layers. Each neuron of a certain layer receives inputs from all the neurons of the previous layer; after processing such data, its output is sent in turn to all the neurons of the following layer. Within the single neuron, the received inputs are weighted and summed together; the output depends on the result being below/above a certain value. In fact, the response function f_j of the j^{th} neuron is given by:

(2.2.13) $$f_j(\boldsymbol{x}) = K\left(\sum_{i=1}^{N} w_{ij}\, g_i(\boldsymbol{x})\right)$$

where $\boldsymbol{x}$ is the input dataset of the network; N is the number of neurons in the previous layer; g_i is the response function of the i^{th} neuron of the previous layer; w_{ij} is the weight given to g_i by the j^{th} neuron; K is the activation function of the j^{th} neuron, defining its output. Typically, K is a binary function, whose value is determined by comparing the summation result with a threshold. Therefore, the first layer of the network provides data to be analysed, which are processed by the intermediate (*hidden*) layers; at the end, the last layer produces the final

output of the network. In this way, the incoming information is "collectively" processed by the neurons.

ANNs are typically configured for specific applications, such as pattern recognition or data classification, through a learning process. As learning in biological systems involves adjustments to the connections (synapses) between neurons, so it does in ANNs. Let us consider the case of supervised learning: an iterative process instructs the ANN to recognize certain features from a training dataset. In order to obtain the desired output, the weights w_{ij} of each single neuron are step-by-step adjusted through backward propagation of errors. In general, the weights of the $(t + 1)^{th}$ iteration are modified according to the following equation:

$$w_{ij}(t+1) = w_{ij}(t) + \eta \left(\frac{\partial C}{\partial w_{ij}}\right)_t + \xi(t) \tag{2.2.14}$$

where η is the learning rate, which influences the speed and quality of learning; C is the cost function, which measures the error (i.e. the difference between desired and obtained outputs); ξ is a stochastic term. The iterative process stops when the error (i.e. the derivative of C) tends to zero.

In conclusion, ANNs provide an analytical alternative to conventional techniques, which are often limited by strict assumptions of normality, linearity, variable independence [84] etc. In fact, such approach has the ability to implicitly detect a great variety of complex nonlinear relationships between variables [85]. For these reasons, ANNs have been applied in many fields and, in particular, to the study of Raman spectra [86-88]. In the case of supervised learning, for example, the network is trained to classify – through the output of a numerical code – each input spectrum belonging to the examined dataset.

2.3 Sample preparation

In the following paragraphs of this section, I will describe the samples used during my PhD and the procedures adopted for their preparation.

2.3.1 Human carotids

Atherosclerosis consists of the deposition and accumulation of fatty material and formation of plaques on the arterial wall (see chapter 3). In order to study such disease, human carotid *ex vivo* tissues affected by atherosclerotic plaques were imaged with NLO microscopy.

The carotids used for this analysis were excised during surgical procedures on five patients with atherosclerosis. The samples were fixed in formalin, embedded in paraffin and sliced with a microtome. Two slices were obtained from each specimen and examined with sagittal optical sectioning geometry: one was processed and labelled with H&E staining for common histopathological routine, and the other was left blank and placed on a glass microscope slide in order to be imaged with the custom-made multimodal microscope. In this way, I directly compared the acquired images with the corresponding histopathology results.

2.3.2 *In vitro* cell cultures

Malignant melanoma (MM) is a skin cancer characterised by strong aggressiveness and high mortality rate. The most frequent oncogenic mutations implicated in the development of MM affect either BRAF or NRAS genes (see chapter 4). In order to discriminate these tumour cell types, I acquired their Raman spectra by means of the XploRA INV microscope.

Three *in vitro* cell cultures were grown in incubator, each one of a different melanoma cell type: SKMEL28 (BRAF-mutated), SKMEL2 (NRAS-mutated) and wild-type (WT, i.e. without BRAF and NRAS mutations). Cells grew in glass-bottom dishes (MatTek, Ashland, MA, USA) with fetal bovine serum (FBS). The serum was removed and substituted with a phosphate-buffered saline (PBS) solution immediately before Raman measurements.

2.3.3 Tissue biopsies

The custom-made multimodal microscope can be used for studying both thin tissue slices (e.g. those described in section 2.3.1) and thick bulk samples. During my PhD, I tested such microscope on two tissues of the latter type: human bladder and rabbit aorta.

Human bladder

Urothelial carcinoma (UC) is a tumour affecting bladder (see chapter 5). Healthy and tumour tissues were excised during surgical procedures (Transurethral Resection of Bladder Tumours, TURBT) on a patient who had been diagnosed with UC. Each sample was immediately stored in formalin solution. Before measurements, I washed it in PBS and fixed it between a microscope slide and a coverslip (both made of quartz).

Rabbit aorta

Three New Zealand male, adult white rabbits were subjected to a cholesterol-rich diet in order to induce atherosclerosis. The animal were then sacrificed, and their aortas were excised through surgery. The specimens, containing the atherosclerotic plaques, were stored in formalin solution. As described in the previous paragraph, the samples were washed in PBS and sandwiched between a quartz slide and a coverslip immediately before measurements.

2.4 Data acquisition and analysis

In this section, I will report the procedures adopted for acquiring and analysing data.

2.4.1 Human atherosclerotic tissues

I set the Ti:Sapphire laser to mode-locking (i.e. pulsed) emission at 840 nm wavelength. Then I imaged human carotid samples through FLIM, TPEF and SHG microscopy. For such measurements, I used the 10× objective already mentioned in this chapter.

TPEF and SHG microscopy

TPEF and SHG images were simultaneously recorded with 20 μs/pxl dwell time, 500 × 500 μm^2 FOV and 512 × 512 pxl^2 resolution. For each technique, there was a different optical filter placed in front of the corresponding PMT: a large band-pass filter FF01-510/84 (Semrock, Rochester, NY, USA) for TPEF, a narrow band-pass filter FF01-420/10 (Semrock, Rochester, NY, USA) for SHG. TPEF and SHG mappings of each sample were reconstructed by attaching images recorded from adjacent positions. These large-FOV multiphoton images were compared to the corresponding images of H&E stained tissue sections. The histopathological examination identified four main tissue types: angiogenesis and inflammation, fibrous cap, calcification, necrosis (see chapter 3). In addition, fibrous cap tissues were classified as thin- or thick- depending on their thickness (below or above 0.5 mm [89], respectively), a parameter related to plaque stability. For each one of these tissues, regions of interest (ROIs) sizing 128 × 128 pxl^2 were cut out from the recorded images, and then analysed (as described below). For backward-detected TPEF and SHG image analysis, I selected 73 ROIs for thick fibrous cap, 40 for thin fibrous cap, 14 for

calcification, 125 for necrosis and 75 for angiogenesis and inflammation. For forward-detected SHG image analysis, I selected 36 ROIs for lipid deposition and 38 for fibrous cap.

I combined multiple methods for analysing and characterising atherosclerotic tissues. TPEF/SHG ratio was calculated for all the pixels and averaged for each ROI. I studied TPEF ROIs, selected from all plaque tissues, by calculating their GLCMs by means of a MATLAB (Mathworks, Natick, MA, USA) routine [25]. Then, for each image, the GLCM correlation length was calculated using a custom-made program for LabVIEW (National Instruments, Austin, TX, USA). I selected SHG ROIs from thin and thick fibrous cap tissues, and calculated their FFT using an ImageJ built-in routine [90]. Then image anisotropy was evaluated by means of the aspect ratio of its FFT profile. Such parameter, corresponding to the minor-to-major axis ratio of the elliptic FFT profile, was calculated by considering the ratio of the two eigenvalues of the covariance matrix, as described in [91]. I also calculated the GLCM correlation length of these ROIs. In addition, the average forward-to-backward (F/B) ratio of SHG emission was calculated from selected lipid deposition and fibrous cap ROIs.

FLIM

I acquired FLIM images from all tissue types, with 200 × 200 μm^2 FOV, 128 × 128 pxl^2 spatial resolution, and temporal resolution of 256 channels over 12.5 ns TAC characteristic. Two sets of optical filters were (alternatively) placed in front of the PMH-100 detector: one consisting of a single filter FF01-470/28 (Semrock, Rochester, NY, USA) and the other one of two filters – FF500-Di01 and FF01-510/84 (Semrock, Rochester, NY, USA) – in cascade. Thus, for both spectral ranges, I recorded 10 ROIs from fibrous cap (both thin- and thick-) regions, 10 from calcification, 10 from necrosis and 10 from angiogenesis and inflammation.

FLIM data analysis was done through SPCImage, as explained in section 2.2.1. Therefore, from each image and for each spectral range, I obtained the distributions of four lifetime parameters: τ_1, τ_2, τ_m, a_1/a_2. First, I calculated the mean of each distribution, and then I obtained a mean value for each parameter, tissue type and spectral range.

2.4.2 Melanoma cells

I selected the 532 nm excitation laser of the commercial Raman setup and acquired 50 spectra for each cell type (SKMEL2, SKMEL28, WT) from as many cell nuclei. Acquisition

was performed by scanning an area (5 μm diameter) centred on each observed nucleus for 120 seconds. Spectra were recorded between 300 and 1900 cm^{-1} by the 1800 lines/mm grating. I used a Plan-Apochromat 60× objective (Nikon; NA = 1.27, WD = 0.17 mm).

Since both the glass-bottom dish and the PBS solution gave background signal, I processed each acquired spectrum for removing such spurious contribution. Then I used the Vancouver Raman Algorithm for removing the fluorescence baseline and, finally, the resulting Raman spectra were analysed through PCA. Additionally, I processed them also with an ANN routine (Neural Network Pattern Recognition, NNPR) based on MATLAB. The aim of both these approaches is to provide an automated classification for newly acquired spectra of cells whose type is unknown.

2.4.3 Bulk tissue samples

Combined TPEF-Raman acquisitions were performed in the same way on both human bladder and rabbit aorta samples through the custom-made multimodal microscope. I set the Ti:Sapphire wavelength to 785 nm, switching between mode-locked and continuous wave emission for TPEF and Raman measurements, respectively. I used the same 10× objective already mentioned in this chapter.

Human bladder

TPEF signal was detected in the 468-552 nm spectral range. 12 images (300 × 300 μm^2, 512 × 512 pxl^2, 20 μs/pxl) were recorded from as many tissue regions: 6 from healthy bladder and 6 from UC. Then, for each region, I acquired a Raman spectrum by scanning its central area (100 μm size) for 120 seconds.

Rabbit aorta

The same procedure described in the previous paragraph was adopted also for studying rabbit aorta. TPEF images and Raman spectra were recorded from 6 arterial tissue regions affected by cholesterol deposition.

Chapter 3: Nonlinear imaging for the diagnostics of atherosclerosis

3.1 Introduction

Coronary heart disease (CHD) is the most common type of heart disease, killing over 370'000 people annually in the United States [92]. CHD is caused by atherosclerosis: a slow, progressive accumulation of cholesterol, fatty substances, cellular waste products, macrophages, calcium and fibrin in the artery wall, which can generate plaques [93, 94]. Several risk factors (systemic hypertension, obesity, cigarette smoking, inactivity, etc) predispose such condition, but hypercholesterolemia is an absolute prerequisite [95]. Moreover, high cholesterol is often associated with Western diet and lifestyle, which involve eating foods with high content in saturated fats and not getting enough physical exercise. Thus, complications of atherosclerosis are the most common causes of death in Western societies [96]. In fact, once the plaque is set, its substances may stimulate the production of other cells in the innermost layer of the arterial wall; at the same time, fat and connective tissue build up within and around it. This process finally results in hardening and narrowing of arteries, and in partially or totally blocking the blood flow. However, the mayor risk related to atherosclerosis consists in sudden rupture of vulnerable plaques [97]. This event delivers thrombotic material within blood and may have life-threatening effects, such as heart attack or stroke, when a coronary or a brain artery is occluded. Therefore, assessing both presence and vulnerability of atherosclerotic plaques at an early stage is extremely important in order to decide a proper treatment of the disease. In this regard, plaque stability is highly correlated to its composition [98]. Stable plaques are rich in smooth muscle cells and show a thick fibrous cap, while unstable ones are characterised by the presence of a large necrotic core, calcification, macrophages, few smooth muscle cells, and a thin cap.

The severity of atherosclerosis is generally assessed by histopathological examination of tissue biopsy. Although the standard hematoxylin/eosin (H&E) stain can be used for arterial tissue diagnostics, specific stains such as Van Gieson (for collagen) or Oil Red-O (for lipids) are more suitable to discriminate plaque depositions from arterial connective tissue and to distinguish the most abundant plaque components, such as cholesterol. Despite its popularity, histopathological examination is limited in terms of achievable contrast for con-

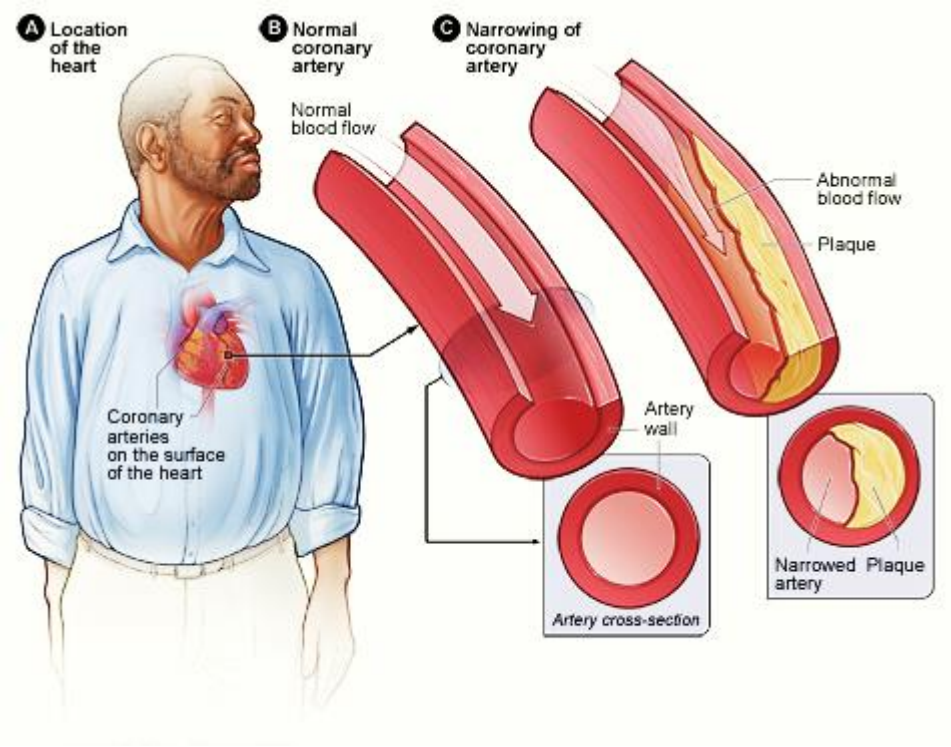

Figure 3.1 Figure A): location of the heart in the body. Figure B): a normal coronary artery with normal blood flow. The inset image shows a cross-section of a normal coronary artery. Figure C): a coronary artery narrowed by an atherosclerotic plaque. The plaque buildup limits the flow of oxygen-rich blood through the artery. The inset image shows a cross-section of the plaque-narrowed artery. Picture taken from [99].

nective tissue and requires a relatively long tissue processing and staining procedures. Immunohistochemistry is a more specific technique for selectively imaging target molecules through specific stains, but such staining processes are even more time-consuming and costly. In general, diagnostic methods are limited to morphological analysis of the examined tissues, whereas an exhaustive characterisation requires a morpho-functional approach.

In this framework, NLO microscopy is a valid, label-free alternative to standard histopathological methods [100, 101]. In fact, specific contrast between collagen fibre bundles – which are highly concentrated in the fibrous cap – and lipids can be generated using NLO imaging by taking advantage of the signal provided by tissue endogenous fluorophores. Moreover, the combination of different NLO techniques in a multimodal scheme allows obtaining both morphological information (similarly to standard histopathological methods) and functional information on the examined tissue [102-104]. Such morpho-functional approach can be applied to study both thin and bulk tissue samples

and, in the latter case, potentially without the need for an excision. Therefore, NLO microscopy represents a powerful tool for tissue characterisation and pathology assessment. In particular, TPEF microscopy is useful for imaging lipids and elastic fibres [105]; FLIM allows the characterisation of various tissue regions based on the fluorescence lifetime [106]; SHG microscopy provides background-free imaging of anisotropic biological molecules with large hyperpolarizability, such as collagen [107] and cholesterol [108].

Therefore, I combined TPEF, FLIM and SHG microscopy for characterising atherosclerotic arterial tissues obtained from human carotid *ex vivo* specimens.

3.2 Materials and methods

3.2.1 Sample preparation

As explained in section 2.3.1, I studied five formalin-fixed, paraffin-embedded human carotid artery slices, cut with sagittal optical sectioning geometry and placed on a microscope slide. Also, from each carotid, an additional slice was prepared, processed and labelled with H&E staining for common histopathological routine. This study was conducted according to the tenets of the Declaration of Helsinki.

3.2.2 Data acquisition and processing

For this research line, I used the custom-made multimodal microscope described in section 2.1.1. After setting the laser to mode-locking emission at 840 nm, TPEF and SHG images were simultaneously recorded with 500 × 500 μm^2 FOV in two separate spectral ranges: 468-552 nm and 415-425 nm, respectively. Then, images recorded from adjacent positions were attached together in order to obtain a multiphoton mapping of each sample. Figure 3.2 shows a comparison between TPEF and SHG mappings with their corresponding H&E stained counterparts. Four main tissue types were recognized by histopathological examination: angiogenesis and inflammation, fibrous cap, calcification, necrosis. These tissues were highlighted by coloured insets in figure 3.2. In particular, the colour-code was blue for angiogenesis and inflammation, green for fibrous cap, yellow for necrotic tissue, and red for calcification. Finally, FLIM images with 200 × 200 μm^2 FOV were recorded specifically from these tissue types and from two spectral ranges: 456-484 and 500-552 nm.

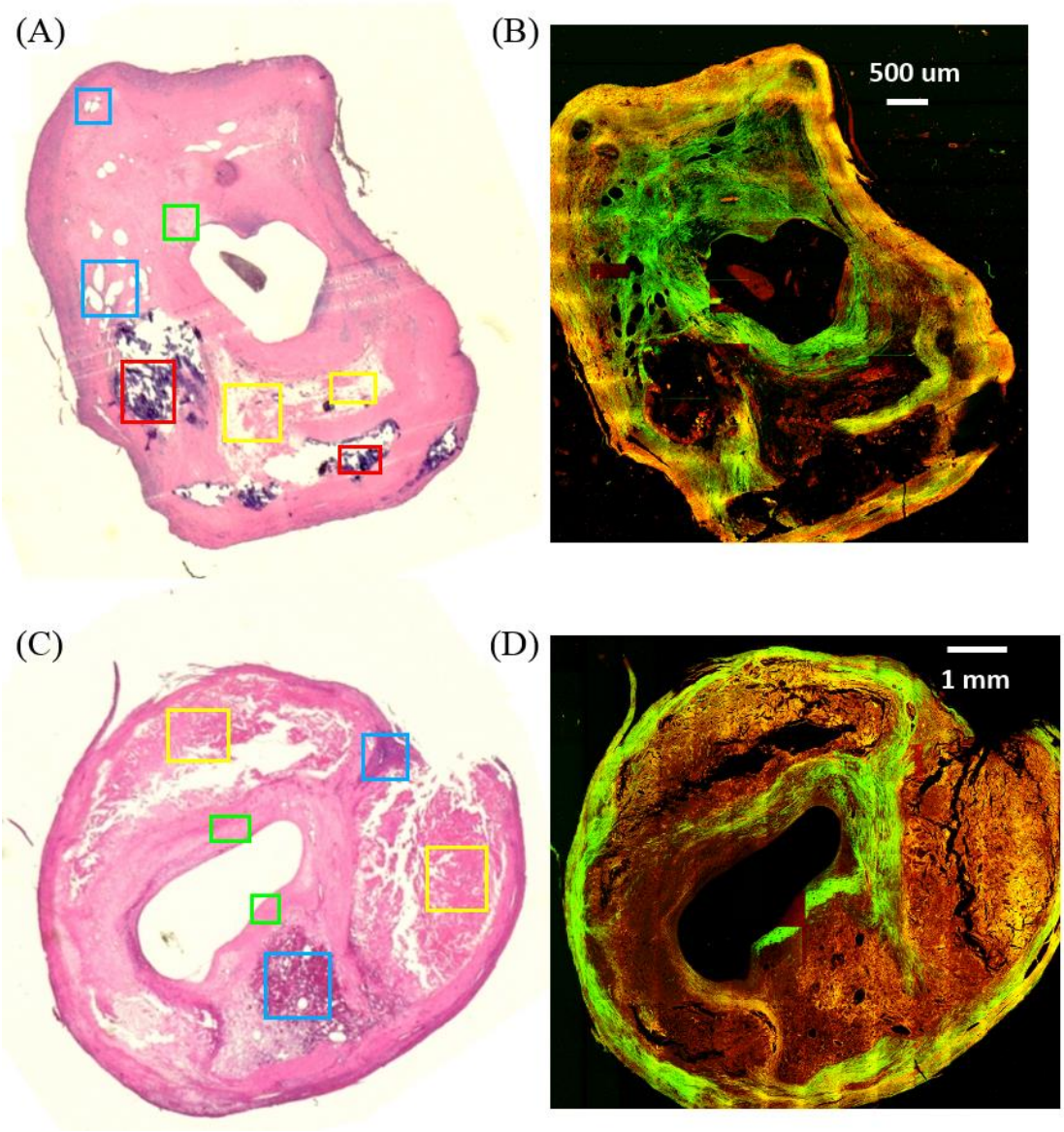

Figure 3.2 Comparison between combined TPEF/SHG mappings of two carotid specimens affected by atherosclerosis and their corresponding histopathological results. A) and C): wide-field images of H&E stained slices. Histopathological annotation was done through coloured squared insets: blue for angiogenesis and inflammatory tissue, green for fibrous cap, yellow for necrotic tissue, red for calcification. B) and D): false-colour images merging TPEF (marked in red) and SHG (marked in green) mappings. B) and D) mappings were obtained by stitching 12 × 13 and 14 × 13 images, respectively. Each single image was acquired with 500 × 500 μm^2 FOV and 512 × 512 pxl^2 resolution.

The regions of interest (ROIs) of each tissue were selected from FLIM, TPEF and SHG images, and then analysed (as described in section 2.4.1) in order to obtain the following parameters:

- TPEF/SHG ratio of ROIs selected from all regions;

- GCLM correlation length of TPEF ROIs selected from all regions;
- GLCM correlation length and FFT aspect ratio of SHG ROIs selected from thin and thick fibrous cap regions;
- F/B ratio of SHG ROIs selected from lipid deposition and fibrous cap regions;
- lifetime parameters (τ_1, τ_2, τ_m, a_1/a_2) selected from all regions and obtained for two spectral ranges (456-484 and 500-552 nm).

3.3 Results and discussion

3.3.1 Multiphoton mappings

As shown in figure 3.2, TPEF and SHG mappings of the examined carotid specimens show a good agreement with the corresponding white-light images taken from H&E stained histological sections. SHG signal (marked in green) originates from collagen and cholesterol, and it might be used for highlighting the fibrous cap. On the other hand, SHG signal is almost absent within both calcification and necrotic regions, where TPEF signal (marked in red) dominates. H&E stained images, instead, show relatively higher concentration of hematoxylin in angiogenic and inflamed or calcified tissues, while necrosis and fibrous cap are targeted though eosin. Thus, without the need of any specific stain, multiphoton imaging can provide high-resolution information (complementary to the histopathological results) about the fibrous cap size and the molecular composition of different tissues, which might be exploited for the purpose of discriminating among them.

3.3.2 SHG-based analysis

Backward-detected SHG ROIs, selected from thin and thick fibrous cap regions, were analysed using two different robust scoring methods, aimed at determining anisotropy (FFT) and correlation length (GLCM).

In fact, the FFT intensity profile of a ROI is elliptic, whereas its eccentricity depends on the anisotropy level of the image: if all the observed objects are arranged along a privileged direction, the FFT ellipse appears very elongated and its minor-to-major axis ratio (aspect ratio) is close to 0. Instead, high isotropy images have circular FFT profiles and aspect ratios close to 1. Therefore, FFT analysis was used for characterising the geometrical orientation of SHG emitters (collagen, cholesterol) at a supramolecular scale within the fibrous cap. For example, a bundle of aligned collagen fibres decreases the aspect ratio, while randomly dis-

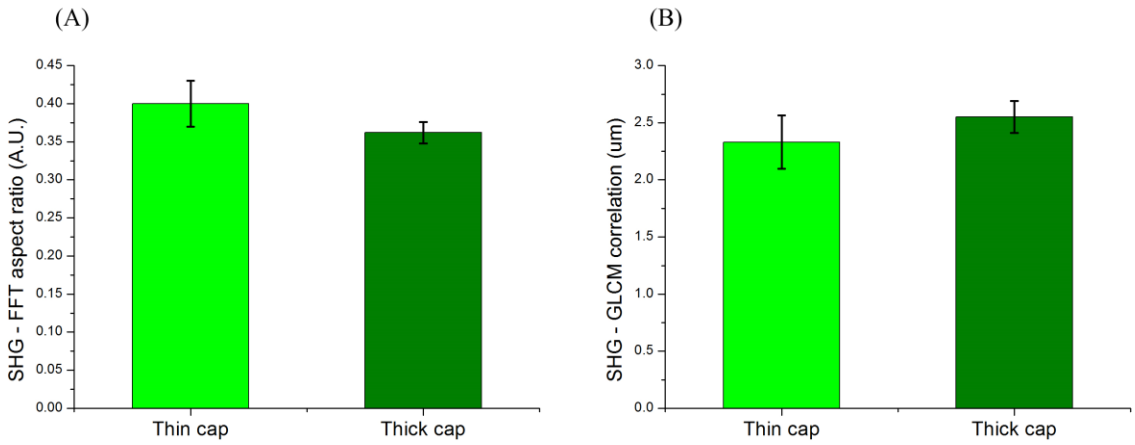

Figure 3.3 Mean values and standard errors (SEs) of A) FFT aspect ratio and B) GCLM correlation length, obtained by analysing SHG images acquired from thin and thick fibrous cap regions.

tributed cholesterol clusters tend to increase it. In this regard, I tried to estimate if the thickness of the fibrous cap correlates to its anisotropy level. The FFT aspect ratio was calculated and used as a score for isotropy/anisotropy of each ROI. The average results for thin and for thick fibrous cap regions are reported in a bar graph in figure 3.3A. The values obtained from the two regions were found to be not statistically different at the 0.05 level after a two-sample statistical t-test ($p = 0.05$) analysis, meaning that the alignment of collagen fibres and the cholesterol distribution in the fibrous cap may not depend on its size. Therefore, such feature cannot be exploited to assess the risk of plaque rupture.

Further characterisation was provided by the GLCM correlation function, which evaluates how much the grey level of each pixel correlates to that of its neighbours as a function of the inter-pixel distance. In fact – as explained in section 2.2.1 – the GLCM correlation length can be taken as a measure of a typical length for structures with periodicity: if the image has a periodic structure, a certain value of the neighbour index shows high correlation value. In this case, I used such parameter for measuring the typical length scale of supra-molecular assemblies of SHG emitters (i.e. collagen fibres and cholesterol formations). The GLCM correlation length represents the typical fibre diameter or cluster size observed in the examined SHG image. Therefore, I calculated the correlation length for each ROI and averaged for both thin and thick fibrous cap regions. The results are reported in a bar graph in figure 3.3B. Again, the values obtained from the two regions were found to be not statis-

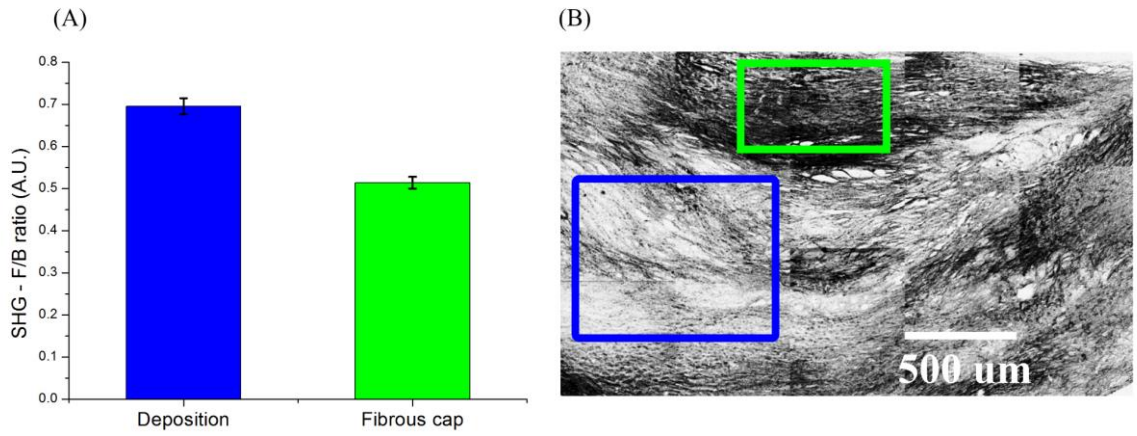

Figure 3.4 A): Mean values and SEs of the SHG F/B ratio measured from fibrous cap (green bar) and lipid deposition (blue bar) regions. B): SHG F/B mapping, showing both fibrous cap (green square) and deposition (blue square) regions.

tically different at the 0.05 level after a two-sample statistical t-test (p = 0.05) analysis. Thus, the typical size of collagen fibres and cholesterol clusters seems unrelated to fibrous cap thickness. In general, the findings based on FFT and GLCM analysis may indicate that fibrous cap regions maintain same anisotropy and organization of their second-harmonic emitters, regardless of their thickness and (as explained in the introduction of this chapter) of the related plaque vulnerability.

Then, I used the forward-backward SHG ratio as a parameter for analysing the ROIs selected from fibrous cap and lipid deposition regions. In fact, as discussed in section 1.1.2, the angular distribution of SHG emission depends on the geometry of its emitters. Consequently, the F/B SHG ratio in these tissues depends on the presence and spatial organization of collagen and cholesterol contents; in particular, such parameter can be used as a way to compare their relative abundancy in the examined regions. Thus, the average F/B ratio was calculated for each ROI and averaged for each tissue type (figure 3.4). F/B SHG ratios calculated from fibrous cap regions were found to be significantly lower with respect to those ones calculated within deposition regions; the values obtained from the two tissue types were found to be statistically different at the 0.05 level after a two-sample statistical t-test (p = 0.05) analysis.

These results seems to reflect different cholesterol-to-collagen content ratios of the two regions. In fact, cholesterol plaques are known to generate higher F/B SHG ratio than colla-

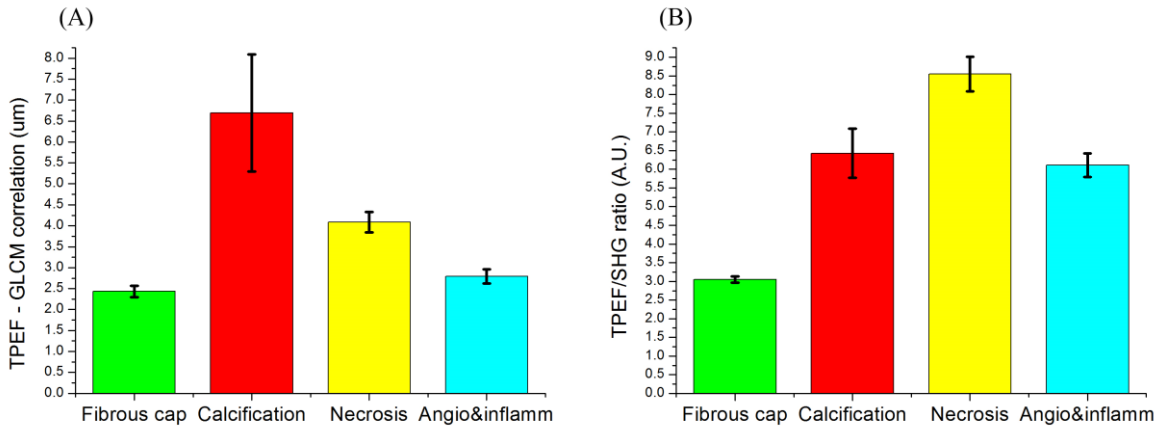

Figure 3.5 GLCM correlation length (A) and TPEF/SHG (B) mean values and SEs obtained from all tissue types: fibrous cap (green), calcification (red), necrosis (yellow), angiogenesis and inflammation (cyan).

gen fibres in normal arterial wall [101]. Since the fibrous cap is mainly made of collagen fibres, while cholesterol is a major component of atherosclerotic plaques, the obtained results may be interpreted in terms of their relative abundancies in the examined tissues.

3.3.3 TPEF-based analysis

TPEF imaging takes advantage of intrinsic fluorescent molecules such as lipids, collagen and elastic fibres for providing label-free imaging of biological tissues. In order to highlight morphological differences between the examined tissues, TPEF ROIs were analysed through the GLCM method. The results are shown in Figure 3.5A: GLCM correlation length is lower in fibrous cap, and higher in calcification regions. All regions are found to be statistically different at the 0.05 level after a two-sample statistical t-test ($p = 0.05$) analysis, except for the comparison between the fibrous cap ROIs and the angiogenesis and inflammation ROIs. These findings might be explained in terms of typical diameter of collagen fibres and size of calcium/lipid agglomerates, as suggested in [109].

The TPEF/SHG ratio of the examined atherosclerotic tissues was calculated in order to take advantage of their different molecular composition. As shown in Figure 3.5B, TPEF/SHG ratio in fibrous cap is significantly lower than in other regions, and it is higher in necrosis. All regions were found to be statistically different at the 0.05 level after a two-sample statistical t-test ($p = 0.05$) analysis, except for the comparison between the calcification ROIs and the angiogenesis and inflammation ROIs. High values of the TPEF/SHG ratio found in

fibrous cap ROIs are related to the higher collagen content found in these ROIs and, therefore, to a higher SHG emission. On the other hand, necrotic tissue is known to emit increased autofluorescence with respect to normal tissue [110-113].

Thus, a combination of GLCM correlation length and TPEF/SHG ratio provides insights about both morphological and molecular information of the examined tissues, allowing discrimination among all of them.

3.3.4 Fluorescence lifetime analysis

FLIM microscopy allows further analysis of plaque molecular composition based on the analysis of fluorescence decay dynamics. Time-resolved intrinsic fluorescence signal was recorded from all tissue types and then analysed for obtaining the corresponding decay parameters after deconvolution and fitting (figure 3.6). Moreover, two spectral ranges – 456-484 and 500-552 nm – were chosen for detecting fluorescence of (respectively) collagen [114] and lipids [115], close to their corresponding fluorescence emission peaks.

Mean and SE of each parameter are reported in figure 3.7 for 456-484 nm and 500-552 nm spectral ranges, respectively. Different tissue types are characterised by significant differences in lifetime parameters measured in both spectral ranges, particularly the short component τ_1 at 456-484 nm and the mean lifetime τ_m at 500-552 nm. Although a clear justification of these results cannot be provided in this framework, a possible explanation may be given considering the difference in terms of fluorescence lifetime between collagen and lipids. In fact, higher values of mean lifetime measured in fibrous cap are consistent with a longer fluorescence lifetime of collagen with respect to lipids [106, 109].

Differences in the molecular composition (above all, the collagen-to-lipid ratio) of the examined tissues can be observed also by comparing each parameter values obtained from the two spectral ranges. Fibrous cap parameters remain almost unchanged between the two spectral ranges, while the other tissues show significant shifts. Such findings can be discussed by considering that:

- collagen fluorescence is detected not only in the 456-484 nm, but also in the 500-552 nm range;
- the lipid content in fibrous cap is relatively small.

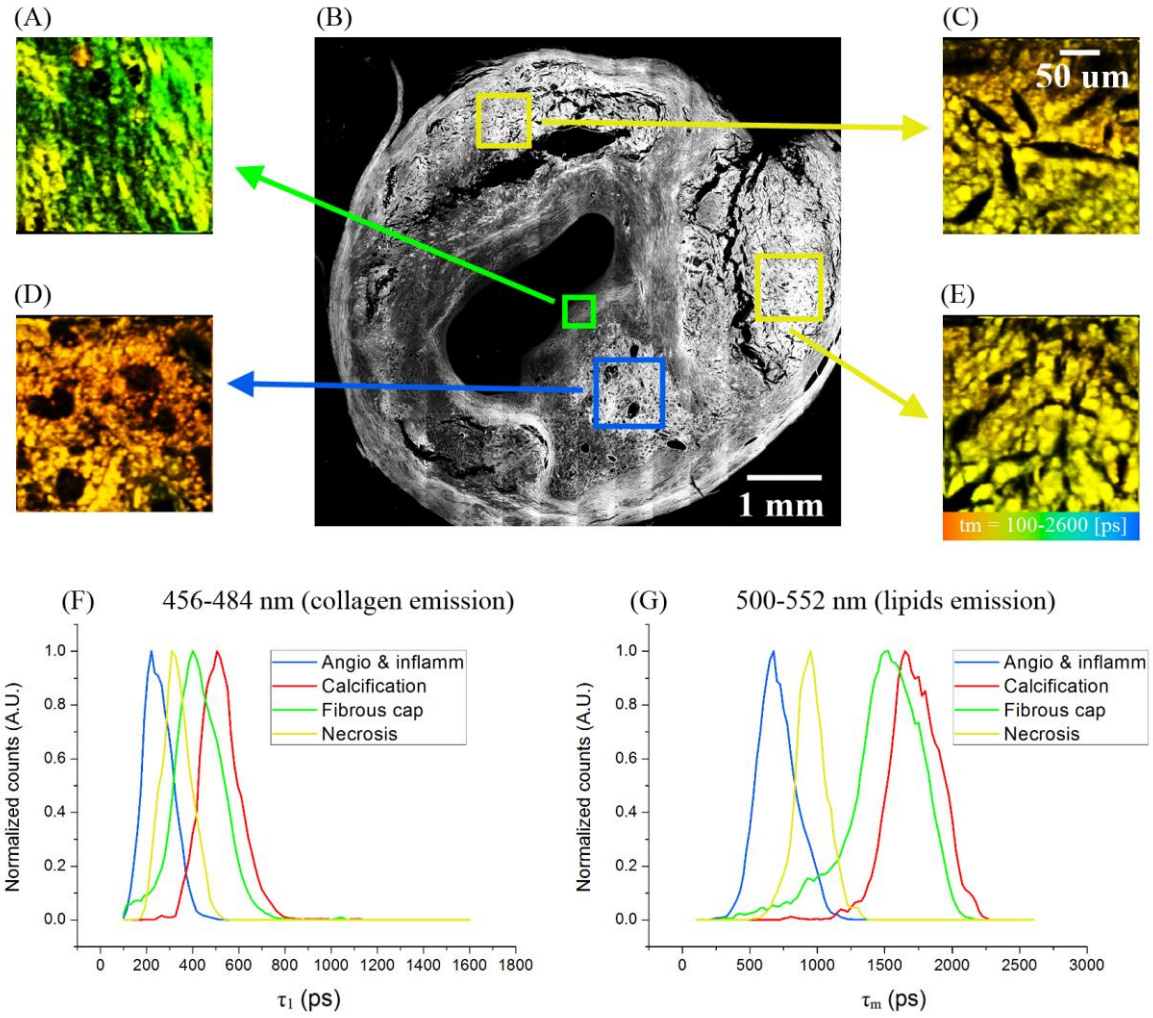

Figure 3.6 TPEF mapping (B) of a human carotid specimen, FLIM images recorded from different tissue types, and distributions of lifetime parameters for all the examined tissues. A), C), D) and E): false colour τ_m images (200 × 200 μm^2 FOV, 128 × 128 pxl^2) acquired at 456-484 nm from fibrous cap (green square), necrosis (yellow) and angiogenesis and inflammation (blue). F) and G): τ_1 distributions at 456-484 nm and τ_m distributions at 500-552 nm, respectively.

Therefore, the fibrous cap fluorescence emission recorded in both spectral ranges is mainly due to collagen. The fluorescence lifetime of fibrous cap reflects only its collagen content, and thus it does not change when measured at 456-484 nm or 500-552 nm. Instead, the other tissues – calcification, necrosis, angiogenesis and inflammation – show diversified molecular contents (collagen, calcium, lipids and other fluorescent molecules) with different relative abundancies. In their cases, the fluorescence detected at 456-484 nm and that one detected at 500-552 nm are typically generated from different fluorophores, resulting in different lifetime values (i.e. the observed shifts between the two spectral ranges). Hence,

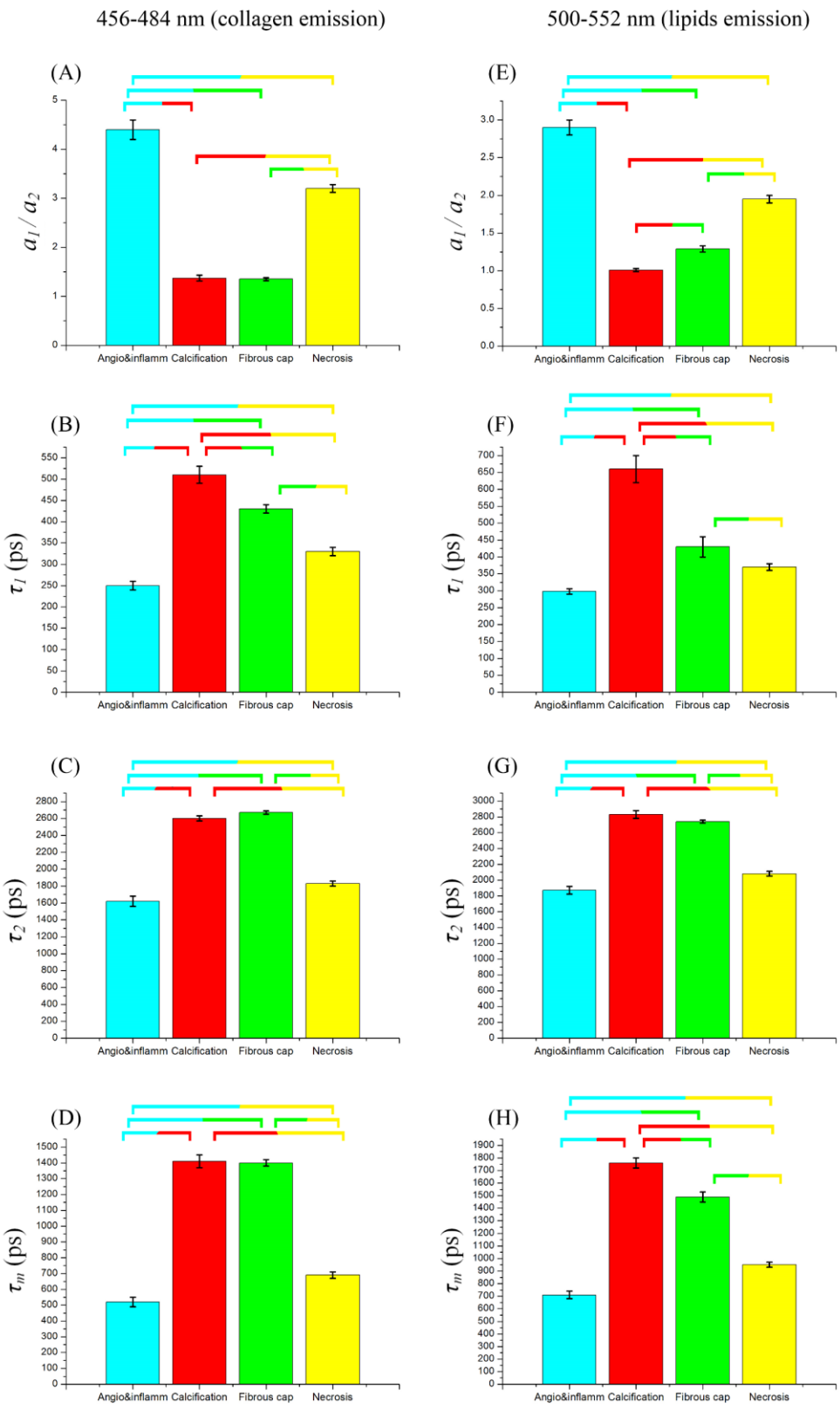

Figure 3.7 A-D) and E-H): mean values and SEs of each FLIM parameter distribution recorded in the 456-484 nm and 500-552 nm spectral ranges, respectively. Each coloured line connects a pair of bars being statistically different at the 0.05 level after a two sample statistical t-test (p = 0.05) analysis.

the presented approach, based both on spectral- and time-resolved information about fluorescence emission, provides additional tools for characterising atherosclerotic tissues.

3.4 Conclusions

In this study, combined FLIM, TPEF and SHG microscopy was used for characterising human carotid *ex vivo* specimens affected by atherosclerosis. Thin tissue slices were examined using sagittal optical sectioning geometry in order to obtain images comparable with histopathological examination.

I used image analysis techniques (FFT, GLCM) and scoring methods (F/B SHG ratio, TPEF/SHG ratio) for studying morphological and physiological features of atherosclerotic tissues. Organization and size of both collagen fibres and cholesterol clusters within fibrous cap regions were analysed, finding no significant differences related to fibrous cap thickness. On the other hand, organization and molecular types of SHG emitters were found to be very different between the lipid deposition of the plaque and the fibrous cap. Then, I measured the typical size of supramolecular formations – such as collagen fibres and calcium/lipid agglomerates – within four tissue types having different histopathological features: calcification, necrosis, fibrous cap, angiogenesis and inflammation. This datum can be integrated with additional information on the molecular composition of each tissue, which was provided by measuring the ratio between TPEF and SHG emission. Combined together, these parameters allowed discriminating all the examined regions. Finally, while TPEF and SHG imaging proved to be useful tools for plaque characterisation, the analysis of FLIM images provided more detailed information on the various tissue types having different histopathological features. Depending on both the molecular content and the environment of the examined tissue, fluorescence lifetime parameters were used for successfully discriminating all regions because of their different composition.

In conclusion, the presented imaging techniques and image analysis methods allowed analysing and discriminating the atherosclerotic tissue types normally identified for histopathological diagnosis. Therefore, combining FLIM, TPEF and SHG microscopy might represent a powerful complement, and could become a valid alternative, to standard histopathological methods for diagnosing and staging atherosclerosis.

Chapter 4: Classification of Melanoma cell lines through Raman spectroscopy

4.1 Introduction

Malignant melanoma (MM) is the most dangerous form of skin cancer, due to its strong aggressiveness and the high mortality rate in case of late diagnosis: five-year survival rates for patients with metastatic disease are below 10% [116, 117]. MM develops when unrepaired DNA damages to skin cells – most often caused by ultraviolet radiation from sunshine – trigger mutations (i.e. genetic defects) that lead the melanocytes to multiply rapidly and form a malignant tumour [118]. In particular, the most frequent oncogenic mutations involve BRAF and NRAS genes (approximately 50% and 20% of all melanomas, respectively [119, 120]); mutations in more than one of these genes are seldom found concurrently in the same tumour.

Clinical treatment of MM consists of a combination of surgery, traditional cytotoxic chemotherapy, targeted therapies, and immune-based therapies. The response to both conventional chemotherapy and targeted agents depends on the specific mutation involved in the carcinogenesis. Therefore, assessing the gene mutation type is extremely important for proper clinical treatment of the disease. Current methods of melanoma mutation analysis are based on DNA sequencing [121] or polymerase chain reaction (PCR [122]); however, these techniques are destructive and take a long time (hours).

Raman spectroscopy is a possible alternative to the standard methods. It provides a fast, non-destructive, label-free optical tool for studying living cells [50, 123] and, specifically, for detecting the cancer ones [124-126]. In fact, the spectrum of scattered light from observed cells reflects the vibration modes (the "fingerprints") of their molecules. Thus, Raman spectroscopy could be used for investigating the molecular composition of different cell types, highlighting their differences.

Therefore, I used a commercial Raman microscope (XploRA INV, Horiba, Kyoto, Japan) for studying *in vitro* melanoma cells with specific mutations of either BRAF or NRAS genes.

4.2 Materials and methods

4.2.1 Sample preparation

As explained in section 2.3.2, I studied three *in vitro* melanoma cell cultures, each one of a different cell type: SKMEL28 (BRAF-mutated), SKMEL2 (NRAS-mutated) and wild-type (WT, neither BRAF- or NRAS-mutated). During each measurement, a glass-bottom dish (MatTek, Ashland, MA, USA) containing the cell culture with PBS solution was imaged and analysed with the Raman microscope.

4.2.2 Data acquisition and processing

For this study, I used an XploRA INV (Horiba, Kyoto, Japan) inverted, confocal Raman microscope (see section 2.1.2). In order to acquire a Raman spectrum from each cell nucleus under investigation, a 5 μm size area centred on the nucleus was scanned with the 532 nm excitation laser. The scattered light was backward collected and detected between 300 and 1900 cm^{-1}. 50 Raman spectra were recorded for each cell type (150 in total).

The acquired spectra were processed for removing both the spectral contributions of glass-bottom dishes [57] and PBS, and the fluorescence emission from the sample. The resulting Raman spectra were analysed through PCA in order to obtain the coefficients of the first six principal components (see equation 2.2.12). A classification method was developed based on linear combinations of such coefficients. In addition, the Neural Network Pattern Recognition (NNPR) routine was used for generating an alternative classification algorithm.

4.3 Results and discussion

4.3.1 Background and fluorescence removal

Glass is known [57] to give a spectral contribution to Raman spectra for 532 nm excitation wavelength. Also, by comparing the Raman spectra acquired on a MatTek dish with and without PBS, I verified that the latter shows a large Raman peak around 1550-1750 cm^{-1} (figure 4.1A). In order to remove such contributions, I normalized the "raw" Raman spectrum of each cell nucleus and simply subtracted the normalized Raman spectrum of both glass-bottom dish and PBS. Following such operation, the resulting Raman spectra of melanoma cells were further processed: the fluorescence baseline was automatically removed by a 5^{th} grade polynomial fitting routine, performed through the Vancouver Raman

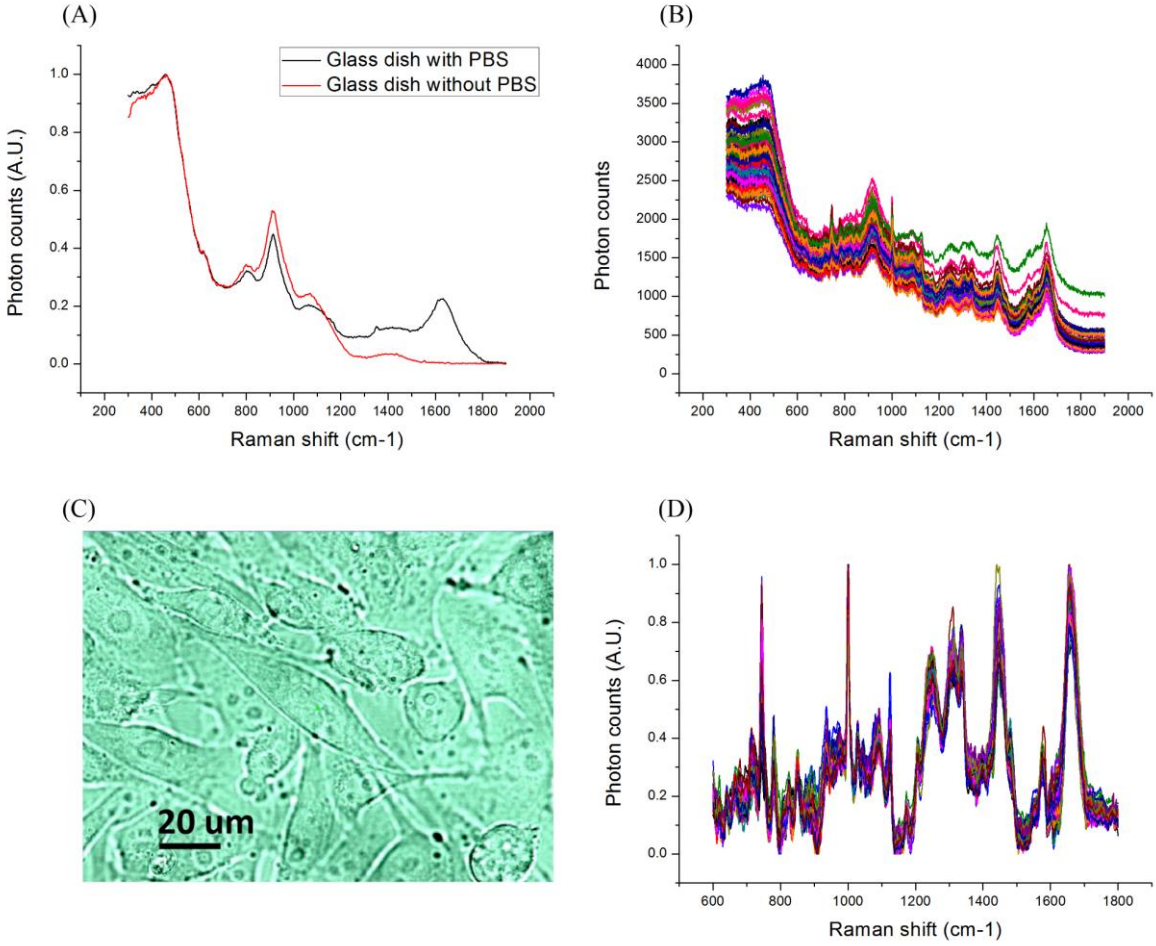

Figure 4.1 A): comparison between the Raman spectra acquired on a glass-bottom dish with and without PBS solution. B): raw Raman spectra acquired from 50 nuclei of SKMEL2 mutated cells. C): wide field epi-illumination images of SKMEL2 mutated cells, obtained with a white-light source. D): Raman spectra of 50 nuclei of SKMEL2 mutated cells obtained by removing glass, PBS background, and fluorescence baseline from the raw acquired data.

Algorithm. As explained in section 2.2.2, the latter is an algorithm for automated fluorescence background removal (though polynomial fitting) from the recorded Raman spectra; in addition, the software allows for smoothing the raw data by applying a Gaussian filter. Figure 4.1D shows the Raman spectra resulting from the whole process; the spectral range was restricted to 600-1800 cm^{-1}, i.e. to the fingerprint region, where all the relevant peaks are.

4.3.2 Cell type classification through PCA

Figure 4.2A shows the mean Raman spectrum of each cell type. As expected from literature [124], these Raman spectra shows very small differences, meaning that most of the recorded

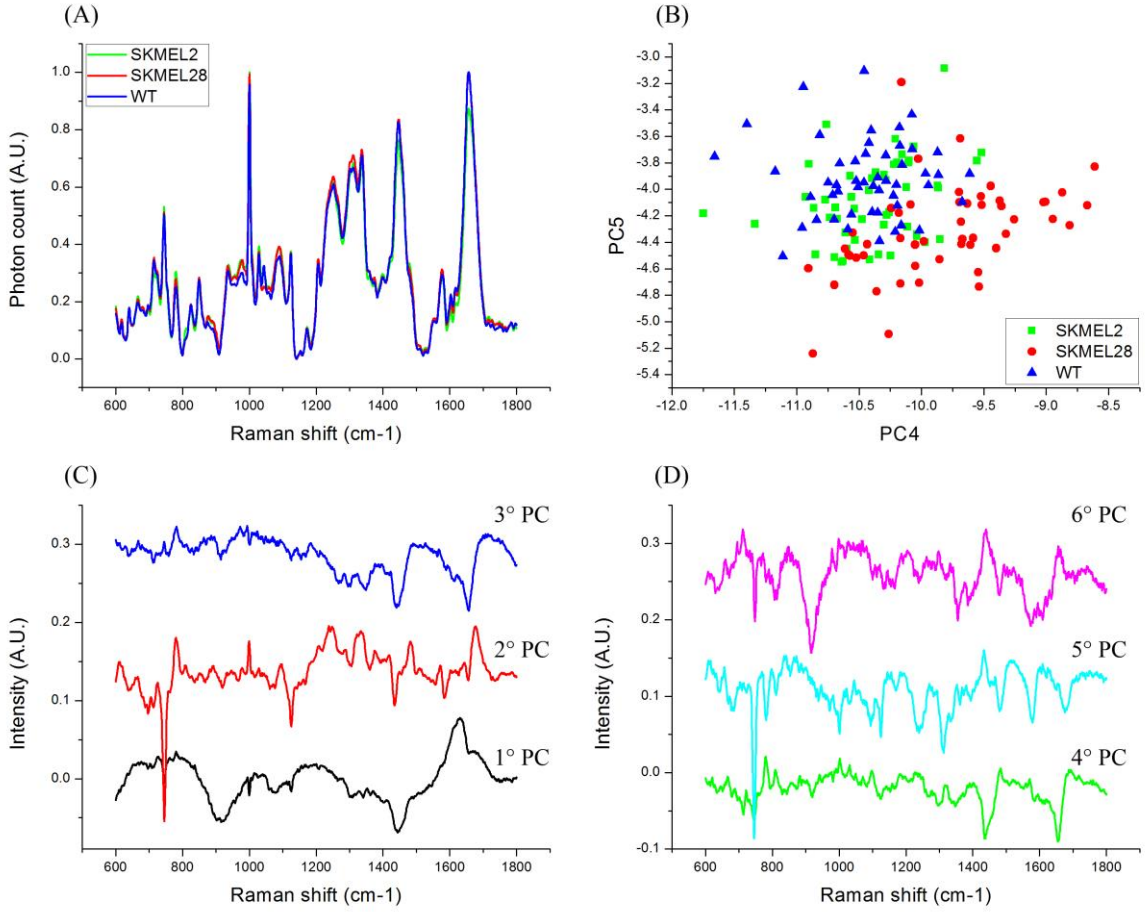

Figure 4.2 A): mean Raman spectra of WT (blue), SKMEL2 (green) and SKMEL28 (red) cell types, each one obtained by averaging 50 recorded spectra. B): scatter plot reporting the PC4 (horizontal axis) and PC5 (vertical axis) coefficients of each recorded spectrum (blue points = WT; green = SKMEL2; red = SKMEL28). C) and D): plotting of the first six PCs. Data are vertically shifted for better visualization.

spectral data is "redundant". Only a small part of the observed spectrum contains the information needed for discriminating tumour cell types. PCA can be used to extract such information from the dataset, consisting of 150 Raman spectra recorded from WT, SKMEL2 and SKMEL28 cells. In fact, as explained in section 2.2.2, the PCA routine calculates the principal components (PCs) of the dataset, which – in this framework – contain the most important spectral features of the recorded Raman spectra (figures 4.2C and D). Usually, the first two or three PCs contain all the relevant information (i.e. the major Raman peaks), while the remaining PCs account only for noise and redundant/unnecessary data. However, since the spectral differences between the three cell types are small, I analysed the first six PCs. Therefore, a recorded spectrum of the dataset can be expressed as a linear combination of

the first six PCs, each one being "weighted" with a certain coefficient (PC1 coefficient, PC2 coefficient, etc). From an algebraic point of view, these coefficients are projections of the

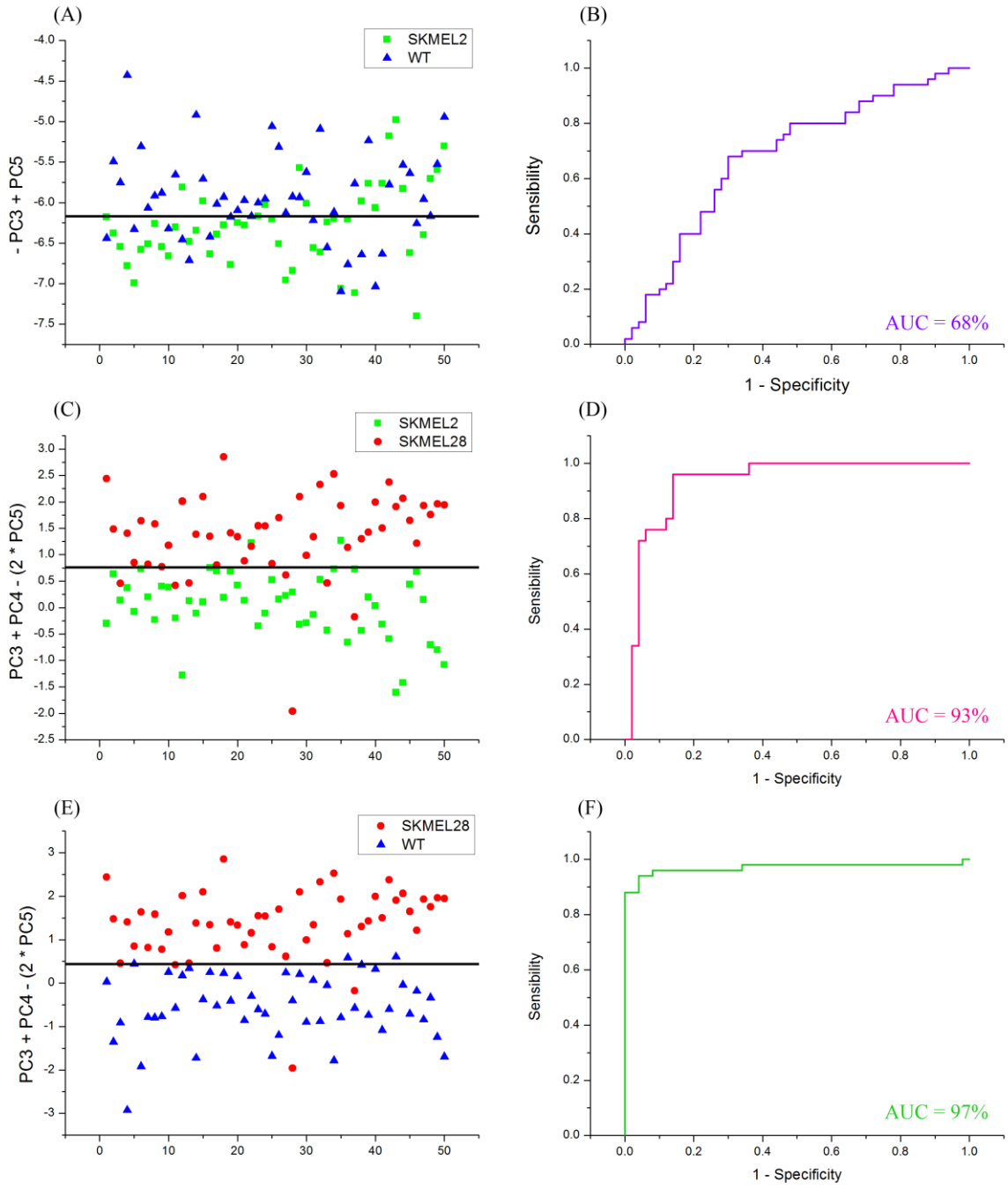

Figure 4.3 Classification of SKMEL2, SKMEL28 and WT spectra through a scoring system based on PCA coefficients. SKMEL2 (green squares), SKMEL28 (red rounds) and WT scores (blue triangles) are calculated with two formulas: (A) PC5 – PC3; (C and E) PC3 + PC4 – (2 × PC5). Each graph shows a threshold (black line) separating the two examined cell types. The ROC curve of each classifier is shown on the right (B, D and F) reporting the corresponding AUC value.

recorded spectrum (which is a 1D vector) along the calculated PCs (which are 1D vectors, too).

PCA coefficients are usually plotted into 2D graphs, like the one shown in figure 4.2B: horizontal and vertical axes report the values of two different coefficients (PC4 and PC5, respectively) and each data point corresponds to one recorded spectrum. Ideally, by plotting the proper PCA coefficients, data points belonging to different classes (i.e. different cell types) should flock into spatially separated "clusters". However, in this case, SKMEL2, SKMEL28 and WT data points cannot be easily separated. Thus, I tested a more complex approach. A score can be assigned to each spectrum by combining its PCA coefficients through simple operations (addition/subtraction). This method aims to find a proper combination that allows discriminating different cell types based on the scores of their spectra. In fact, if a score is above (or below) a certain threshold, the corresponding spectrum is classified into a specific cell type. For example, a classification formula combining PC3 and PC5 was found to differentiate scores belonging to WT and SKMEL2 spectra (figure 4.3A). Moreover, a classifier based on PC3, PC4 and PC5 allowed discriminating SKMEL28 from both SKMEL2 (figure 4.3C) and WT (figure 4.3E) spectra. Figures 4.3B, D and F show the Receiver Operating Characteristic (ROC) of each classifier, whose Area Under the Curve (AUC) measures its classification accuracy. The AUC of the SKMEL2/WT classifier is 68%; for SKMEL28/SKMEL2, it is 93%; for SKMEL28/WT, it is 97%.

The rationale behind this method is that PCs are spectral profiles containing the most relevant Raman peaks of the acquired spectra. By considering only few PCs, redundant and noisy information is discarded from the original dataset. Moreover, a proper combination of the remaining PCs generates a spectral profile that shows only specific Raman peaks. For example, figure 4.4 shows a comparison between SKMEL28 and WT mean Raman spectra and the PCs combination used for discriminating these two cell types. While the three spectral profiles have many peaks in common, there are also significant differences. In fact, the PCs combination contains only the information required for highlighting molecular differences between SKMEL28 and WT: some of their Raman peaks are missing in the PC-derived spectrum because they are not useful for discriminating this two cell types. Finally, the scoring method described in the previous paragraph is equivalent to projecting SKMEL28 and WT Raman spectra along the PC-derived spectral profile – i.e. to simply calculating their scalar products with the latter. In other words, different scores reflect differ-

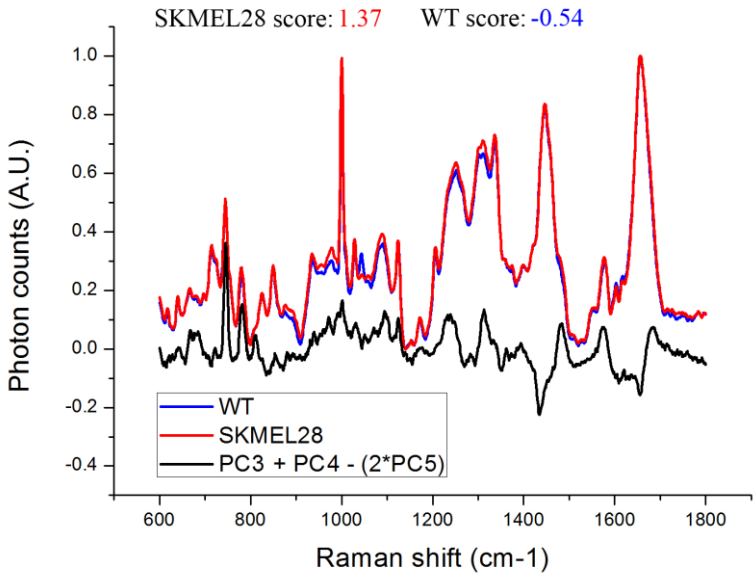

Figure 4.4 Comparison between the mean Raman spectra of SKMEL28 (red) and WT (blue) melanoma cells and the spectral profile obtained by combining the PCs used for the classification formula (black). The scoring system consists in projecting each cell Raman spectrum along the PC-based spectral profile, i.e. by calculating their scalar products. The figure shows the average SKMEL28 and WT scores obtained through the following classifier: PC3 + PC4 – (2 × PC5).

ent intensities of the Raman peaks shown in the PCs combination. Since those peaks are associated to specific molecules, the two cell types can be analysed based on their molecular contents.

The results show that SKMEL28 (i.e. BRAF-mutated cells) Raman spectra can be successfully discriminated from SKMEL2 (NRAS-mutated) and WT (neither BRAF- or NRAS-mutated) spectra by the presented method. Hence, the PCs obtained from the current dataset could be used to classify also newly acquired spectra from unknown melanoma cells. In fact, each new spectrum can be assigned a score through a simple projection along the PC-derived spectral profiles already found in this study; when compared to the corresponding threshold, such number provides an automated classification.

On the other hand, the comparison between SKMEL2 and WT scores provides low classification accuracy (< 70%). Such finding implies either that the molecular differences between these two cell types are very small, or that more PCs should be included in PCA analysis and scoring. In the first case, Raman spectroscopy may not be a reliable tool for discriminating SKMEL2 from WT melanoma cells. In the second case, the problem requires

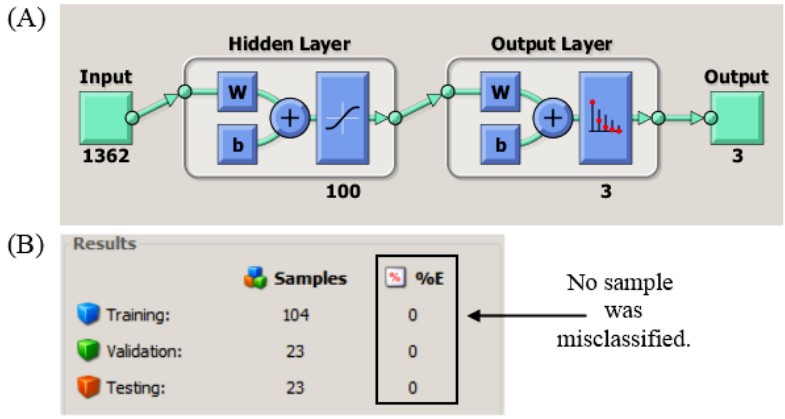

Figure 4.5 A): scheme of the NNPR tool structure. Input data (150 Raman spectra, each one made of 1362 points) are sent to a hidden layer consisting of 100 neurons. Their response function products are sent to an output layer, consisting of 3 neurons, which processes such data and finally produces a 3-digit classification code. Then the software verifies if the latter is correct; otherwise, neuron response functions are modified and the entire process is repeated. B): NNPR results. The percent error (%E) indicates the fraction of samples (i.e. spectra) which are misclassified. A value of 0 means no misclassifications, while 100 indicates maximum misclassifications. In this case, no sample of whatever category (training, validation or testing) was misclassified.

a deeper and/or alternative analysis. For such reason, I tried to classify the same Raman dataset via an Artificial Neural Network (ANN).

4.3.3 Cell type classification through NNPR

As discussed in section 2.2.2, an ANN is a computing system made up of interconnected processing elements (neurons). Neural Network Pattern Recognition (NNPR) is an ANN routine in MATLAB for generating a classification algorithm. The network is instructed via supervised learning to recognize certain features from a dataset of samples and to use them for generating the desired output (i.e. a correct classification of the input data). Using NNPR is very simple and fast. The software automatically creates a 3-layer network (figure 4.5A): an input layer for receiving the samples to be analysed; a hidden layer, whose number of neuron can be selected, for processing the input data; an output layer for generating a classification code. The NNPR tool iterates this process until the classification of all input data cannot be further improved. Moreover, the dataset is divided into three categories:

- training – these samples train the network, which is adjusted according to the errors made in classifying them;

- validation – these samples are used to validate the network, and to halt training when their classification stop improving;
- testing – these samples have no effect on the network training and so provide an independent measure of its performance.

Finally, the NNPR routine compiles a classification algorithm based on the trained network.

Therefore, I loaded 150 Raman spectra (50 for each cell type) and the corresponding classification codes (1-0-0 for SKMEL2, 0-1-0 for SKMEL28, 0-0-1 for WT) into the NNPR tool. 70% (104 spectra) of the dataset was used for training, 15% (23) for validation and the remaining 15% (23) for testing. After setting the hidden layer to have 100 neurons, the output layer generated a 3-digit code for each processed Raman spectrum. As shown in figure 4.5B, all the 150 spectra were successfully classified. Such result suggests that Raman spectroscopy is capable of detecting molecular differences between SKMEL28, SKMEL2 and WT cells. This conclusion seems to be confirmed by the 100% success rate of NNPR in classifying the testing category, which represents exactly an independent test.

However, since the number of sample is quite limited, an additional test was performed in order to further validate this analysis. I ran the network with only 120 Raman spectra ("learning set"), leaving out 10 spectra for each cell type. At the end of the NNPR routine, I tried the resulting classification algorithm on the remaining 30 spectra ("testing set"). Then, four more trials were made by changing every time the spectra used for learning and testing. This approach is similar to the leave-one-out cross-validation (LOOCV) technique, which iteratively leaves one sample out of the training process and uses it as a test for validating the classification accuracy. Table 4.1 reports the success rate of the five trials. On average, the learning set and testing set spectra were classified with 100% and 96% success rate, respectively.

4.4 Conclusions

In this study, I recorded the Raman spectra of three melanoma mutated cell types (SKMEL2, SKMEL28 and WT). I proposed a procedure for removing fluorescence and background signals from the raw acquired data, and then I developed a classification method based on PCA. The three cell types were discriminated though a scoring system, which reflects the intensity of specific Raman shifts. Therefore, Raman spectroscopy proved to be a useful tool

	Learning set (ALL)	Testing set SKMEL2	Testing set SKMEL28	Testing set WT	Testing set (ALL)
Trial n°1	100.0%	100.0%	90.0%	100.0%	96.7%
Trial n°2	100.0%	90.0%	90.0%	90.0%	90.0%
Trial n°3	100.0%	100.0%	100.0%	100.0%	100.0%
Trial n°4	100.0%	90.0%	90.0%	100.0%	93.3%
Trial n°5	100.0%	100.0%	100.0%	100.0%	100.0%
Average	**100.0%**	**96.0%**	**94.0%**	**98.0%**	**96.0%**

Table 4.1 Success rates of the NNPR algorithm in classifying the "learning set" and "testing set" samples (120 and 30 Raman spectra, respectively). The spectra of the two sets were rearranged for five times, as well as the number of classification trials. The success rates of SKMEL2, SKMEL28 and WT spectra from the testing set are reported both separately and aggregated. The bottom row reports the average success rates of the five trials.

for recognition of BRAF and NRAS mutations. Then, in order to improve the classification accuracy, I tried an alternative approach based on a neural network routine. In fact, ANNs have the ability to automatically detect complex nonlinear relationships between variables. Not only the network had succeeded in correctly classifying all the Raman spectra, but also an additional set of trials confirmed the reliability of such outcome.

In conclusion, this study validates the capability of Raman spectroscopy in detecting molecular differences between melanoma cell types. Specific mutations of BRAF and NRAS genes were successfully discriminated, which is a very important clinical datum to be known for properly treating the disease. Therefore, being an optical, label-free and non-destructive technique, Raman spectroscopy provides a fast and effective alternative to the standard methods for classifying mutated melanoma cells.

Chapter 5: Combined two-photon and Raman microscopy

5.1 Introduction

Both TPEF and Raman microscopy proved to be valuable tools for analysing biological samples, as reported in chapter 3 for two-photon imaging of atherosclerotic tissues, and in chapter 4 for the detection of melanoma cell mutations through Raman spectroscopy. However, applying the latter for imaging biological tissues may require a huge amount of time: typical acquisition times for Raman maps can be in the order of ~10 s per point (or longer), resulting in total measurement times in the order of hours or days [127]. An ingenious way to circumvent such problem consists in arranging TPEF and Raman techniques in a complementary approach, capable of providing a fast, label-free and non-invasive alternative to standard histopathological methods. In fact, NLO microscopy can be used for studying tissue morphology and detecting (in a relatively short amount of time) specific regions of interest within very large areas. Then, each one of such regions can be scanned for recording its average Raman spectrum, which provides detailed information about its molecular composition. In this way, the speed of two-photon imaging is integrated with the specificity of Raman spectroscopy. This approach can be applied to the study of a wide variety of tumour or non-tumour diseases. Hence, I applied both TPEF microscopy and Raman spectroscopy (combined in the same custom-made multimodal microscope described in section 2.1.1) to the study of both urothelial carcinoma (UC) and atherosclerosis. In this thesis, thick (bulk) specimens were examined using *en face* optical sectioning geometry for attaining results comparable with potential *in vivo* measurements.

5.1.1 Urothelial carcinoma (UC)

Bladder cancer is a disease involving uncontrolled growth of cells in the urinary bladder: as more of such cells develop, they can form a tumour and spread to other areas of the body [128]. The most common type of bladder cancer is UC, which – depending on its growth pattern – can be classified as papillary or flat. UCs are also divided between invasive and non-invasive, as they can (respectively) grow deep into the bladder wall or they can be limited to the bladder lining. Finally, they are described as high- or low-grade, depending on their degree of architectural and cytological abnormalities [129].

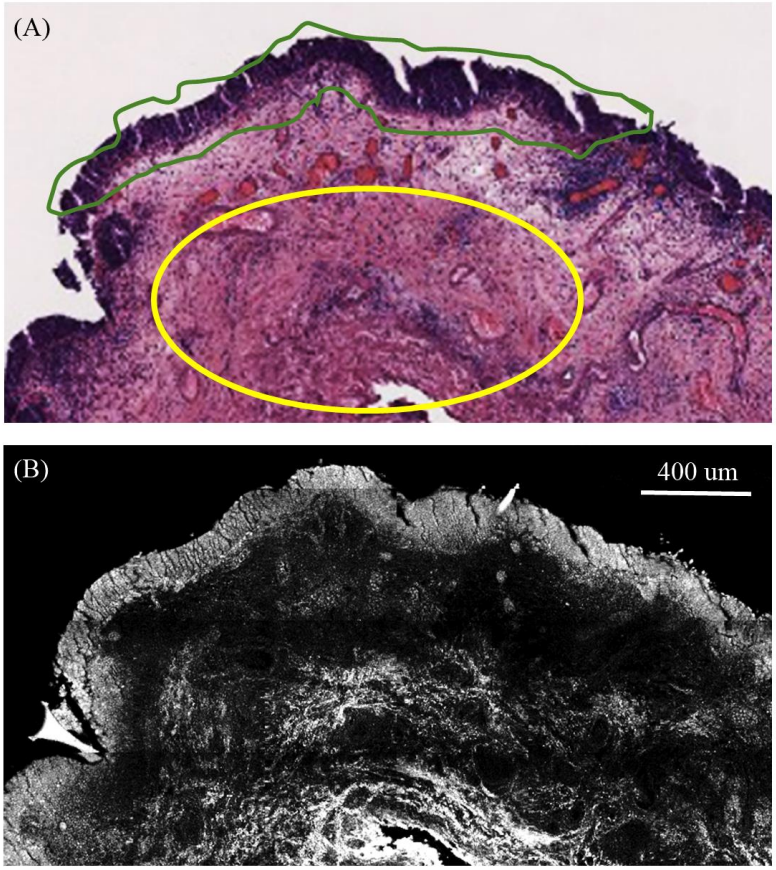

Figure 5.1 Comparison between TPEF mapping of a human bladder specimen affected by UC and its corresponding histopathological result. A): wide-field image of H&E stained slice. Histopathological annotation was done through coloured insets: green for carcinoma in situ, yellow for healthy chorion. B): TPEF mapping obtained by stitching 6 × 4 images. The fluorescence signal was detected in the spectral range 468-552 nm. Each single image was acquired from a formalin-fixed, paraffin-embedded slice with 400 × 400 μm^2 FOV and 512 × 512 pxl^2 resolution, using an excitation wavelength of 740 nm.

Presence, invasiveness and grade of UC are generally diagnosed by histopathological examination, which requires the sampling of several tissue biopsies through a transurethral resection. However, this methodology is highly invasive, and requires a relatively long tissue processing and staining procedure. Moreover, since bladder cancer is characterised by very high recurrence rate [130], its clinical management is very expensive. In this framework, combining NLO microscopy and Raman spectroscopy is a valuable alternative for high-resolution imaging [131] and diagnostics [132] of tissues. In fact – as discussed in the previous chapters – NLO microscopy techniques are useful for investigating tissue morphology (see figure 5.1). In particular, TPEF imaging takes advantage of intrinsic fluorescent molecules (contained both in cells and in the extracellular matrix) such as

NADH, tryptophan, keratins, melanin, elastin, cholecalciferol and others [133], allowing the comparison of cell nuclei dimension between healthy and tumour tissues. On the other hand, the molecular composition of a tissue can be studied in detail through Raman spectroscopy: tumour and healthy cells may be discriminated based on the spectral shape and peaks of their Raman spectra.

5.1.2 Atherosclerosis

Atherosclerosis is a cardiovascular disease in which degenerative material (macrophages, lipids, calcium, fibrous connective tissue, etc) accumulates in the inner layer of the arterial wall. A detailed description of this pathology was given in chapter 3.

NLO microscopy and Raman techniques had been widely used for studying atherosclerotic tissues [100, 105, 134]. SHG, TPEF and CARS microscopy, for example, allowed to image and investigate collagen, cholesterol and, in general, lipid-rich contents [101, 104]. The application of Raman spectroscopy has been proved successful as well [135, 136], since it provides discrimination between normal arterial wall and lipid-rich deposition plaque. Therefore, a combined NLO-Raman microscopic approach has great potential for *in vivo* label-free detection and non-invasive vulnerability assessment of atherosclerotic plaques.

5.2 Materials and methods

5.2.1 Sample preparation

Since the custom-made multimodal microscope can be used for studying both tumour and non-tumour diseases, I applied its capabilities on both UC and atherosclerosis. In fact, with respect to these pathological conditions, two bulk tissue types were investigated: human bladder and rabbit aorta.

Healthy and tumour urothelial tissues were excised through Transurethral Resection of Bladder Tumours (TURBT) surgery from UC patients. I fixed each sample between a microscope slide and a coverslip, both made of quartz (in order to avoid spurious Raman contributions).

Similarly, the atherosclerotic aortas of three New Zealand male, adult white rabbits were excised through surgery. Then, I prepared each specimen in the same way described above.

5.2.2 Data acquisition and processing

The experimental setup used for this study is the custom-made multimodal microscope, whose laser wavelength was set to 785 nm. TPEF images (300 × 300 μm^2 FOV, 512 × 512 pxl^2 resolution, 468-552 nm spectral range) were obtained when the Ti:Sapphire laser was set to pulsed emission. Then, after switching the laser to continuous wave emission, Raman spectra (650-1750 cm^{-1} spectral range, 120 s acquisition time) were recorded by scanning the squared central portion (100 μm size) of each TPEF image. Such procedure was performed on both the human bladder and rabbit aorta examined samples. In particular, 6 combined TPEF-Raman acquisitions were done on healthy bladder, other 6 on diseased bladder, and 6 on diseased aorta.

The recorded Raman spectra were processed through the Vancouver Raman Algorithm software (see section 2.2.2) for separating the Raman signal from the fluorescence emission of the sample. The routine used a 5^{th} order polynomial function in order to fit the fluorescence baseline. Finally, by subtracting the latter from the raw data, I obtained the corresponding Raman spectrum.

5.3 Results and discussion

5.3.1 Combined TPEF-Raman measurements on human bladder

Figure 5.2 reports the TPEF images and mean Raman spectra recorded from normal (i.e. healthy) and tumour urothelial specimens.

Multiphoton imaging can be used for highlighting morphological features in healthy and diseased tissues. For example, as known from literature [137], a tumour cell nucleus is usually bigger than a normal cell nucleus (figures 5.2H-M). Such feature is a key indicator of malignancy, commonly used in standard histopathological examination. Thus, TPEF provides the same information attainable through H&E staining, but in a label-free modality.

Moreover, healthy and diseased Raman spectra show significant differences between their spectral profiles. In particular, UC shows two main peaks around 900 and 1400-1500 cm^{-1}, whereas normal bladder does not. The first band is typically associated with amino acids (such as proline [138]), while the second corresponds to proteins (such as collagen) and lipids [139]. Since UC is characterised by higher levels of amino acids and by an increased

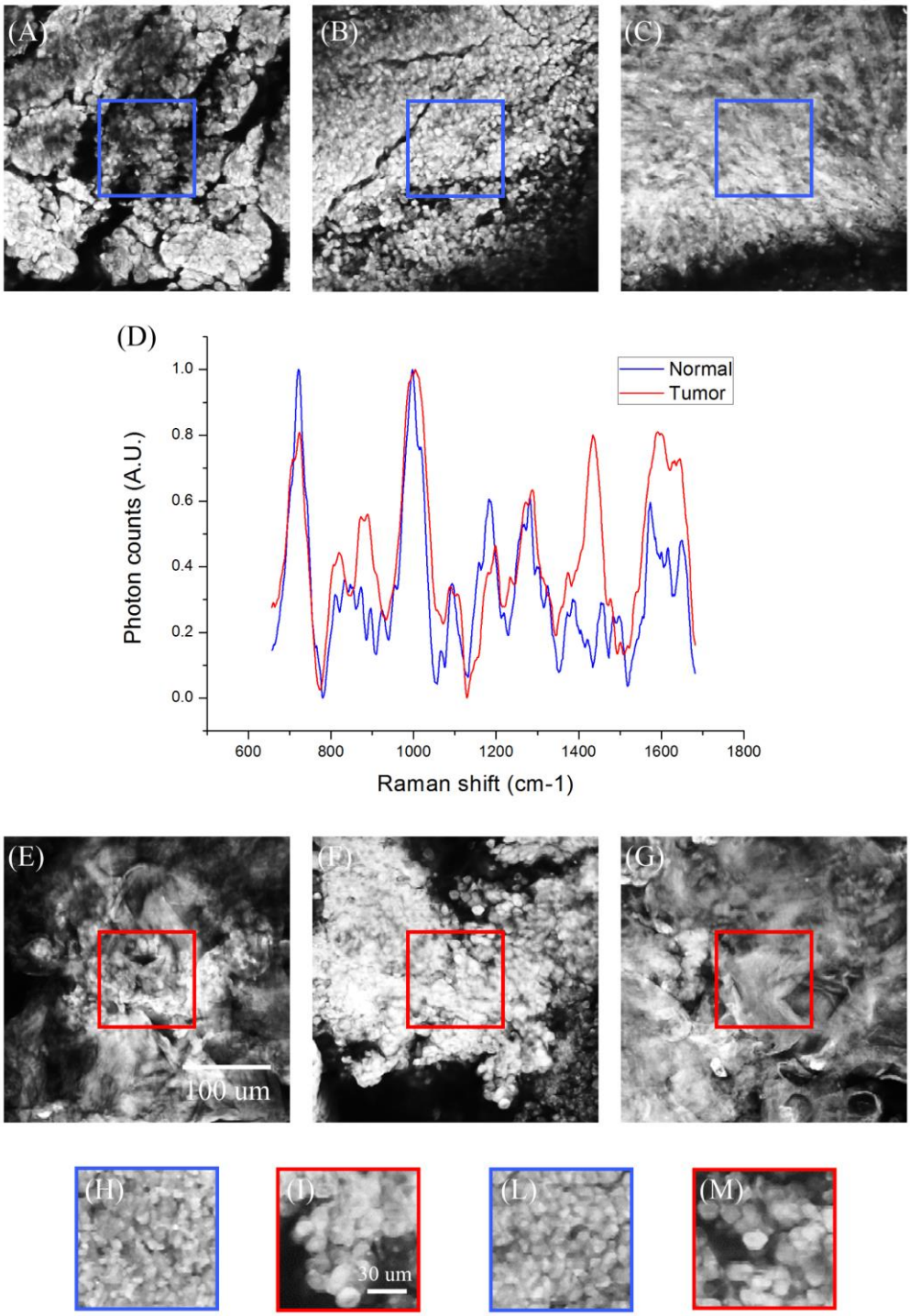

Figure 5.2 A-C) and E-G): TPEF images (300 × 300 μm^2 FOV, 512 × 512 pxl^2 resolution) of healthy and tumour bladder tissues, respectively. D): comparison between the mean Raman spectra recorded from normal (blue line) and diseased (red line) tissues. Each Raman spectrum was obtained by scanning and averaging the signal emitted from the central portion (blue and red squares) of TPEF images. H, L) and I, M): cropped TPEF images (75 × 75 μm^2 FOV, 128 × 128 pxl^2 resolution) of normal and tumour cells in urothelial tissues, respectively.

production in the majority of lipid classes [140], the peaks observed in the tumour spectrum may reflect the altered metabolism of bladder cancer. Detecting changes in the products of metabolic activity by using an optical tool such as Raman spectroscopy could be a huge improvement with respect to other methods, like mass spectrometry (MS) and immunohistochemistry (IHC). All these techniques provide molecular characterisation of the examined tissues; however, the MS procedure destroys the sample, while IHC has many limitations. In fact, IHC requires the use of specific markers, and hence tissue fixation and processing; moreover, there are significant bias related to execution and results interpretation. In contrast, Raman spectroscopy does not affect the specimen, is label-free and its results can be obtained through automated data processing.

5.3.2 Combined TPEF-Raman measurements on rabbit aorta

Figure 5.3 reports the TPEF images and mean Raman spectra recorded from bulk atherosclerotic tissues. Since the internal layer (tunica intima) of each artery was fully covered by thick lipid deposition, it was not possible to image the underlying arterial wall with *en face* optical section geometry. Thus, comparing healthy and diseased arterial tissues required a cross-section imaging geometry (see below).

TPEF microscopy takes advantage of the presence of intrinsic fluorophores such as lipids (e.g. cholesterol) and elastic fibres (collagen, elastin) within the sample. Therefore, it can be used for imaging both atherosclerotic plaques and arterial walls: the former are lipid-rich depositions, while the latter consist mainly of collagen fibres. These tissues have very different morphological features: the plaque is characterised by isotropic distribution of lipid clusters (figure 5.3A-C and E-G), while the arterial wall shows a bundle of collagen and elastic fibres aligned in the same direction. As demonstrated in a previous study [109], GLCM correlation and FFT analysis are valuable tools for discriminating the deposition from the wall. In fact, the correlation length measures the typical size of lipid clusters and the diameter of collagen fibres, while the aspect ratio analyses the anisotropy level of organized fibres and disorganized lipid formations.

The Raman spectrum of lipid deposition shows many peaks (figure 5.3D) and the most intense Raman band (1400-1500 cm^{-1}) corresponds to the presence of cholesterol [141]. This result can be compared to previous Raman measurements performed on a thin cross-section of rabbit aorta (figure 5.4A). In fact, a thin slice of aorta was placed on a microscope quartz

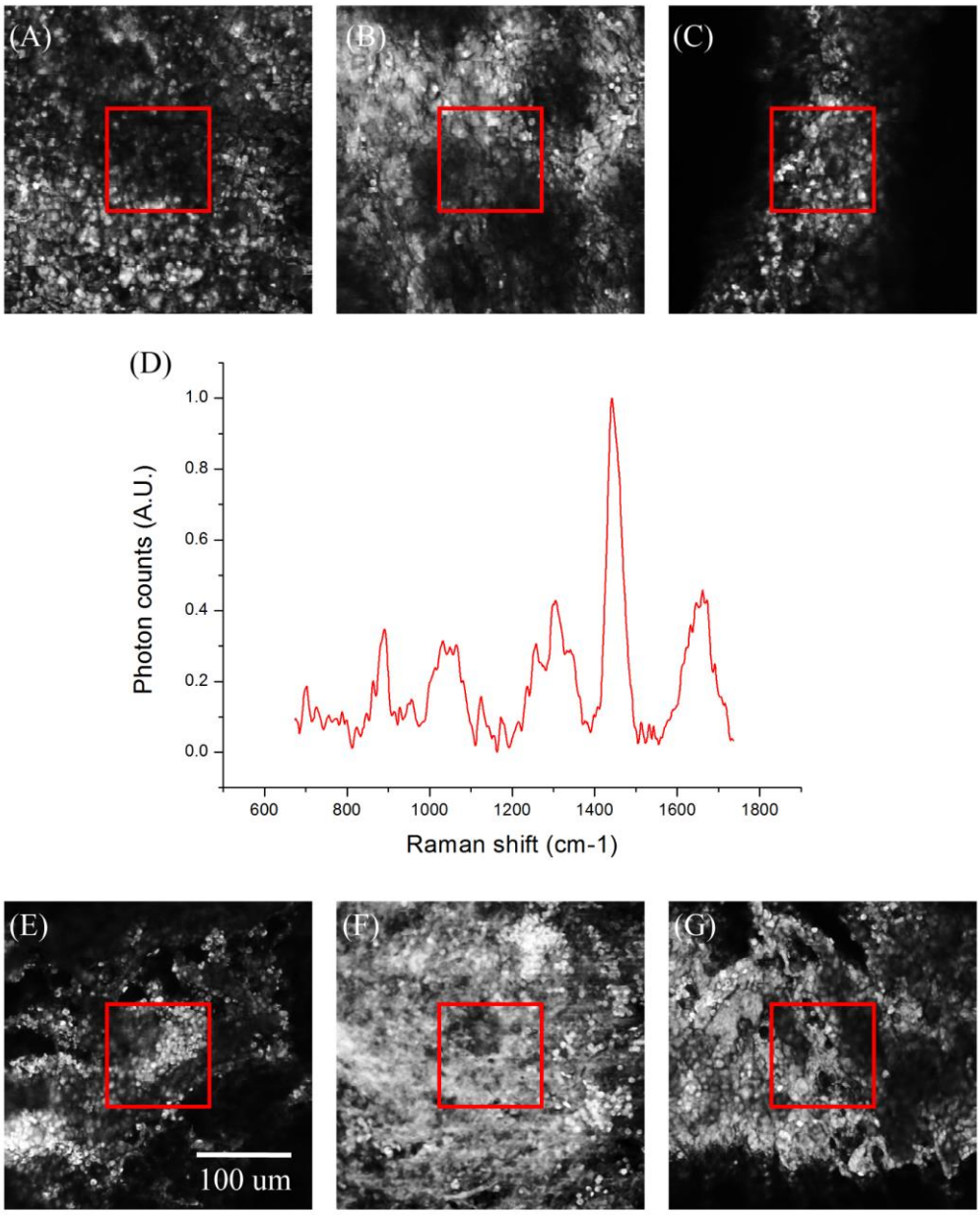

Figure 5.3 A-C) and E-G): TPEF images (300 × 300 μm^2 FOV, 512 × 512 pxl^2 resolution) recorded from atherosclerotic plaques of rabbit aorta. D): mean Raman spectrum recorded from lipid depositions and obtained by scanning and averaging the signal emitted from the central portion (red squares) of TPEF images.

slide for observation with cross-section geometry – which is typically adopted in histopathological examination. Then, I used the XploRA INV (Horiba, Kyoto, Japan) commercial microscope for recording the Raman spectra of normal arterial wall and lipid deposition regions (figure 5.4B) within the examined slice. I found that lipid deposition spectra recorded from both bulk and thin tissue samples are consistent and well correlated.

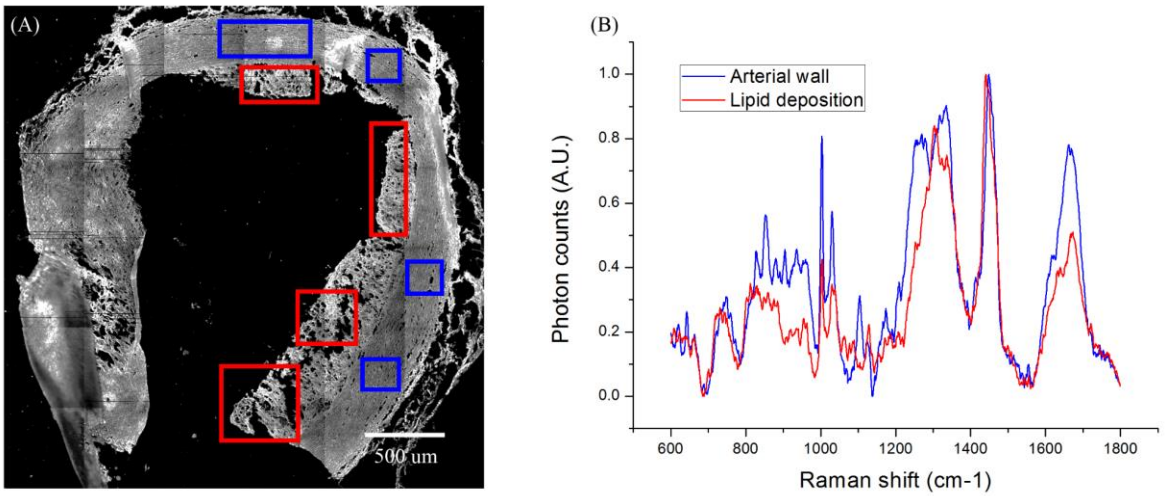

Figure 5.4 A): TPEF mapping (6 × 6 images, each one acquired with 500 × 500 μm^2 FOV and 512 × 512 pxl^2 resolution) of rabbit aorta cross-section. Coloured insets indicate arterial wall (blue) and lipid deposition (red) regions. B): mean Raman spectra recorded from arterial wall (blue) and lipid depositions (red) regions of rabbit aorta.

Moreover, strong spectral differences can be observed between the arterial wall and the atherosclerotic plaque. In particular, the recorded spectra have very different profiles around 1250 cm^{-1}: the arterial wall shows a peak associated with collagen [142], while the lipid deposition does not. In this regard, it is interesting to note that the bulk sample spectrum in figure 5.3D shows a small peak at the same Raman shift. In fact, non-descanning detection excludes the possibility of using a pinhole for removing out-of-focus photons. Therefore, the Raman signal generated from the sample is detected not only from the focal plane (i.e. from the plaque superficial layer imaged in figure 5.3), but also from deeper layers – such as the underlying arterial wall. Thus, the latter may give a contribution to the recorded Raman spectrum. These results could provide important insights for potential *in vivo* applications. The ratio between the Raman intensity at 1450 cm^{-1} (corresponding to both collagen and cholesterol contents) and the intensity at 1250 cm^{-1} (collagen) could indicate the presence of a plaque. Moreover, the lipid-to-collagen ratio being correlated to plaque stability [115], this approach based on Raman spectroscopy could be used for vulnerability assessment.

5.4 Conclusions

I used a custom-made multimodal microscope that combines two-photon imaging and Raman spectroscopy for studying and characterising both tumour and non-tumour diseases.

These techniques proved to be fast, label-free and non-invasive optical tools for analysing morphology and molecular composition of biological tissues.

I found that TPEF allows discriminating between healthy and tumour urothelial tissues based on nuclear size, in a good agreement with corresponding histopathological examination. Moreover, Raman spectra of UC shows an increased presence of lipids and amino acids with respect to normal bladder, reflecting an altered metabolism of the tumour with respect to the healthy tissue.

Similarly, combined TPEF-Raman microscopy was used for imaging atherosclerotic tissues and investigating their composition. In fact, significant morphological differences can be highlighted through multiphoton microscopy: normal arterial wall is characterised by well-aligned collagen fibres, while plaque deposition shows a "grainy" pattern consisting mainly of lipids. Differences between the two tissue types were observed also from the molecular point of view using Raman spectroscopy: the Raman bands of lipids and collagen can be easily identified, and their intensity ratio may be a valuable tool for assessing the severity of atherosclerosis.

Therefore, combined two-photon and Raman microscopy provides a powerful alternative to standard histopathological methods. TPEF imaging allows fast detection of sensible (e.g. diseased) areas within the examined specimen, while Raman spectroscopy can be used for diagnosing them with high sensitivity and specificity. Moreover, by examining bulk samples with *en face* geometry, the presented results are comparable with potential *in vivo* measurements, paving the way for a non-invasive detection of the studied diseases.

Chapter 6: Conclusions

Combined FLIM, TPEF and SHG microscopy was used for characterising human carotid *ex vivo* specimens affected by atherosclerosis. This approach provided high-contrast images comparable with histopathological examination, highlighting many and useful morphological and physiological features for assessing plaque vulnerability. In fact, TPEF and SHG allowed evaluating the organisation and size of calcium/lipids agglomerates and collagen fibres within different atherosclerotic tissues, paving the way for discriminating different atherosclerotic tissues through a classification algorithm based on such features. This approach allowed not only the detection of fibrous cap regions, but also the discrimination of necrotic, calcified and inflammatory tissues within plaque depositions. FLIM imaging added further and complementary information by examining differences in fluorescence lifetime of the examined tissues, due to their environment and molecular composition. Thus, all tissue types were discriminated based on their averaged fluorescence lifetime parameters. Therefore, the presented method provides a faster and label-free alternative to the standard histopathological techniques commonly applied for the examination of tissue biopsies.

In another study, Raman spectroscopy was used for *in vitro* discrimination of melanoma mutated cell types. Since the medical treatment of MM targets the specific mutation involved in the carcinogenesis, this research aimed to provide an additional tool for clinical routine. The analysis of the recorded Raman spectra required removing fluorescence and background signals from the raw data, and then applying two high-level classification methods for differentiating MM mutations. This approach resulted in high-performing classification accuracy. This study, by successfully discriminating MM mutations through optical probing, without any labelling procedure, proved the potential benefits of applying Raman spectroscopy for clinical detection of tumour diseases. In fact, the results obtainable with such methodology could assist the clinicians in choosing a proper therapy for their patients.

Finally, combined two-photon imaging and Raman spectroscopy were used for studying and characterising both human bladder affected by UC and atherosclerotic aorta obtained from an animal model. These bulk samples were examined with *en face* optical geometry in order to produce results comparable with potential *in vivo* measurements. Arranging these techniques in a complementary approach combines the fast imaging capability of NLO with

the high-specificity of Raman spectroscopy, providing a thorough tool for analysing both morphology and molecular composition of biological tissues. In fact, TPEF allowed discriminating between healthy and tumour urothelial tissues based on nuclear size – in a good agreement with corresponding histopathological examination – while Raman spectroscopy revealed the altered metabolism of UC (in terms of increased production of lipids and amino acids) with respect to normal bladder. These features are extremely important for early detection of the tumour; moreover, the measurements performed for observing them could be done *in vivo*. Similarly, combined TPEF-Raman microscopy was used for imaging atherosclerotic tissues excised from rabbit aorta, and investigating their composition. In fact, multiphoton microscopy highlighted strong morphological differences between the normal arterial wall and the plaque deposition. Raman spectroscopy provided a stark contrast as well by reflecting mainly the collagen and lipid contents that differentiate these tissues. Thus, the presented results could help detecting atherosclerotic plaques at early stages. Moreover, the Raman bands of lipids and collagen can be used for evaluating their relative abundancies within the examined region, which could be a relevant datum for assessing the severity of atherosclerosis and urging the surgery of vulnerable plaques.

In conclusion, combined NLO-Raman microscopy proved to be not only a fast, label-free and non-invasive alternative to standard histopathological methods, but also a powerful tool for clinical diagnosis – with potential life-saving and cost-effective applications. Also, this approach could be further improved by adding other techniques (see chapter 7) for obtaining additional morpho-functional information. In fact, improving the capabilities of multimodal microscopes with respect to their clinical application will be a driving factor for future ability of early disease detection and treatment, with large and positive impacts on our society.

Chapter 7: Future perspectives

The presented study shows the successful application of multimodal microscopy to different clinical problems but, more importantly, it opens the door to a great number of exciting and diversified developments in the near future.

The custom-made multimodal microscope can be easily adapted for new purposes. For example, simply adding a motorised polarising filter before the excitation objective would allow polarisation-resolved measurements of SHG signal. Also, by using resonant scan mirrors or acousto-optic modulators for laser beam deflection, both scan accuracy and imaging speed would increase. A major improvement could be provided by substituting the excitation source with an ultrafast, broadly tunable laser with phase-locked dual output: this step would allow the implementation of additional techniques – such as CARS, THG and SRS – for providing other fast, high-resolution and label-free contrast mechanisms.

Thus, the spectrum of possible applications could increase dramatically. There are many tissues and diseases, involving alterations in collagen or myelinated fibres and lipid-rich structures, that can be studied though the above-mentioned techniques: cornea (keratoconus), brain (focal cortical dysplasia), blood cells (malaria), peripheral nervous system (lipidosis, diabetes), etc. Moreover, FLIM, TPEF and SHG could be used for investigating other *ex vivo* specimens (such as melanocytic lesions and breast cancer) as well as for *in vivo* monitoring of the metabolism of standard animal models (mouse, zebrafish).

There is room to improve data analysis, too. For instance – as shown in chapter 3 – multiphoton imaging can measure many parameters for each point of the examined area: TPEF/SHG and SHG F/B ratios, lifetime parameters, GLCM correlation length, etc. PCA could be used for analysing the whole set of these variables, discarding noise and redundant information, and then discriminating different tissues. Moreover, well-known methods such as Multivariate Curve Resolution (MCR) and Partial Least Square Discriminant Analysis (PLS-DA) could be applied to spectral analysis. MCR is able to recognise the molecular constituents that contribute to recorded Raman spectra, while PLS-DA is commonly used for discriminating different categories. These methods could help interpreting tissue composition as well as providing their classification based on spectral information.

Therefore, there is still a lot to be done in the following years for exploiting all the opportunities given by multimodal microscopy, and for exploring all its possible applications. In addition, the current development of multiphoton endoscopes is opening the way for clinical diagnosis and monitoring of a wide range of diseases though NLO microscopy – a step that could result in a relevant advance in photonics technology for medical diagnostics.

References

[1] "*Nonlinear optics - Chapter 5*", retrieved from the website of Springer: https://www.springer.com/

[2] J. Mertz, "*Nonlinear microscopy: new techniques and applications*", Current Opinion in Neurobiology **14**(5), 610-616 (2004).

[3] P.T.C. So, C.Y. Dong, B.R. Masters, K.M. Berland, "*Two-Photon Excitation Fluorescence Microscopy*", Annual Review of Biomedical Engineering **2**, 399-429 (2000).

[4] Retrieved from the website of the David Kleinfeld Laboratory: https://physics.ucsd.edu/neurophysics/courses/physics_173_273/Nonlinear_optics.pdf

[5] D. Yelin, Y. Silberberg, "*Laser scanning third-harmonic-generation microscopy in biology*", Optics Express **5**(8), 169-175 (1999).

[6] C.L. Evans, X.S. Xie, "*Coherent Anti-Stokes Raman Scattering Microscopy: Chemical Imaging for Biology and Medicine*", Annual Review of Analytical Chemistry **1**, 883-909 (2008).

[7] L. de Vivo, S. Landi, M. Panniello, L. Baroncelli, S. Chierzi, L. Mariotti, M. Spolidoro, T. Pizzorusso, L. Maffei, G.M. Ratto, "*Extracellular matrix inhibits structural and functional plasticity of dendritic spines in the adult visual cortex*", Nature Communications **4**, 1484 (2013).

[8] S.L. Jacques, "*Optical properties of biological tissues: a review*", Physics in Medicine & Biology **58**(11), R37-61 (2013).

[9] V.V. Tuchin, "*Polarized light interaction with tissues*", Journal of Biomedical Optics **21**(7), 071114 (2016).

[10] M. Goeppert-Mayer, "*Uber elementarekte mit zwei Quantensprunger*", Annales de Physique **9**(401), 273-294 (1931).

[11] W. Kaiser, C.G.B. Garrett, "*Two-photon excitation in $CaF_2:Eu^{2+}$*", Physical Review Letters **7**(6), 229-231 (1961).

[12] W. Denk, H.J. Strickler, W.W. Webb, "*Two-photon laser scanning fluorescence microscopy*", Science **248**(4951), 73-76 (1990).

[13] W.R. Zipfel, R.M. Williams, W.W. Webb, "*Nonlinear magic: multiphoton microscopy in the biosciences*", Nature Biotechnology **21**, 1369-1377 (2003).

[14] O. Nakamura, "*Fundamental of two-photon microscopy*", Microscopy Research and Technique **47**(3), 165-171 (1999).

[15] C.J.R. Sheppard, M. Gu, "*Image formation in two-photon fluorescence microscopy*", Optik **86**(3), 104-106 (1990).

[16] R. Hellwarth, P. Christensen, "*Nonlinear optical microscopic examination of structure in polycristalline ZnSe*", Optics Communications **12**(3), 318-322 (1974).

[17] C.J.R. Sheppard, R. Kompfner,, J. Gennaway, D. Walsh, "*The Scanning Harmonic Optical Microscope*", IEEE Journal of Quantum Electronics **13**(9), 100D (1977).

[18] J.N. Gannaway, C.J.R. Sheppard, "*Second-harmonic imaging in the scanning optical microscope*", Optical and Quantum Electronics **10**, 435-439 (1978).

[19] P.J. Campagnola, M. Wei, A. Lewis, L.M. Loew, "*High-resolution nonlinear optical imaging of live cells by second harmonic generation*", Biophysical Journal **77**(6), 3341-3349 (1999).

[20] L. Moreaux, O. Sandre, J. Mertz, "*Membrane imaging by second-harmonic generation microscopy*", Journal of the Optical Society of America B **17**(10), 1685-1694 (2000).

[21] Y. Guo, P.P. Ho, H. Savage, D. Harris, P. Sacks, S. Schantz, F. Liu, N. Zhadin, R.R. Alfano, "*Second-harmonic tomography of tissues*", Optics Letters **22**(17), 1323-1325 (1997).

[22] R.M. Williams, W.R. Zipfel, W.W. Webb, "*Interpreting second-harmonic generation images of collagen I fibrils*", Biophysical Journal **88**(2), 1377-1386 (2005).

[23] C. Xu, W.W. Webb, "*Measurement of two-photon excitation cross section of molecular fluorophores with data from 690 nm to 1050 nm*", Journal of the Optical Society of America B **13**(3), 481-491 (1996).

[24] M. Born, E. Wolf, "*Principles of optics*", Pergamon Press: Oxford, UK (1993).

[25] R. Cicchi, N. Vogler, D. Kapsokalyvas, B. Dietzek, J. Popp, F.S. Pavone, "*From molecular structure to tissue architecture: collagen organization probed by SHG microscopy*", Journal of Biophotonics **6**(2), 129-142 (2013).

[26] M.J. Buehler, "*Nature designs tough collagen: Explaining the nanostructure of collagen fibrils*", Proceedings of the National Academy of Sciences of the United States of America **103**(33), 12285-12290 (2006).

[27] M. Lombardo, D. Merino, P. Loza-Alvarez, G. Lombardo, "*Translational label-free nonlinear imaging biomarkers to classify the human corneal microstructure*", Biomedical Optics Express **6**(8), 2803-2818 (2015).

[28] R. Cicchi, "*Non-linear laser imaging of human skin*", Faculty of Mathematical, Physical and Natural Sciences – University of Florence, Italy (2006-2007).

[29] W.R. Zipfel, R.M. Williams, R. Christie, A.Y. Nikitin, B.T. Hyman, W.W. Webb, "*Live tissue intrinsic emission microscopy using multiphoton-excited native fluorescence and second harmonic generation*", Proceedings of the National Academy of Sciences of the United States of America **100**(12), 7075-80 (2003).

[30] E.P. Diamandis, "*Immunoassays with time-resolved fluorescence spectroscopy: principles and applications*", Clinical Biochemistry **21**(3), 139-50 (1988).

[31] G.A. Elöve, A.F. Chaffotte, H. Roder, M.E. Goldberg, "*Early steps in cytochrome c folding probed by timeresolved circular dichroism and fluorescence spectroscopy*", Biochemistry **31**(30), 6876–6883 (1992).

[32] J.R. Lakowicz, H. Szmacinski, K. Novaczyk, K.W. Berndt, M. Johnson, "*Fluorescence lifetime imaging*", Analytical Biochemistry **202**(2), 316-330 (1992).

[33] J.R. Lakowicz, K.W. Berndt, "*Lifetime-selective fluorescence imaging using an rf phase sensitive camera*", Review of Scientific Instruments **62**(7), 1727-1734 (1991).

[34] R. Sanders, A. Draaijer, H.C. Gerritsen, P.M. Houpt, Y.K. Levine, "*Quantitative pH imaging in cells using confocal fluorescence lifetime imaging microscopy*", Analytical Biochemistry **227**(2), 302-308 (1995).

[35] T. French, P.T.C. So, D.J. Weaver Jr, T. Coelho-Sampaio, E. Gratton, E.W. Voss Jr, J. Carrero, "*Two-photon fluorescence lifetime imaging microscopy of macrophage-mediated antigen processing*", Journal of Microscopy **185**(3), 339-353 (1997).

[36] I. Rocha-Mendoza, J. Licea-Rodriguez, M. Marro, O.E. Olarte, M. Plata-Sanchez, P. Loza-Alvarez, "*Rapid spontaneous Raman light sheet microscopy using cw-lasers and tunable filters*", Biomedical Optics Express **6**(9), 3449-3461 (2015).

[37] W. Demtröder, "*Atoms, Molecules and Photons – An Introduction to Atomic-, Molecular- and Quantum Physics*", Springer: Berlin/Heidelberg, Germany (2010).

[38] "*The Born-Oppenheimer Approximation*", retrieved from the website of New York University (USA): https://www.nyu.edu/classes/tuckerman/quant.mech/lectures/lecture_10/node1.html

[39] "*Morse potential*", retrieved from the website of Wikipedia: https://en.wikipedia.org/wiki/Morse_potential

[40] H.A. Szymanski, "*Raman spectroscopy - Theory and practice*", Plenum Press: New York, USA (1967).

[41] Retrieved from the following website: http://www.raman.de/

[42] Katherine J.I. Ember, M.A. Hoeve, S.L. McAughtrie, M.S. Bergholt, B.J. Dwyer, M.M. Stevens, K. Faulds, S.J. Forbes, C.J. Campbell, "*Raman spectroscopy and regenerative medicine: a review*", npj Regenerative Medicine **2**(12), 1-10 (2017).

[43] G. Placzek, "*Rayleigh–Streuung und Raman-Effekt*" in: E.A. Marx, "*Handbuch der Radiologie*" Acadeische-Verlag **6**, 205 (1934).

[44] L. Pauling, E.B. Wilson, "*Introduction to Quantum Mechanics*", McGraw-Hill: New York, USA (1935).

[45] J. Zhao, H. Lui, D.I. McLean, H. Zeng, "*Real–Time Raman Spectroscopy for non-invasive skin cancer detection - preliminary results*", 30th Annual International IEEE EMBS Conference in Vancouver, British Columbia, Canada (2008).

[46] R. Cicchi, A. Cosci, S. Rossari, D. Kapsokalyvas, E. Baria, V. Maio, D. Massi, V. De Giorgi, N. Pimpinelli, F.S. Pavone, "*Combined fluorescence-Raman spectroscopic setup for the diagnosis of melanocytic lesions*", Journal of Biophotonics **7**(1-2), 86-95 (2014).

[47] M.G. Shim, L.M.W.K. Song, N.E. Marcon, B.C. Wilson, "*In vivo near-infrared Raman spectroscopy: demonstration of feasibility during clinical gastrointestinal endoscopy*" Photochemistry and Photobiology **72**(1), 146-150 (2000).

[48] V.S. Hanchanale, R.R. Amrith, S. Das, "*Raman spectroscopy and its urological applications*", Indian Journal of Urology **24**(4), 444-450 (2008).

[49] J.P. Salenius, J.F. Brennan 3rd, A. Miller, Y. Wang, T. Aretz, B. Sacks, R.R. Dasari, M.S. Feld, "*Biochemical composition of human peripheral arteries examined with near-infrared Raman spectroscopy*", Journal of vascular surgery **27**(4), 710-719 (1998).

[50] R. Smith, K.L. Wright, L. Ashton, "*Raman spectroscopy: an evolving technique for live cell studies*", Analyst **141**, 3590-3600 (2016).

[51] C. Matthäus, B. Bird, M. Miljković, T. Chernenko, M. Romeo, M. Diem, "*Infrared and Raman Microscopy in Cell Biology*", Methods in Cell Biology **89**, 275-308 (2008).

[52] G. Clemens, J.R. Hands, K.M. Dorlingab, M.J. Baker, "*Vibrational spectroscopic methods for cytology and cellular research*", Analyst **139**, 4411-4444 (2014).

[53] I.W. Schie, C. Krafft, J. Popp, "*Cell classification with low-resolution Raman spectroscopy (LRRS)*", Journal of Biophotonics **9**(10), 994-1000 (2016).

[54] I. Pence, A. Mahadevan-Jansen, "*Clinical instrumentation and applications of Raman spectroscopy*", Chemical Society Reviews **45**(7), 1958-1979 (2016).

[55] J. Zhao, H. Lui, D.I. McLean, H. Zeng, "*Automated Autofluorescence Background Subtraction Algorithm for Biomedical Raman Spectroscopy*", Applied Spectroscopy **61**(11), 1225-1232 (2007).

[56] J.T. Motz, M. Hunter, L.H. Galindo, J.A. Gardecki, J.R. Kramer, R.R. Dasari, M.S. Feld, "*Optical fiber probe for biomedical Raman spectroscopy*", Applied Optics **43**, 542-554 (2004).

[57] D. Tuschel, "*Selecting an Excitation Wavelength for Raman Spectroscopy*", Spectroscopy **31**(3), 14-23 (2016).

[58] T.F. Budinger, "*Resonance Raman Scattering*", Volume 1 – Nuclear Medicine and Molecular Imaging, in: A. Brahme, "*Comprehensive biomedical physics*", Elsevier: Amsterdam, Netherlands (2014).

[59] G. Stock, W. Domcke, "*Theory of resonance Raman scattering and fluorescence from strongly vibronically coupled excited states of polyatomic molecule*", The Journal of Chemical Physics **93**, 5496-5509 (1990).

[60] A.N. Kuzmin, A. Pliss, C.K. Lim, J. Heo, S. Kim, A. Rzhevskii, B. Gu, K.T. Yong, S. Wen, P.N. Prasad, "*Resonance Raman Probes for Organelle-Specific Labeling in Live Cells*", Scientific Reports **6**, 28483 (2016).

[61] M. Harz, P. Rösch, J. Popp, "*Raman Investigation of Microorganisms on a Single Cell Level*", Application Notes **RA59**, Horiba.

[62] J. Jehličkaa, H.G.M. Edwardsa, A. Orenc, "*Raman Spectroscopy of Microbial Pigments*", Applied Environmental Microbiology **80**(11), 3286-3295 (2014).

[63] A.C.S. Talari, Z. Movasaghi, S. Rehman, I. ur Rehman, "*Raman Spectroscopy of Biological Tissues*", Applied Spectroscopy Reviews **50**(1), 46-111 (2014).

[64] See the website of Autodesk: https://www.autodesk.com/products/inventor/overview

[65] See the website of the US National Institute of Health: https://imagej.nih.gov/ij/

[66] See the website of the Physical Measurement Laboratory (National Institute of Standards and Technology, USA): https://physics.nist.gov/PhysRefData/Handbook/Tables/neontable2.htm

[67] See the website of the McCreary research group (National Institute for Nanotechnology, University of Alberta, Canada): http://www.chem.ualberta.ca/~mccreery/ramanmaterials.html

[68] C. Van Loan, "*Computational frameworks for the fast Fourier transform*", Society for Industrial and Applied Mathematics: Philadelphia, USA (1992).

[69] R. Cicchi, D. Kapsokalyvas, V. De Giorgi, V. Maio, A. Van Wiechen, D. Massi, T. Lotti, F.S. Pavone, "*Scoring of collagen organization in healthy and diseased human dermis by multiphoton microscopy*", Journal of Biophotonics **3**(1-2), 34-43 (2010).

[70] Retrieved from the Mryka Hall-Beyer's website: http://www.fp.ucalgary.ca/mhallbey/the_glcm.htm

[71] Z. Huang, A. McWilliams, H. Lui, D.I. McLean, S. Lam, H. Zeng, "*Near–infrared Raman spectroscopy for optical diagnosis of lung cancer*", International Journal of Cancer **107**(6), 1047-1052 (2003).

[72] J. Zhao, H. Lui, D.I. McLean, H. Zeng, "*Real-Time Raman Spectroscopy for Noninvasive in vivo Skin Analysis and Diagnosis*", in: D. Campolo, "*New Developments in Biomedical Engineering*", InTech: Rijeka, Croatia (2010).

[73] M. Mazilu, A.C. De Luca, A. Riches, C.S. Herrington, K. Dholakia, "*Optimal algorithm for fluorescence suppression of modulated Raman spectroscopy*", Optics Express **18**(11), 11382-11395 (2010).

[74] A.C. De Luca, M. Mazilu, A. Riches, C.S. Herrington, K. Dholakia, "*Online Fluorescence Suppression in Modulated Raman Spectroscopy*", Analytical Chemistry **82**(2), 738-745 (2010).

[75] L.I. Smith, "*A tutorial on Principal Components Analysis*", (2002). See here: http://www.cs.otago.ac.nz/cosc453/student_tutorials/principal_components.pdf

[76] J. Schlens, "*A Tutorial on Principal Component Analysis*", (2005). See here: http://www.cs.cmu.edu/~elaw/papers/pca.pdf

[77] P.J. de Groot, G.J. Postma, W.J. Melssen, L.M.C. Buydens, V. Deckert, R. Zenobi, "*Application of principal component analysis to detect outliers and spectral deviations in near-field surface-enhanced Raman spectra*", Analytica Chimica Acta **446**(1-2), 71-83 (2001).

[78] D. Uy, A.E. O'Neill, "*Principal component analysis of Raman spectra from phosphorus-poisoned automotive exhaust-gas catalysts*", Journal of Raman Spectroscopy **36**(10), 988-995 (2005).

[79] R.Y. Sato-Berrúa, C. Frausto-Reyesc, M. Villagrán-Muniza, S.H. Murrieta, J.M. Saniger, "*Application of principal component analysis and Raman spectroscopy in the analysis of polycrystalline $BaTiO_3$ at high pressure*", Spectrochimica Acta Part A: Molecular and Biomolecular Spectroscopy **66**(3), 557-560 (2007).

[80] S. Managò, C. Valente, P. Mirabelli, D. Circolo, F. Basile, D. Corda, A.C. De Luca, "*A reliable Raman-spectroscopy-based approach for diagnosis, classification and follow-up of B-cell acute lymphoblastic leukemia*", Scientific Reports **6**, 24821 (2016).

[81] C. Stergiou, D. Siganos, "*Neural networks*". See here: https://www.doc.ic.ac.uk/~nd/surprise_96/journal/vol4/cs11/report.html#Introduction

[82] Kevin Gurney, "*An introduction to neural networks*", UCL Press: London, UK (1997).

[83] M.A. Nielsen, "*Neural Networks and Deep Learning*", Determination Press (2015).

[84] J.T. Burger, "*A Basic Introduction To Neural Networks*". See here: http://pages.cs.wisc.edu/~bolo/shipyard/neural/local.html

[85] J.V. Tu, "*Advantages and disadvantages of using artificial neural networks versus logistic regression for predicting medical outcomes*", Journal of Clinical Epidemiology **49**(11), 1225-1231 (1996).

[86] M. Gniadecka, P.A. Philipsen, S. Sigurdsson, S. Wessel, O.F. Nielsen, D.H. Christensen, J. Hercogova, K. Rossen, H.K. Thomsen, R. Gniadecki, L.K. Hansen, H.C. Wulf, "*Melanoma diagnosis by Raman spectroscopy and neural networks: structure alterations in proteins and lipids in intact cancer tissue*", Journal of Investigative Dermathology **122**(2), 443-449 (2004).

[87] A.R. de Paula Jr, S. Sathaiah, "*Raman spectroscopy for diagnosis of atherosclerosis: a rapid analysis using neural networks*", Medical Engineering & Physics **27**(3), 237-244 (2005).

[88] M. Jermyn, J. Desroches, J. Mercier, M.A. Tremblay, K. St-Arnaud, M.C. Guiot, K. Petrecca, F. Leblond, "*Neural networks improve brain cancer detection with Raman spectroscopy in the presence of operating room light artifacts*", Journal of Biomedical Optics **21**(9), 94002 (2016).

[89] Z.Y. Li, S.P.S. Howarth, T. Tang, J.H. Gillard, "*How Critical Is Fibrous Cap Thickness to Carotid Plaque Stability? A Flow–Plaque Interaction Model*", Stroke **37**(5), 1195-1199 (2006).

[90] C.A. Schneider, W.S. Rasband, K.W. Eliceiri, "*NIH Image to ImageJ: 25 years of image analysis*", Nature Methods **9**, 671-675 (2012).

[91] P. Matteini, F. Ratto, F. Rossi, R. Cicchi, C. Stringari, D. Kapsokalyvas, F.S. Pavone, R. Pini, "*Photothermally-induced disordered patterns of corneal collagen revealed by SHG imaging*", Optics Express **17**(6), 4868-4878 (2009).

[92] Retrieved from the website of the US Centers for Disease Control and Prevention: https://www.cdc.gov/heartdisease/facts.htm

[93] Retrieved from the website of the US American Heart Association: http://www.heart.org/HEARTORG/Conditions/Cholesterol/WhyCholesterolMatters/Atherosclerosis_UCM_305564_Article.jsp#.WLlWkVUrLip

[94] D. Steinberg, A.M. Gotto, "*Preventing coronary artery disease by lowering cholesterol levels. Fifty years from bench to bedside*", Journal of the American Medical Association **282**(21), 2043-2050 (1999).

[95] W.C. Roberts, "*Twenty questions on atherosclerosis*", Proceedings (Baylor University. Medical Center) **13**(2), 139-143 (2000).

[96] C.K. Glass, J.L. Witztum, "*Atherosclerosis: The Road Ahead*", Cell **104**(4), 503-516 (2001).

[97] P. Libby, "*Inflammation in atherosclerosis*", Nature **420**(6917), 868-874 (2002).

[98] A.V. Finn, M.Nakano, J. Narula, F.D. Kolodgie, R. Virmani, "*Concept of Vulnerable/Unstable Plaque*", Arteriosclerosis, Thrombosis, and Vascular Biology **30**(7), 1282-1292 (2010).

[99] Retrieved from the website of the US Nation Heart, Lung, and Blood Institute: https://www.nhlbi.nih.gov/health/health-topics/topics/cad

[100] M.B. Lilledahl, A.O. Haugen, C.L. Davies, L.O. Svaasand, "*Characterization of vulnerable plaque by multiphoton microscopy*", Journal of Biomedical Optics **12**(4), 044005 (2007).

[101] R. Cicchi, C. Matthäus, T. Meyer, A. Lattermann, B. Dietzek, B.R. Brehm, J. Popp, F.S. Pavone, "*Characterization of collagen and cholesterol deposition in atherosclerotic arterial tissue using non-linear microscopy*", Journal of Biophotonics **7**(1-2), 135-143 (2014).

[102] Y. Sun, A.J. Chaudhari, M. Lam, H. Xie, D.R. Yankelevich, J. Phipps, J. Liu, M.C. Fishbein, J.M. Cannata, K.K. Shung, L. Marcu, "*Multimodal characterization of compositional, structural and functional features of human atherosclerotic plaques*", Biomedical Optics Express **2**(8), 2288-2298 (2011).

[103] H.W. Wang, I.M. Langohr, M. Sturek, J.X. Cheng, "*Imaging and quantitative analysis of atherosclerotic lesions by CARS-based multimodal nonlinear optical microscopy*", Arteriosclerosis Thrombosis and Vascular Biology **29**(9), 1342-1348 (2009).

[104] T.T. Le, I.M. Langohr, M.J. Locker, M. Sturek, J.X. Cheng, "*Label-free molecular imaging of atherosclerotic lesions using multimodal nonlinear optical microscopy*", Journal of Biomedical Optics **12**(5), 054007 (2007).

[105] A. Zoumi, X. Lu, G.S. Kassab, B.J. Tromberg, "*Imaging Coronary Artery Microstructure Using Second-Harmonic and Two-Photon Fluorescence Microscopy*", Biophysical Journal **87**(4), 2778-2786 (2004).

[106] J.E. Phipps, Y. Sun, R. Saroufeem, N. Hatami, L. Marcu, "*Fluorescence lifetime imaging microscopy for the characterization of atherosclerotic plaques*", Proceedings of SPIE – The International Society for Optical Engineering **7161** (2009).

[107] S.R. Watson, S.M. Lessner, "*(Second) Harmonic Disharmony: Nonlinear Microscopy Shines New Light on the Pathology of Atherosclerosis*", Microscopy and Microanalysis **22**(3), 589-598 (2016).

[108] J.L. Suhalim, C.Y. Chung, M.B. Lilledahl, R.S. Lim, M. Levi, B.J. Tromberg, E.O. Potma, "*Characterization of Cholesterol Crystals in Atherosclerotic Plaques Using Stimulated Raman Scattering and Second-Harmonic Generation Microscopy*", Biophysical Journal **102**(8), 1988-1995 (2012).

[109] R. Cicchi, E. Baria, C. Matthäus, M. Lange, A. Lattermann, B.R. Brehm, J. Popp, F.S. Pavone, "*Non-linear imaging and characterization of atherosclerotic arterial tissue using combined SHG and FLIM microscopy*", Journal of Biophotonics **8**(4), 347-356 (2015).

[110] C.D. Anderson, W.C. Lin, J. Beckham, A. Mahadevan-Jansen, C.R. Buttemere, J. Pierce, I.B. Nicoud, C. Wright Pinson, R.S. Chari, "*Fluorescence spectroscopy accurately detects irreversible cell damage during hepatic radiofrequency ablation*", Surgery **136**(3), 524-531 (2004).

[111] P. Chopra, U. Sabherwal, "*Histochemical and fluorescent techniques for detection of early myocardial ischemia following experimental coronary artery occlusion: A comparative and quantitative study*", Angiology **39**(2), 132-140 (1988).

[112] L. Salinas-Madrigal, C. Sotelo-Avila, "*Morphologic diagnosis of acute tubular necrosis (ATN) by autofluorescence*", American Journal of Kidney Diseases **7**(1), 84-87 (1986).

[113] G. Majno, I. Joris, "*Apoptosis, oncosis, and necrosis. An overview of cell death*", American Journal of Pathology **146**(1), 3-15 (1995).

[114] A. Kuehn, A. Graf, U. Wenzel, S. Princz, H. Mantz, M. Hessling, "*Development of a highly sensitive spectral camera for cartilage monitoring using fluorescence spectroscopy*", Journal of Sensors and Sensor Systems **4**(2), 289-294 (2015).

[115] J. E. Phipps, Y. Sun, M. C. Fishbein, L. Marcu, "*A Fluorescence Lifetime Imaging Classification Method to Investigate the Collagen to Lipid Ratio in Fibrous Caps of Atherosclerotic Plaque*", Lasers in Surgery and Medicine **44**(7), 564-571 (2012).

[116] "*Cancer Facts & Figures 2016*", American Cancer Society (2016).

[117] A. Jemal, R. Siegel, J. Xu, E. Ward, "*Cancer statistics, 2010*", CA: A Cancer Journal for Clinicians **60**(5), 277-300 (2010).

[118] See the website of the Skin Cancer Foundation: http://www.skincancer.org/skin-cancer-information/melanoma

[119] U. Banerji, A. Affolter, I. Judson, R. Marais, P. Workman, "*BRAF and NRAS mutations in melanoma: potential relationships to clinical response to HSP90 inhibitors*", Molecular Cancer Therapeutics **7**(4), 737-739 (2008).

[120] See the website My Cancer Genome: https://www.mycancergenome.org/content/disease/melanoma/

[121] M.F. Berger, L.A. Garraway, "*Applications of Genomics in Melanoma Oncogene Discovery*", Hematology/Oncology Clinics of North America **23**(3), 397-414 (2009).

[122] T. Huang, J. Zhuge, W.W. Zhang, "*Sensitive detection of BRAF V600E mutation by Amplification Refractory Mutation System (ARMS)-PCR*", Biomarker Research **1**, 3 (2013).

[123] K. Hamada, K. Fujita, N. Smith, M. Kobayashi, Y. Inouye, S. Kawata, "*Raman microscopy for dynamic molecular imaging of living cells*", Journal of Biomedical Optics **13**(4), 044027 (2008).

[124] E. Brauchle, S. Noor, E. Holtorf, C. Garbe, K. Schenke-Layland, C. Busch, "*Raman spectroscopy as an analytical tool for melanoma research*", Clinical and Experimental Dermatology **39**(5), 636-645 (2014).

[125] H. Wang, T.H. Tsai, J. Zhao, A.M. Lee, B.K. Lo, M. Yu, H. Lui, D.I. McLean, H. Zeng, "*Differentiation of HaCaT cell and melanocyte from their malignant counterparts using micro-Raman spectroscopy guided by confocal imaging*", Photodermatology, Photoimmunology & Photomedicine **28**(3), 147-152 (2012).

[126] C. Krafft, C. Beleites, I.W. Schie, J.H. Clement, J. Popp, "*Raman-based identification of circulating tumor cells for cancer diagnosis*", Proceedings of SPIE **9704** (2016).

[127] See the website of Horiba: http://www.horiba.com/scientific/products/raman-spectroscopy/raman-academy/raman-faqs/how-long-does-it-take-to-acquire-a-raman-spectral-image/

[128] Retrieved from the American Cancer Society website: http://www.cancer.org/cancer/bladdercancer/detailedguide/bladder-cancer-what-is-bladder-cancer

[129] R. Montironi, A. Lopez-Beltran, R. Mazzucchelli, D. G. Bostwick, "*Classification and grading of the non-invasive urothelial neoplasms: recent advances and controversies*", Journal of Clinical Pathology **56**(2), 91-95 (2003).

[130] C. S. Lee, C. Y. Yoon, J. A. Witjes, "*The past, present and future of cystoscopy: the fusion of cystoscopy and novel imaging technology*", BJU International **102**(9 Pt B), 1228-33 (2008).

[131] E. Baria, A. Barone, G. Nesi, F.S. Pavone; R. Cicchi, "*Imaging of human urothelial carcinoma samples using multimodal multiphoton microscopy*", SPIE Proceedings **104140Q** (2017).

[132] Q. Li, Q. Gao, G. Zhang, "*Classification for breast cancer diagnosis with Raman spectroscopy*", Biomedical Optics Express **5**(7), 2435-2445 (2014).

[133] R. Cicchi, A. Crisci, A. Cosci, G. Nesi, D. Kapsokalyvas, S. Giancane, M. Carini, F. S. Pavone, "*Time- and spectral-resolved two-photon imaging of healthy bladder mucosa and carcinoma in situ*", Optics Express **18**(4), 3840-3849 (2010).

[134] G. Deinum, D. Rodriguez, T.J. Romer, M. Fitzmaurice, J.R. Kramer, M.S. Feld, "*Histological Classification of Raman Spectra of Human Coronary Artery Atherosclerosis Using Principal Component Analysis*", Applied Spectroscopy **53**(8), 938-942 (1999).

[135] S.W. van de Poll, T.J. Römer, G.J. Puppels, A. van der Laarse, "*Imaging of atherosclerosis. Raman spectroscopy of atherosclerosis*", Journal of Cardiovascular Risk **9**(5), 255-261 (2002).

[136] A.R.de Paula Jr, S. Sathaiah, "*Raman spectroscopy for diagnosis of atherosclerosis: a rapid analysis using neural networks*", Medical Engineering & Physics **27**(3), 237-244 (2005).

[137] A.I. Baba, C. Câtoi, "*Comparative Oncology – Chapter 3: Tumor cell morphology*", The Publishing House of the Romanian Academy: Bucharest, Romania (2007).

[138] S. Bandeira CartaxoI, I. Dunshee de Abranches Oliveira Santos, R. Bitar, A. Fernandes Oliveira, L. Masako Ferreira, H. Silva Martinho, A.A. Martin, "*FT-Raman spectroscopy for the differentiation between cutaneous melanoma and pigmented nevus*", Acta Cirurgica Brasileira **25**(4), 351-356 (2010).

[139] S. Feng, S. Huang, D. Lin, G. Chen, Y. Xu, Y. Li, Z. Huang, J. Pan, R. Chen, H. Zeng, "*Surface-enhanced Raman spectroscopy of saliva proteins for the noninvasive differentiation of benign and malignant breast tumors*", International Journal of Nanomedicine **10**(1), 537-547 (2015).

[140] D. Sahu, Y. Lotan, B. Wittmann, B. Neri, D.E. Hansel, "*Metabolomics analysis reveals distinct profiles of nonmuscle-invasive and muscle-invasive bladder cancer*", Cancer Medicine **6**(9), 2106-2120 (2017).

[141] H.H. Kim, "*Endoscopic Raman Spectroscopy for Molecular Fingerprinting of Gastric Cancer: Principle to Implementation*", BioMed Research International **670121** (2015).

[142] E. Vargis, E.M. Kanter, S.K. Majumder, M.D. Keller, R.B. Beaven, G.G. Rao, A. Mahadevan-Jansen, "*Effect of normal variations on disease classification of Raman spectra from cervical tissue*", The Analyst **136**(14), 2981-2987 (2011).